Impact of Mechanical Loading on the Deformation and the Electronic Properties of Metallic Nanoparticles

Matteo Erbi

Sorbonne Université

ED397 - Physics and chemistry of materials

Laboratoire d'Etude des Microstructures - ONERA/CNRS

Impact of Mechanical Loading on the Deformation and the Electronic Properties of Metallic Nanoparticles

Par Matteo Erbi'

Thèse de doctorat de Physique des materiaux

Présentée et soutenue publiquement le 24 Novembre 2023

Devant un jury composé de :

Ferrando Riccardo	Professor - Univ. Genoa	Rapporteur
Godet Julien	Maitre de conference - Univ. Poitiers	Rapporteur
Montalenti Francesco	Professor - UniMiB	Examinateur
Mottet Christine	Directrice de Recherche - CINaM	Présidente du jury
Pietrucci Fabio	Maitre de conference - Univ. Sorbonne	Examinateur
Putz Barbara	Assistant professor - Empa	Examinatrice
Amara Hakim	Directeur de Recherche - ONERA	Directeur de These
Gatti Riccardo	Chargé de recherche - CNRS	Encadrant de These

March 8, 2024 ONERA

Contents

List of Figures

List of Tables

List of Abbreviations

ldos	Local density of State
BCC	Body Centered Cubic
DFT	Density Functional Theory
DOS	Density of State
EAM	Embedded Atom Method
FCC	Face-Centered Cubic
FE	Finite Element
FEM	Finite Element Method
HCP	Hexagonal Close-Packed
MD	Molecular Dynamics
NP	Nano-Particles
PDE	Partial Differential Equation
SFE	Stacking Fault Energy
SMA	Second Moment Approximation
TB	Tight-Binding
TC	Truncated Cube
TO	Truncated Octahedron
USFE	Unstable Stacking Fault Energy

Nomenclature

α	Exponent for size effect
μ_1, μ_2	First and second momentum
$\sigma_{c,y}$	Critical and yield stress
σ_{rss}	Resolved Shear Stress
σ_v	Von Mises Stress
E_{eff}	Effective Young's modulus
$\boldsymbol{\sigma}, \sigma_{ij}$	Stress tensor
$\boldsymbol{\varepsilon}, \varepsilon_{kl}$	Strain tensor
$\boldsymbol{b}$	Burger vector
$\boldsymbol{C}, C_{ijkl}$	Elastic tensor
$\boldsymbol{u}$	Displacement vector
Ψ	Wave function
a	Lattice parameter
d	Object size
d_n	Local density of states of site n
E_b	Binding Energy
E_f	Fermi Energy
G	Shape parameter
H	Hamiltonian
R	Ion space
r	Electron space

Introduction 1

This study focuses on metallic nano-structure, particularly nanoparticles with sizes in the nanometer range corresponding to a total number of atoms usually between $\sim 10^2$ to $\sim 10^6$. These nano-objects have attracted significant attention due to their unique physical and chemical properties exploited thanks tospecificities an increased surface-to-volume ratio and even the possibility of having a defect-free system. Thanks to this and many other interesting features, nanoparticles have found applications in various fields such as catalysis, electronics, biomedicine, and mechanics. [1–4].

The Ph.D. was conducted at the "Laboratoire d'Etude des Microstructures" (LEM), a laboratory whose research is organised around two main branches. One branch investigates the evolution of microstructures and their influence on physical properties of materials, in particular predicting the mechanical properties of metallic alloys, including the study of plasticity, via models at the mesoscopic scale such as the discrete dislocation dynamics and the phase field method. The second branch deals with low-dimensional material focusing on synthesis, characterization, and electronic optical properties by combining experiments and simulations at the atomic scale. The present thesis aimed to leverage on the knowledge and the expertise acquired at the LEM to study mechanical end electronic properties of nano-structures, creating a new area of research within the laboratory. Consequently, the current study aims to firstly investigate the interplay among shape, size, and composition of nanoparticles (NPs), with the ultimate goal of engineering a new class of nano-objects with targeted mechanical properties, and secondly to understand the relation between mechanical deformation and electronic properties, with the particular application of catalysis.

This manuscript is divided into seven chapters. The first chapter provides theoretical concepts and establishes a general context based on previous bibliographical works, where this work is developed(Chapter 1). Chapter 2 describes the methodologies and techniques used in the project. In the following four chapters the results are presented. Chapter 3 focuses on how the elastic response of a nanoparticle is influenced by their size and shape. In contrast, Chapter 4 examines the plastic behavior of these structures, focusing on the onset of plasticity. Chapter 5 explores the impact of composition by comparing the response of pure materials to alloy systems. Chapter 6, throughout the knowledge acquired in the field of mechanics, investigates the effects of elastic and plastic deformation on local electronic properties. In the

final chapter, the conclusions drawn from the previous chapters are presented along with future perspectives for possible related work.

1.1 Total energy of a crystal

The opening chapters of this manuscript revolve around the Hamiltonian of a crystal. Although the problem is technically unsolvable, by introducing certain approximations, we can simplify it and examine the mechanical and electronic properties. This method is applicable to bulk materials and nano-structures, covering single-element materials, alloys, and systems with defects.

Within a solid, the nucleus of an atom oscillates around an equilibrium position, while the core electrons and higher-energy electrons exhibit different degrees of freedom depending on the system. In metals, these higher-energy electrons can be highly delocalized (almost free), while in non-metallic systems, they tend to be more localized. From the perspective of quantum mechanics in materials science, the study of total energy can be attributed to a fundamental problem known as the many-particle Hamiltonian.

In this context, it is intuitive to consider that the contributions to the total energy arise from the interactions of all electrons and ions in the crystal. These contributions include both the kinetic energy and the Coulomb interactions leading to the following Hamiltonian (H):

$$H = \sum_i \frac{P_i^2}{2M} + \sum_j \frac{p_j^2}{2m} - \sum_{ij} \frac{Ze^2}{(r_i - R_j)} + \frac{1}{2}\sum_{ij} \frac{e^2}{(r_i - r_j)} + \\ + \frac{1}{2}\sum_{ij} \frac{Z^2e^2}{(R_i - R_j)} \tag{1.1}$$

The first two terms of equation 1.1 represent the kinetic contribution given by ions and electrons (T_e), respectively, where M and P_i stand for the mass and momentum of the ion and m and p_j for the electrons. The indexes i, j correspond to the contribution over all the ions and electrons, respectively. The last terms correspond to the Coulomb interactions: the third one represents the electron-ion interaction, V_{Ie}, fundamental to determine most of the electronic properties, together with the electronic kinetic contribution, and with some correction that can be brought by the electron-electron interaction (fourth term V_{ee}). The last interaction is the ion-ion one, V_{II} describing the repulsive and attractive behavior of the nucleus in a solid. In all the contributions, Z and e represent the atomic number and the electron charge, respectively [5–7].

The energy of the system can be calculated by solving the time independent Shrödinger equation:

$$H\Psi(r_i, R_j) = E\Psi(r_i, R_j), \tag{1.2}$$

with E the total energy, and Ψ the system wave-function that depends on the nucleus and electronic position. The problem is unsolvable, given the too-high number of degrees of freedom (represented by all the ions and electrons). Some hypotheses are therefore required to simplify it depending on the application of interest. During the last century, two main ideas and classes were adopted to solve the problem; an overview is presented in Figure 1.1.

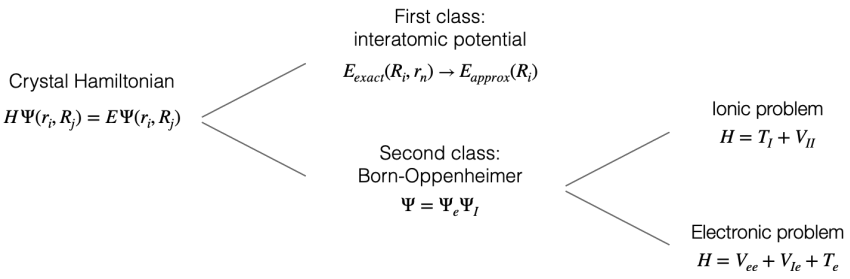

Figure 1.1: Schematic view of different types of solutions for the crystal Hamiltonian. On one side, there is the solution that leads to the design of interatomic potentials for MD applications. On the other side, the solution that leads to the electronic Hamiltonian, which allows the study of the electronic properties of materials.

In the first class, the degrees of freedom given by the electrons are removed, and their effect is embedded in V_{II} to create an effective interaction as:

$$E_{exact}(R_i, r_n) \rightarrow E_{approx}(R_i) \tag{1.3}$$

It is a strong approximation where all the information on electron energies is lost. However, it can allow us to study the ion's motion in a potential that still considers the electronic effect. This assumption is considered to develop inter-atomic potentials that can be used in MD to emulate real mechanical tests or to understand the macroscopic mechanical properties, such as ductility or elasticity. In the second class of solution, the effect of electrons on the energies is explicitly considered, but different strategies are used to simplify the problem.

The second class exploits the Born-Oppenheimer approximation, that is a powerful tool that allows us to separate the electronic and ionic contributions, simplifying them into two different and more manageable problems. This approximation is based on the significant difference in mass between electrons and ions, allowing the electrons to adjust to the motion of the ions quickly. This separation leads to the electronic and ionic Hamiltonian formulation, as depicted in Figure 1.1.

Obviously, the electronic Hamiltonian serves as a basis for various models developed to analyze electronic properties. The level of approximation in these models determines the accuracy and details they provide, ranging from the simple Fermi theory to the more

sophisticated DFT. As the complexity increases, so does the computational cost. A good compromise between accuracy and computational efficiency is achieved with the Tight-Binding (TB) formalism, which is the method chosen in this work to address electronic properties and is described in Section 2.5.

1.2 MECHANICAL PROPERTIES OF BULK MATERIALS

In the first class of approximation of the crystal Hamiltonian, the behaviour of electrons is combined with that of ions, through a potential. By studying an effective potential, it is possible to link macroscopic properties with the atomic behaviour of the chosen material. To understand this, we must introduce a useful quantity called the binding or cohesive energy E_b. It is defined as the energy required to create or break a bond, and from it, we can recover information on the type of bond or the elastic response of the material. In Figure 1.2, we can observe two different materials and the difference

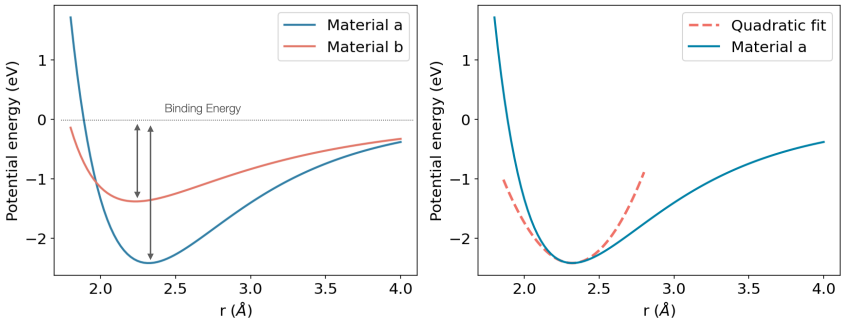

(a) (b)

Figure 1.2: Figure (a): difference in binding energy in two different materials. Figure (b): quadratic local approximation of the inter-atomic potential, that leads to one branch of continuum mechanics.

in the binding energy. Larger binding energy indicates very strong bonds that can be ionic or covalent (as for ceramic material). On the other hand, metals have lower binding energy with consequent different properties, such as good ductile behavior.

The strength of a material is highly micro-structure dependent and can be engineered, almost losing all the connection with the type of bond. However, if we consider the elastic response, change in the micro-structure does not affect the link with the binding energy too much. This relation can be understood by observing the proportional relation between the cohesive energy E_b and the bulk modulus (B) in table 1.1, where the latter is defined as the material resistance to isotropic deformation.

	B (GPa)	E_b (eV/at)
Cu	137	-3.49
Au	173	-3.81
Ni	186	-4.44
Pt	278	-5.84

Table 1.1: B, E_b extracted from [6]. Materials with higher binding energies might exhibit higher bulk modulus values because they resist to deformation more strongly.

The connection between atomic physics and macroscopic behavior can be made thanks to the harmonic approximation, where atoms can be seen as a point of a network connected by springs, characterised by a quadratic potential, see Figure 1.2b. This assumption allows to study the heat or the phonon dispersion in a specific material,

and to establishes the connection between an effective potential and the elastic constants [7]. From this approximation, we can directly establish the relation between the total energy of the system (E_{tot}) that can be thought as the sum of all the potential in a crystal, the strain tensor ϵ_{ij} , the volumetric factor (Ω) and the fourth-order elasticity tensor (C_{ijkl}) as:

Throughout this study, tensors are referenced using Einstein notation; see the appendix for details 8.1

$$C_{ijkl} = \frac{1}{\Omega}\frac{\partial^2 E_{tot}}{\partial\epsilon_{ij}\partial\epsilon_{kl}}, \tag{1.4}$$

with i, j, k, l representing the x, y, and z directions [5].

1.2.1 Continuous theory - the linearized theory of elasticity

The central problem of continuous mechanics is deformation, i.e. how a specific structure reacts to an external loading. It is a fundamental issue from the engineering point of view because it allows for the proper design of structures and materials able to withstand various deformation conditions.

The continuous theory allows to reduce the complexity of the material without considering all the degrees of freedom given by all the atoms. In this case, the objects are considered homogeneous. This theory is based on three fundamental quantities: stress, strain, and displacement.

The stress tensor characterizes the internal forces acting per unit area on a surface element, oriented in a specified direction. It is commonly denoted by $\boldsymbol{\sigma} = \sigma_{ij}$, for a force that acts in the i direction on a surface with a normal oriented in the j one.

Regarding the strain, a material or structure can be deformed in different ways, and two are the theories that deal with it: the infinitesimal strain theory and the Finite strain theory. In the first, we make the approximation that the displacement ($\nabla\boldsymbol{u}$) is very small, leading to significant simplifications of the deformation problem [8]. The second theory deals with large deformation, invalidating the assumption of the infinitesimal strain theory . Our deformation condition, smaller than 10%, places us in the first case, from which the strain ($\boldsymbol{\varepsilon}$) is defined:

$$\varepsilon_{ij} = \frac{1}{2}\left(\frac{\partial u_i}{\partial x_j} + \frac{\partial u_j}{\partial x_i}\right) \tag{1.5}$$

where i and j representing the x, y, and z directions. The strain tensor is symmetric and of the second order, $\varepsilon_{ij} = \varepsilon_{ji}$. Stress and strain are linked through Hooke's law. Therefore, in case of small deformation, the strain is directly proportional to the stress through the following equation:

$$\sigma_{ij} = C_{ijkl}\varepsilon_{kl} \tag{1.6}$$

At this point, it is important to mention that C_{ijkl} are written in the Voigt notation in the manuscript, which is a way of simplifying the fourth order tensor to a second order. Following the symmetries of the $\boldsymbol{\sigma}$ and $\boldsymbol{\epsilon}$ tensor and dealing with a cubic crystal, it can be shown that only three independent elastic constants exist: C_{11}, C_{12} and C_{44}.

Now that the fundamental quantities are introduced, we can move on to the Partial Differential Equation (PDE), which describes how a given object reacts to a load. When no acceleration is considered, from Newton's second law it can be derived:

$$\frac{\partial}{\partial x_i}\left(\sigma_{ij}\right) = f_i \rightarrow \nabla\boldsymbol{\sigma} = \mathbf{f} \tag{1.7}$$

with $\mathbf{f}$ representing the body force (as for gravity), zero in this case. Here, σ_{ij} is obtained by:

$$\sigma_{ij} = \frac{\partial U}{\partial \varepsilon_{ij}} \tag{1.8}$$

with U the elastic energy density given by:

$$U = \frac{1}{2} C_{ijkl}\varepsilon_{ij}\varepsilon_{kl} \tag{1.9}$$

More precisely, U measures the potential energy stored in the material when it is elastically deformed. If the load is released, the elastic energy dissipates, and the sample returns to its original shape.

1.2.2 Stress-strain curves analysis

In the field of materials science, mechanical properties can be probed and measured through tensile or compressive tests. In these experiments, a sample undergoes to pulling or pushing forces and the corresponding displacement is measured. These quantities are closely related to stress, $\sigma = F/A$ with F the force applied by, for instance, an indenter and A the sample area and to strain $\varepsilon = \Delta L/L_0$ with ΔL the change in specimen's dimension compared to the initial one L_0. The stress-strain curve describes the relationship between stress and strain (see Figure 1.3), from which two main regimes can be identified: the elastic and the plastic one. In the elastic domain, the study of the stiffness or of the Young's modulus (E) is fundamental. This corresponds to the elastic response to an applied stress, the slope of the linear part of the stress-strain curve, as depicted in Figure 1.3. Any deformation in this regime is reversible; removing the loading, the original configuration of atoms can always be recovered. The limit between elasticity and plasticity is defined by the yield stress or critical stress, denoted as σ_y in this work, and it is related to the strength of the material (limit of the elastic regime in Figure 1.3). After the σ_y, in the plastic regime, deformation in the system is irreversible. The elementary mechanism regulating the elastic- plastic transition

In the case of macroscopic material it is preferred to talk about yield point. In nano and pristine object, the preferred choice is the critical stress σ_c, the point where a dislocation nucleate.

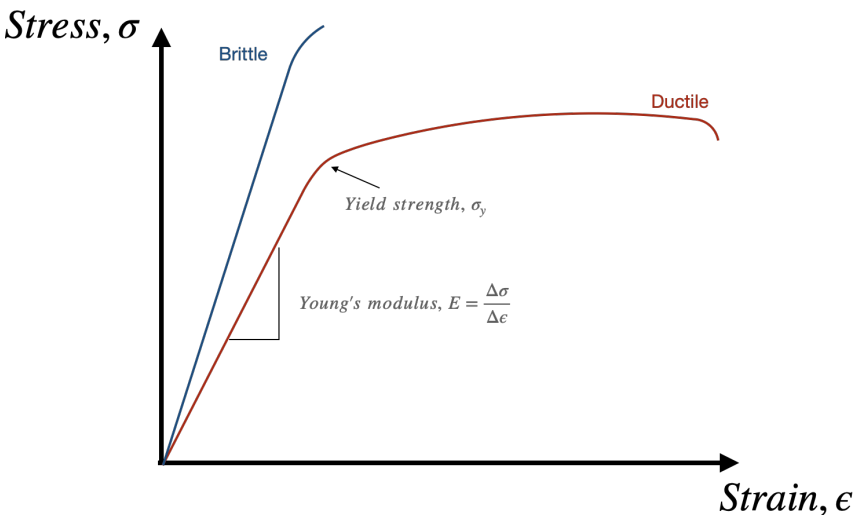

Figure 1.3: Typical stress and strain curve for macroscopic material, brittle and ductile.

change changing the size. In bulk systems, preexisting dislocations start to move whereas, at the nanoscale, often, a dislocation nucleates. In the plastic domain, we can define ductility as the ability of a material to be permanently deformed without breaking. In this regime, we usually observe hardening; the structure results harder to deform as the loading increases.. This is the result of dislocation microstructure formation due to the dislocation motion, interaction and multiplication. In Figure 1.3, the difference between a ductile and a brittle material is presented where, respectively, after reaching σ_y, one keeps deforming and the other one fails. This property can be linked to the type of material and bonds such as ductile metallic and brittle ionic bond.

In the context of our work, numerous theories and research efforts have been devoted to understanding and controlling the three key parameters: stiffness, strength, and ductility, around which our work is designed.

1.2.3 CONTINUUM THEORY OF PLASTICITY: INTRODUCTION TO DISLOCATIONS

Various theories study the onset of plasticity and the plastic regime in crystalline materials , trying to predict the behavior of a sample under external loading. We can mention Molecular Dynamics (small sizes), Phase Field theory (crack and dislocation study by mean of elastic field) or Discrete Dislocation Dynamics (based on the concept that dislocation motion and interaction govern plasticity).

The first explanation of plasticity has been provided by Frenkel in 1923. He wanted to find a way to predict the shear yield point (σ_{ideal}) of materials from a microscopic point of view. He calculated the slip energy of two planes shearing one respect to the other. What he found out is $\sigma_{ideal} \sim C_{44}/2\pi$ for a metal; this is what usually is

referred as ideal shear strength [9] . Evident differences arise between this theory, where the system is considered perfectly crystalline, and reality. Aluminum, for example, is elastically deformed only for strain lower than 10^{-5}. Other materials such as germanium and silicon, at room temperature, do not deform plastically and crack just after the elastic regime [6].

	C_{44}	σ_{ideal}	σ_{bulk}
Au	45.4	7.22	0.20
Cu	81.8	13.0	0.79
Pt	100	13.0	0.17
Ni	131	20.8	0.46

Table 1.2: All the units in (GPa). C_{44} from [6]. Note for σ_{bulk} the exact strength point can vary depending on a variety of factors including its purity, its manufacturing history (work hardening or annealing processes), and its grain structure. Values extracted from [10–12],

The ideal shear strength is usually of the order of magnitude ~ (GPa), way larger compared to what can be found in bulk material ~ MPa. In table 1.2 some typical values for transition metal are listed. In the following years, many different people proposed a theory on plasticity based on dislocation motion. The basic idea is that to break a simple line of atom's bonds is easier than to shear a complete plane, much lower energy is needed: plasticity is the result of defects motion.

Defects in a solid

In real crystals, imperfections are present in the form of point, line, surface, or volume defects, which locally disrupt the regular arrangement of atoms.

Thus, the point defects are vacant atomic sites or self-interstitial atoms that can be generated through, for instance, irradiation. Besides, the stacking faults are planar defects interrupting the regular stacking sequence within a crystal. They can originate after a dislocation slip or as intrinsic defects at the synthesis. Additionally, crystalline solids typically consist of numerous randomly oriented grains separated by grain boundaries constituting volume defects.

Lastly, line defects are called dislocations. Dislocations represents the contour line of a sheared region, along a lattice direction, of the crystals. They can be of two elemantary types: edge and screw dislocations. As highlighted in Figure 1.4, assuming that the green lines are the dislocation line directions, an edge dislocation configuration can be visualized by adding a plane to half of the crystalline structure (left figure). Conversely, a screw dislocation (right figure) can be pictured by shearing the crystal along the dislocation line direction. A way to identify a dislocation is to introduce the notion of Burgers vector, $\boldsymbol{b}$. The Burgers vector is the lattice direction in which a dislocation shear a crystal. To visualize it, we can draw a circuit on a perfect lattice (called the Burgers circuit, top of the panel in Figure 1.4). A difference can be noticed by introducing an extra half plane and drawing the circuit again among the same points; this difference is called the Burgersvector. In the edge dislocation case, $\boldsymbol{b}$ is perpendicular to the dislocation line; meanwhile, in the screw case is parallel. Pure edge or screw dislocation exists in a real crystal, nonetheless we mainly observe mixed patterns: the summation of elementary edge and screw dislocation.

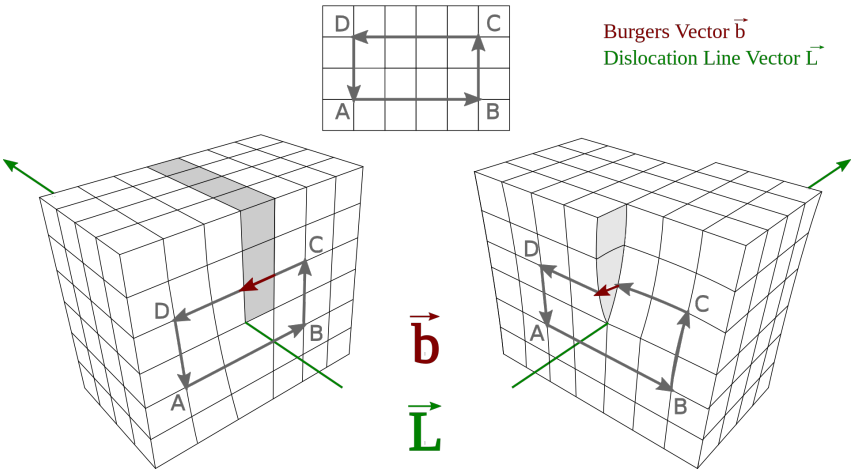

Figure 1.4: Edge dislocation (left), screw dislocation (right) and Burger circuit (top) as well as schematic representation of the Burgers vector. Figure extracted from [13].

DISLOCATION MOTION

When loading a sample, and it starts to deform plastically, preexisting dislocations begin to move and interact. In this study, we only consider dislocation motion (glide) inside the plane defined by the Burgers vector and the dislocation line (glide plane), but other mechanisms exist as the non-conservative motion (climb), where the dislocation moves out from the gliding plane. Plastic deformation happens by dislocation gliding on a given plane, an example is presented in Figure 1.5, where the motion of an edge dislocation in the Burgers vector direction is displayed. Dislocation motion is caused by internal or

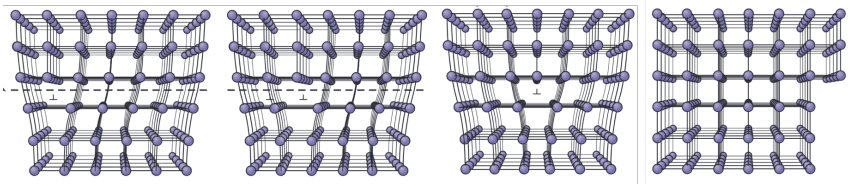

Figure 1.5: Dislocation movement inside a crystal. When the dislocation gets out from the crystal a surface step is created. Figure extracted from [14].

external stress field acting on the line defects. The stress acting on a dislocation is called the resolved shear stress (σ_{rss}) defined as:

$$\sigma_{rss} = \boldsymbol{s} \cdot \boldsymbol{\sigma n} \tag{1.10}$$

with $\boldsymbol{\sigma}$ the stress tensor, $\boldsymbol{n}$ the normal to the slip plane, and $\boldsymbol{s}$ the slip direction. In our case, it is the Burgers vector. This is an important quantity because it gives the effective stress in the slip direction, responsible for dislocation motion.

Another useful quantity is the von Mises stress (σ_v) which plays a crucial role in macro-material to predict the yield of ductile systems under complex loading scenarios. For a general three-dimensional system, σ_v is given by:

$$\sigma_{\mathrm{v}}^2 = \frac{1}{2}\left[(\sigma_{11}-\sigma_{22})^2 + (\sigma_{22}-\sigma_{33})^2 + (\sigma_{33}-\sigma_{11})^2 + \right. \\ \left. +6\left(\sigma_{23}^2 + \sigma_{31}^2 + \sigma_{12}^2\right)\right. \tag{1.11}$$

with σ_{11}, σ_{22}, and σ_{33} represent the normal stresses in the x, y, and z directions respectively. σ_{12}, σ_{23}, and σ_{31} denote the off diagonal terms.

By evaluating the von Mises stress, one can assess the potential for material failure by comparing it to the material's yield strength. Typically, the von Mises criterion is applied to situations and materials where dislocations already exist. The notion of resolved shear stress and von Mises stress are useful to study the onset of plasticity in nanoparticles. As already mentioned, in such pristine object the onset of plasticity occurs via dislocation nucleation. In our study, we are not aiming to construct a comprehensive theory for the prediction of nucleation or slip events. Instead, our focus is on the phenomenological processes behind these events. Consequently, quantity such as σ_v and σ_{rss} that accounts for all stress components demonstrate to be key parameters.

Elastic energy in dislocation

When compressing, energy is transmitted, for instance, from the indenter to the sample. In case of elastic deformation, no permanent changes happen in the crystal. When releasing the load, the system tends again to its original ground state. In the plastic regime, this energy is used to move defects and thus to permanently displace atoms, making the crystal different from its original configuration. Around the dislocation, atoms undergo a stress field generated by the presence of the dislocation. In Figure 1.5, the nature of this stored energy is evident: atoms above the dislocation line are compressed, and atoms below are stretched, far from their equilibrium position. Potential energy is stored in this object. An important relation between elastic energy E_{el} and Burgers vector is $E_{el} \propto C_{44}b^2$ with C_{44} the shear modulus. When loading our sample, the total elastic energy is given by the interaction between the dislocation micro-structure induced and the loading induced stress field [9].

Partial dislocation

The object of this study are transition metals such as copper, gold, platinum, and nickel. These metals have an FCC structure. As we have previously seen, dislocation energy is proportional to the square of the Burgersvector $\propto \boldsymbol{b}^2$. Slip is more likely to be in the direction with the highest concentration of atoms where the distance between atoms is lower, {111} planes in FCC lattice. Moreover, the shortest lattice vectors are $a/2\langle 110\rangle$ and $a\langle 001\rangle$ where a is the lattice parameter. The elastic energy of a dislocation in the [110] is half the [001] direction; thus, it is the privileged slip direction. Summarising, in an FCC structure, four equivalent {111} planes can be found, each having

three ⟨110⟩ slip directions and therefore twelve slip systems. When

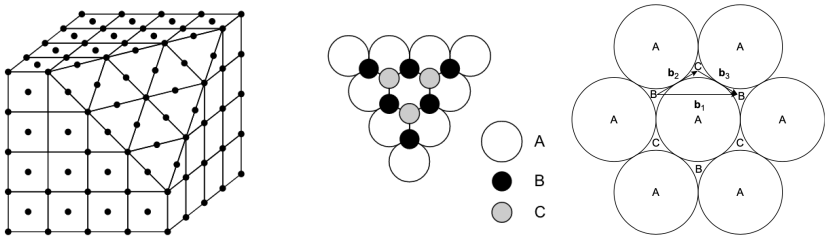

(a) (b)

Figure 1.6: Figure (a): (111) slice of a cubic FCC structure, and the different layers in the [111] direction, A,B and C. Figure (b): Partial dislocation moving atom B in C position, creating a stacking fault. The effect of the second partial dislocation bringing back atom B in a B position. Figures extracted from [9].

a dislocation moves of a translation lattice vector (as for $a/2\langle 110\rangle$), it leaves the crystal behind intact and perfect. This is what is called a perfect dislocation. What happens, in reality, is more complex. In Figure 1.6, a slice normal to the [111] direction can be found together with, at the right, the three-fold stacking sequence of an FCC structure. It is straightforward to observe that for an atom it is easier to move from a B position to C ("into the potential valley") compared to a direct BB transition. This process creates a stacking fault inside the crystal (transition BC) and the total energy increase of a quantity called stacking fault energy (quantity per unit area). This position is not stable since a B atom is stable in the B position. Thus, the first partial dislocation is followed by a second partial dislocation, bringing the B atom from the C position back to the B one. The perfect dislocation $b_1 = \frac{1}{2}\langle 110\rangle$ might dissociate in two partial dislocations called Shockley partial dislocations as:

$$b_1 = \frac{1}{2}\langle 110\rangle \rightarrow \frac{1}{6}\langle 221\rangle + \frac{1}{6}\langle 12\bar{1}\rangle \tag{1.12}$$

This occurs if the energy of the two Shockley partial dislocations plus the energy of the created stacking fault is smaller than the energy of the perfect dislocations.

1.2.4 Engineering mechanical properties of bulk materials

This section aims to give a global overview of the main techniques used nowadays for controlling and improving a material's mechanical response: the Hall-Petch effect, solid solution strengthening and strain hardening.

The Hall-Petch effect is a physical phenomenon, observed in polycristals, where the strength of the material increases as the grain size decreases $\sigma_y = \sigma_0 + \frac{k_y}{\sqrt{d}}$, with σ_y the yield stress, σ_0 constant stress needed to start dislocation motion, k_y a strengthening coefficient and d the grain size. Consequently, reducing the grain size increase the number of grain boundaries. This type of defect slow down or block dislocation motion increasing the total strength of the material. With

the solid solution technique, materials are strengthened by exploiting the same physical process. In this case, the dislocation are blocked or slowed down by a substitutional defects. The added atoms create lattice distortions and thus a local stress field that alters the dislocation motion process.

When a solid solution is supersaturated (at high temperature), we have the formation of small precipitates that help strengthen the sample. This technique is called precipitation hardening. The strain hardening process is a much simpler technique. Loading a metallic sample at first, we deform it elastically and, secondly, plastically where dislocations move and multiplicate themselves. This new crystal configuration is stronger since dislocation motion is blocked by the formation of a dislocation microstructure.

1.3 Mechanical properties at the nanoscale

From classical metallurgy to the era of nanotechnology, new techniques for the production of materials with growing smaller scales led to the discovery of many new interesting properties that nowadays are used to improve the mechanical performance [4], such as composite materials [15, 16], NEMS [17] and lubrifiant [18]. It is also important to evaluate the mechanical stability of fundamental processes like catalysis [2] or even in biological environments where nanoparticles are highly applied in cancer treatment [1].

The first materials with lower dimensions used are thin films. Developed in the 20th century, only after the invention of the vacuum deposition technique, it discovers that the thinner the film (here lower than $1\mu m$) and the stronger it is, from which the motto *smaller is stronger* is born. To move one dimension down into the study of micro-pillars, we had to wait until the 2000's. These micro-pillars are object typically of few micrometers and possess varying aspect ratios. In 2004, *Uchic et al.* [19, 20] are the first to discover that the "smaller is stronger" principle also applies to micro-pillars. Indeed, pillars with nanometric dimensions exhibit incredible strength compared to bulk materials. As seen in Figure 1.7, the critical stress is highly improved when the size is reduced. Moreover, it is also interesting to observe the trace of the plastic events, with surface steps all around the pillar surface. In this particular case, the critical stress (σ_c) is characterized by the following power law:

$$\sigma_c = Ad^{-\alpha} \tag{1.13}$$

where d represents the diameter of the micro-pillar and α is a fitted exponential.

With advancements in techniques, we can now produce reduced-sized pristine samples. However, the classical arguments on plasticity discussed earlier cannot be directly applied to these samples. Micro-pillars and nanoparticles possess significantly higher strength than bulk materials, often approaching the theoretical limits discussed in Section 1.2.3. Geer and colleagues in 2005 initially explained this phenomenon through a process known as dislocation starvation [21]. The idea is based on the observation that micro-pillars typically exhibit a residual dislocation density. During compression, dislocations either escape through free surfaces or annihilate each other, depending on their size, ultimately leaving the sample defect-free at a certain point. The plastic transition in pristine systems is governed by the process of dislocation nucleation. The experimental technique

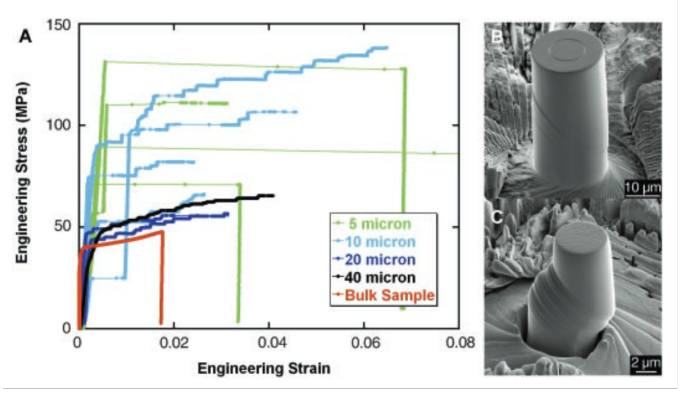

Figure 1.7: Experimental nano-indentation of micro-pillars. Stress and strain curves highlighting size effects. Results extracted from [19].

commonly employed for this purpose is called nano-indentation (or nanocompression). Operating solely in compression, the objective is to replicate the same curve observed for bulk materials in Section 1.2.2. Nano-indentation experiments can be performed based on various methods where the pico indenter being the most commonly used instrument allowing for simultaneous imaging (SEM, FIB/SEM, PFIB) and nanomechanical testing. These experiments enable the extraction of stress-strain curves. It is worth noting that strong theoretical modeling is often employed in conjunction with these experiments. Theoretical models serve to justify and comprehend the results, as well as to design experiments from scratch. From a modeling perspective, Molecular Dynamics, FE analysis and Dislocation Dynamics [22] are commonly applied to study mechanical problems. In extreme cases, Density Functional Theory [23] is also used. Each technique has its advantages and disadvantages. Thanks to these approaches, many important physical properties of mechanics at the nanoscale have been highlighted allowing interpretation and deeper understanding of experimental data. More specifically, three main parameters governing the mechanical response of nanoparticles have been emphasized: firstly, we have the size as previously discussed concerning its effect on strength. The second parameter is the composition, referring to the choice of the elements (one, two or more) which can alter the atomic

SEM: Scanning Electron Microscope
FIB/PFIB: (Plasma) Focused Ion Beam

organization within the nanoparticle. Lastly, we have the parameter of shape. The following sections provide a detailed literature analysis of the impact of these quantities on both the plastic and elastic responses.

1.3.1 Plasticity

Size

Previously we have seen that dislocation nucleation controls mechanics at the nanoscale. More precisely, this phenomenon can be divided in two cases: heterogeneous and homogeneous nucleation. The first is nucleation linked to the existence of previous defects (such as normal defects or even surfaces). In contrast, the second refers to defect-free systems [24] and nucleation happens far away from surfaces.

More generally, to introduce a dislocation, an energy barrier needs to be overcome. The energy of the system has two main sources, mechanical and thermal. The mechanical energy is transmitted by an external loading, such as indentation, and the thermal factor helps reduce the mechanical barrier and introduce stochasticity in the process [9]. Following this reasoning, we can define two parameters that characterize the source of a dislocation: the athermal strength and the activation parameters. The first refers to the elastic limit at which dislocation occurs without the help of thermal fluctuation. Thus, by performing simulations at 0 K, we expect to find a fixed value with no statistical behavior. Conversely, at fixed temperature, we must consider the activation energy and the activation volume: it is a probabilistic measure of dislocation nucleation events with thermal fluctuation and an applied loading smaller the athermal limit [25]. The activation volume is a very important parameter because it allows the prediction of the nucleation event. For example, nucleation is more likely to happen in a corner than on a free surface because the activation volume on the surface is higher than the corner one. As a result, the size effect in defect-free nano-structure (nanopillars, nanoparticles...) is due to the reduction of the volume available for nucleation. In 1953, Cottrell proposed a predictive model for the critical stress of homogeneous nucleation of a dislocation loop under a uniform stress field [26]. This model forecasts an elastic limit of approximately $\sim G/30$, notably larger than experimental observations, but still substantially smaller than Frenkel's theoretical limit as discussed in Section 1.2.3.

The same model is used by *Mordehai et al.* in 2011 [27] to investigate the size effect in nanostructures. This model is distinct from previous ones as it incorporates a heterogeneous stress field, a concept introduced by Williams and Bogy [28] for studying stress around singularities. This approach is applied to tackle various problems, such as the nucleation

of misfit dislocations [29, 30]. As proposed in this work, the following equation 1.14 characterizes the stress (τ) within the nanoparticle:

$$\tau = A\sigma\left(\frac{d}{r}\right)^{\alpha}, \tag{1.14}$$

where r denotes a spatial variable, d represents the particle's size, A is a constant, and σ is the stress. The study carried out in [27] concentrates on Wulff-shaped nanoparticles, marking the first observation and elucidation of the size effect in nanoparticles of a few hundred nanometers. Figure 1.8 presents the experimental findings. This work suggests that the elastic limit is determined by the nucleation of a partial dislocation (Shockley $\langle 112 \rangle \{111\}$) at the top nanoparticle edges, a type of nucleation also observed in other pristine FCC systems, as is discussed further.

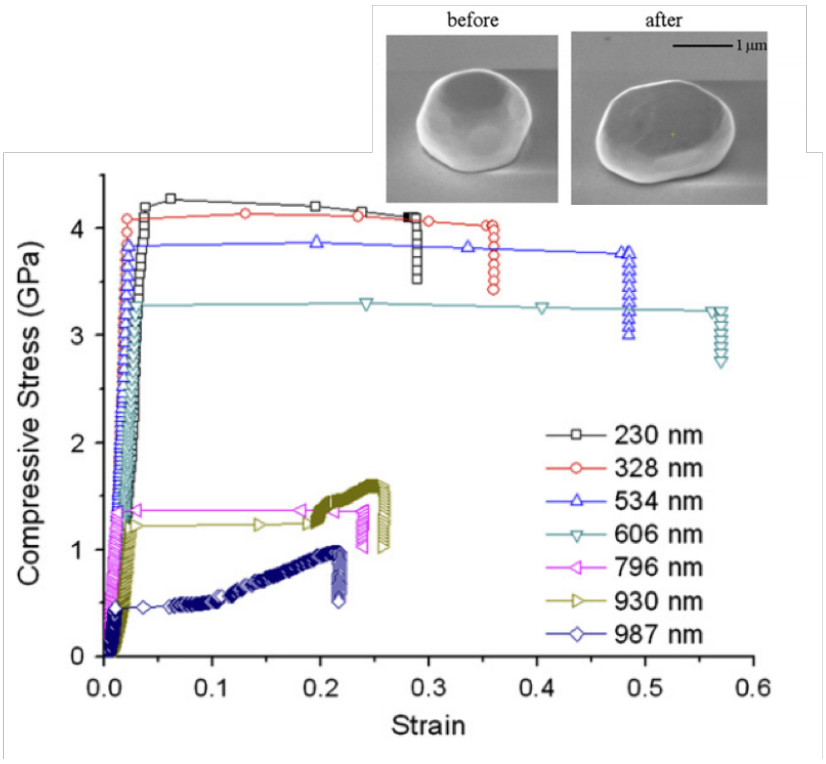

Figure 1.8: Size effect in microparticles. Experimental nanoindentation, stress and strain curve and real indented object. Figure extracted from [27].

Composition

In the literature, many works are focused on different types of transition metals, characterized by a FCC structure such as Au [27], Cu[31], Ni([32], strength record) Pt([33]) and generalized in 2016 by Feruz and Mordehai [34]. All different materials with the identical shape where exhibiting a critical stress given by equation 1.13 where the exponent α is the same for all nanoparticles and A depends on materials properties such as stacking fault energy and Burgers vector.

So far, only FCC-type metallic nanoparticles are discussed, but it is clear that other classes of nanomaterials are also studied. Let's take the case of Body Centered Cubic (BCC) metallic nanoparticles such as Fe [35] and Mo [36]. In this last work, an incredible stress value of 46 GPa is reached for a 110 nm faceted nanoparticle (Bulk value ~ 500 MPa). Moreover, a dependence on shape is observed (rounded or faceted nanoparticles) leading to a critical stress value independent of size. Concerning semiconductors (important for electronic applications), silicon is the most studied material. In 2003, *Gerbirich et al*. [37] found that silicon nanoparticles are super hard. Furthermore, they can be hardened and have an amorphous transition despite dislocating. In 2015 *Wagner et al*. discovered that Si nanocubes do not show size effect in elastic moduli, critical stress, and strain [38]. This shape dependence is deeply analyzed for cubes, rounded cubes sphere, and Wulff shape [39]. Again cubic system shows no size effect contrary to Wulff. Lastly, other materials are also studied to characterize their mechanical properties as a function of size such as ceramics as MgO [40] and Al_2O_3 [41].

In materials science, blending different elements can produce intermetallic compounds and alloys. These can typically exhibit properties intermediate between those of the pure constituents. The pursuit to engineer materials with precise properties and structures at the nanometer scale has kindled interest in alloy nanoclusters or nanoalloys [42]. As highlighted in the previous section 1.2.4, alloying is a potent strategy for modulating material properties, including the impediment of dislocation motion.

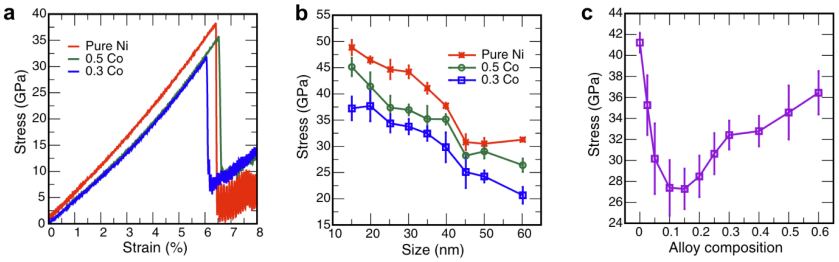

Figure 1.9: (a) Typical engineering stress-strain curves for a 40 nm particle. (b) Strength as a function of particle size. (c) Strength as a function of chemical composition for 35 nm particles. The error bars represent one standard deviation. Figure and caption extracted from [43]

Solid solution properties in bulk materials, can be reproduced at the nanoscale, but the mechanism that regulates plasticity is much more complex. One of the initial studies to characterize the effect of alloying at the nanoscale is conducted by *Chen et al.* in 2020 [44]. They illustrated a softening effect, i.e., a reduction in the critical stress σ_c, in alloy compared to pure materials, taking the NiFe nanowire system in traction as a case study. In the case of the NiCo system, a softer but tougher behavior is identified, as documented in [43], a finding that is in line with other research [45] on NiFe [46]. An illustration of this softening effect is presented in Figure 1.9, where it is clear that increasing the percentage of Co in a Ni matrix leads to earlier dislocation nucleation. These works converge on a simple idea: the

softening occurs due to an increase in local resolved shear stress. The idea of elastic softening inducing a plastic softening is excluded [43] (see Figure 1.10).

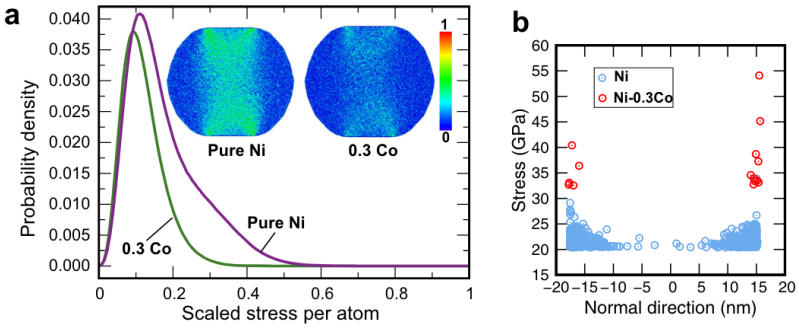

Figure 1.10: Characterization of stresses in nanoparticles under compression. Figure (a) MRAS (Maximum resolved shear stress) distribution scaled by the min-max in 35 nm particles of pure Ni and Ni-0.3Co. The inset shows the min–max scaled MRAS distributions in the particle cross-sections. Figure (b) MRAS in the particles as a function of the z-coordinate normal to the substrate (z = 0 at the particle center). Only the high end of the MRAS distribution is shown for clarity. Figure and caption extracted from [43]

In addition to solid solutions, metallic nanoalloys can generate other types of structure such as core-shell systems bringing many advances in various fields [42]. Concerning mechanical properties, the tuneable thickness of the shell represents a parameter that we can control and possibly drive the mechanical properties in the desired way. One example is proposed by *Kilymis et al* in case of SiC nanoparticles. [47] where very atypical phenomena happen, such as a confined plasticity in the core or shell of the nanoparticle and an increased strength, depending on the shell thickness.

The last and probably more futuristic class of material are multi-species alloys, from ternary systems to the wide class of High Entropy Alloys [48, 49]. The latter is a system where five or more different types of atoms are homogeneously mixed to improve the general mechanical (high strength and ductility compromises) in bulk system [50]. This can be simply explained by reminding us that plasticity is regulated by dislocation motion. Changing this motion implies improving mechanical properties; this highly disordered system helps this process incredibly. At the nanoscale, the study is still at the beginning since mastering their synthesis is already a challenge in itself. To my knowledge, only one study is published until now [51]. In this work, *Yan et al*. found similar results to binary alloys, a general softening due to the local stress induced by very different types of atoms in the nanoparticle.

Shape

According to *Feruz et al.*, [34], nanoparticles of similar shape (Wulff) exhibit the same size effect. On the other hand, cubic systems such as Si do not show size effects [38, 39], see Figure 1.11, different size effect are recovered by changing the shape.

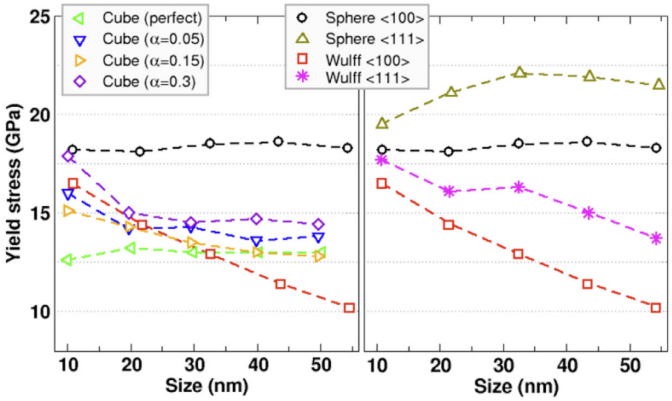

Figure 1.11: Shape dependent size effect: Yield stress as a function of size, at 5 K. Results for compressions along < 100 > are shown on the left graph, and those for spherical and Wulff-like nanoparticles and both < 100 > and < 111 > orientations are represented on the right graph. Dashed lines have been added between data points for visualizing trends. Figure and caption extracted from [39]

However, shapes are not always as predicted in theory, as they may have imperfections and defects. For example, sharp-cornered regions can be smoothed, resulting in a deviation from the simulated properties and a significant impact on the mechanics of the nanoparticle. One of the first studies on this topic is conducted on faceted and rounded nanowires by *Cao et al*. [52]. The study revealed that smoothing the edges of a square-shaped nanowire leads to delayed onset of plasticity. The basic idea is that the shape influences the stress distribution that controls nucleation. Square-shaped nanowires tend to nucleate at lower stresses than rounded ones.

In the 0D world, *Amodeo et al.* [53] observed a similar strengthening effect by rounding the edges of a cubic Ni_3Al system (from a cube to a sphere). Smoothing the corners changes the stress distribution in the nanoparticle, and dislocation nucleation occurs not only at the surface but also in the core of the nanoparticle (homogeneous nucleation). Similarly, *Sharma et al*. [36] highlighted a strengthening effect by smoothing the edges of faceted nanoparticles with Mo and by rounding the edges of a cube to a sphere with Si [39].

In a recent publication, *Zimmerman et al.* [33] proposed an experimental explanation for the nanoparticle shape effect. They modeled the yield stress as

$$\sigma_y = BD_{proj}^{i}Q^{j} \tag{1.15}$$

where B, i, and j are fitted constants. Q is the ratio between the top indented surface and the projected area of the entire nanoparticle on a plane perpendicular to the applied loading and D_{proj} can be related to the size. The model agreed well with the experimental results, confirming that shape is an important parameter to be controlled, along with size, in order to predict the mechanical properties.

1.3.2 ELASTICITY

In 2012, Armstrong and Peukert explored the size-dependent elastic properties of various structures such as cubic, Wulff-like, and spherical

shapes. Their work highlighted clear effects below 20 nm and a high dependence on the specific shape of structures [54]. In the studies that followed, researchers carried out nano-indentation experiments on nanoparticles, observing that the effective Young's modulus values differed from those of bulk materials [55, 56]. By 2016, an analytical models is developed, describing the variation in elastic responses when transitioning from a cube to an octahedron, which are detailed in [57]. In Figure 1.12, you can find the results of the model together with the MD results.

The effective Young's modulus is the elastic response of non-homogenous and non-symmetric object. A better introduction on this parameter is proposed in Chapter 2

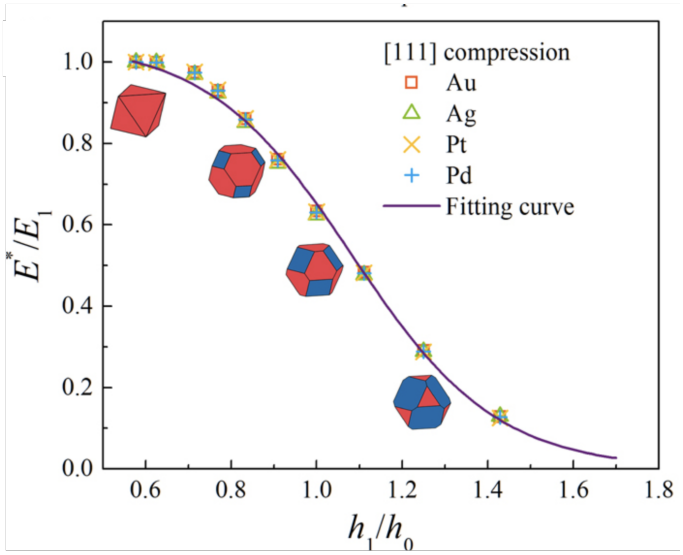

Figure 1.12: Dependence on shape of the elastic response in nanoparticles in the [111] direction for different material. The value of the effective response is normalised and h is a parameter allowing to identifying the nanoparticle shape. Figure extracted from [57].

When it comes to numerical methods, Molecular Dynamics remains the preferred tool for analyzing structural properties at the nanoscale. However, the Finite Element analysis also offers a reliable alternative. While not always the first choice, finite elements have proven to be an useful method in nanoscale research. It has been used in a range of research areas including the modeling of plastic relaxation in SiGe/Si heteroepitaxial nanoislands[58–60], studying both elastic and plastic behavior through dislocation dynamics simulations [22], calculating stress distribution in nanoparticles during indentation [27, 36], and understanding surface strain in core-shell nanoparticles [61], with a comparison with molecular static (MS), as function of the size. Similarly the previous work of *Yang et al.* [57], proposed a comparison between the two method (FE and MS) changing the shapes, with a fixed size, and looking at the effective Young's modulus.

1.4 Electronic properties of deformed nanoparticles

Deformed nano-materials have proven to be very useful nowadays since strain can be used as an additional degree of freedom to control and engineer devices. Probably the most known examples belong to

the semiconducting world where the transport properties of CMOS in the sub-130 nm range are improved by 70% by inducing strain in the channel. This technology isadopted in devices produced by ADM, IBM, and Intel [62, 63]. Strained materials become interesting in the catalytic world by shifting the attention onto metallic objects where mechanical deformations can enhance the catalytic properties such as fuel cells [64], nowadays used for energy production, converting hydrogen to water. However, one of the challenges of such applications lies in the oxygen reduction reaction (ORR) at the cathode. This reaction is typically catalyzed by platinum which is expensive and rare . To overcome these limitations, researchers are exploring methods to improve fuel cell performance while reducing the quantity of platinum used. One promising approach is manipulating surface strain at the interface, which has proven to be highly effective [65].

Interstingly, the strain can be controlled and optimized with two main different techniques. The first way is through engineering the structure by changing the morphology (different shapes or even size) [66]. Indeed, surface strain arises naturally due to surface relaxation, resulting from the lower coordination number at the surface compared to the bulk. Some shapes are fascinating because they are naturally defective, icosahedron or decahedron, and possess intrinsic twin boundaries that induce surface strain [67, 68]. Considering alloys, surface atoms different from platinum induce local strain due to a mismatch in atomic parameter [69], or even to create core-shell structures [61]. The second way consists in using external forces where modifying some external conditions can induce changes in the lattice parameter and then tuning certain chemical and physical properties. For instance in catalytic reactions, sub-surface gas can apply pressure and then induce strain in the material as well as bending a substrate on which the catalyst is deposited. Additionally, introducing ions such as doping can cause lattice distortions, leading to strain.

In this work, the focus is on investigating the effect of mechanical deformation on the catalytic reactivities of metallic nanoparticles. The following section presents the concepts and theoretical formalism that enable the understanding of how electron properties are modified by mechanical constraint, and how this might relate to catalytic properties.

1.4.1 The tight-binding formalism

When analyzing the electronic problem, we can go back to the crystal Hamiltonian seen in Section 1.1, from which we derived the electronic Hamiltonian:

$$H = V_{ee} + V_{Ie} + T_e \tag{1.16}$$

In this equation, V_{ee} represents the electron-electron interaction term, V_{Ie} represents the electron-ion interaction term, and T_e represents the kinetic energy term.

The tight-biding approximation (semi-empirical) is a good compromise in terms of computation time and accuracy (compared to DFT, for example). It is therefore very well suited to investigate the periodic systems, but one of its strength relies also on non-periodic systems such as nanoparticles or defective structures. This formalism neglects the electron-electron interaction and assumes that the electron wave functions can be approximated as a linear combination of atomic wave functions (ϕ_α) centered around each atomic site in the crystal lattice ($\mathbf{R_i}$). This is called the Linear Combination of Atomic Orbitals (LCAO) method. The wave function is expressed using Dirac notation:

$$\Psi(\mathbf{r}) = \sum_i \sum_\alpha a_{i,\alpha} \phi_\alpha(\mathbf{r} - \mathbf{R_i}) \rightarrow |\Psi\rangle = \sum_i \sum_\alpha a_{i,\alpha} |i, \alpha\rangle \tag{1.17}$$

where the $|i, \alpha\rangle$ stands for the orbital of type α at site i. Assuming one orbital per atom and projecting onto one state $\langle j|$ while imposing the orthogonality of the atomic states ($\langle i|j\rangle = \delta_{i,j}$), we can derive the tight-binding Hamiltonian:

$$H = \sum_i |i\rangle \, \epsilon_i \, \langle i| + \sum_j |i\rangle \, \beta_{i,j} \, \langle j| \tag{1.18}$$

As we can see, H comprises two terms. The first term, known as the atomic level, corresponds to the energy level in an isolated atom, denoted as ϵ_i, and is given by $\langle i|H|i\rangle$. The second term involves the hopping integrals, which represent the wave-function overlap, $\beta_{i,j}$, between sites i and j. This parameter can be determined by evaluating the integral $\langle i|H|j\rangle$ or can be fitted based on experimental or ab-initio data, as adopted in this study.

The concept of hopping integrals has been generalized to include all orbitals - s, p, and d - and account for all angular dependencies, building on the work by Slater and Koster [70, 71]. Various types of bonds can form between orbitals while preserving angular momentum. For instance, $d - d$ orbitals can exhibit σ, π, and δ bonds. Similar bonding is possible for s and p orbitals, as well as for inter-atomic bonds such as $s - p$, $s - d$, and $p - d$. These values are typically derived from DFT or experimental data [72] and utilized to reconstruct the interactions of all orbitals through Slater-Koster coefficients.

For this work, it is interesting to introduce the *ldos* since this quantity is analyzed to understand the electronic properties of deformed nanoparticles. A local density of states description is particularly useful in case of nanoparticles where the behavior of well-confined

regions such as surfaces is relevant in deformed materials. The local density of states for a generic atom i is:

$$d_i(E) = \sum_k \mid \langle i|\Psi_k\rangle \mid^2 \delta(E - E_k) \tag{1.19}$$

This expression states that every contribution to the density of states $\delta(E - E_k)$ is weighted by the probability $\mid \langle i|\Psi_k\rangle \mid^2$ of finding an electron in a particular base state $|i\rangle$ and the summation spreads over all the k-states with energy E_k and wave function Ψ_k that is a linear combination of atomic states $|i\rangle$. The expression for the total density of states can be reconstructed following $D(E) = \sum_i d_i(E)$.

1.4.2 From local density of states to catalytic properties

Fom Nørskov's work, a direct link has been established between the adsorption of atoms or molecules on a surface of a catalyst and its local electronic properties [73, 74]. The core idea suggests that the reaction activity of specific sites present at the surface is influenced by the center of mass (or first momentum) of their local density of states where the momentum of order p, denoted as μ_p, is defined as:

$$\mu_p = \int_{-\infty}^{+\infty} (E - H_{ii})^p \cdot d(E), dE \tag{1.20}$$

The first moment (μ_1) corresponds to the center of mass or mean; the second moment (μ_2) represents the width or variance, and so on.

In the context of transition metals, the *ldos* exhibits a broad, semi-filled s band and a more narrow d-band, the occupancy of which depends on whether the material is a late or early transition metal. The narrowness of the d bands is a result of the coupling matrix element (V_{dd}) associated with localized d states. Notably, the bandwidth correlates with V_{dd}, a concept grounded in tight-binding theory [71].

During the interaction of an adsorbate state with the d electrons of a surface, bonding and antibonding states frequently emerge, similar to the two-state problem. If the band is low and wide, a single resonance appears at the band's base (Figure 1.13a). However, if the bandwith is small, a distinct antibonding state materializes above the band. If these antibonding states are situated above the Fermi level, they are vacant leading to stronger bonds as more of these states are unoccupied. In simple terms, a narrower *ldos* correlates with stronger absorption, and this is directly indicated by μ_1. When μ_1 is closer to the Fermi level, the band is narrower and the adsoprtion is favoured.

There exist multiple strategies to adjust the μ_1 parameter, including moving along the periodic table (vertically or horizontally) or

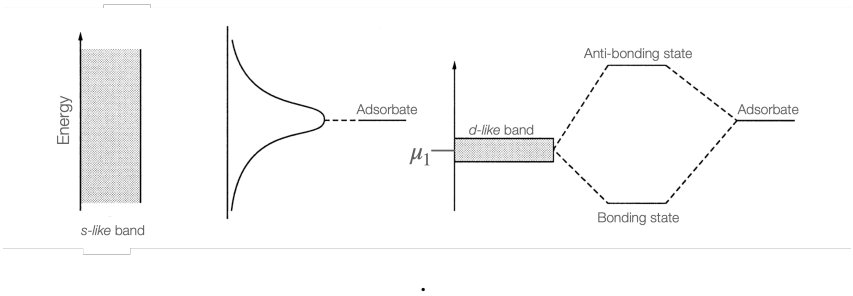

Figure 1.13: The local density of states of an adsorbate atom in two limiting cases: (a) for a broad surface band (such as *s* band) ; (b) for a narrow metal band (such as transition metal *d* band). Figure extracted from [73]

manipulating structural parameters such as strain or coordination. Transitioning horizontally, for instance from silver to zirconium, causes an upward shift of the d bands and a reduction in occupancy of the antibonding states, enhancing absorption energy. The interesting part is that the relation between chemisorption with μ_1 is linear (different μ_1 are obtained with different metals [73].)

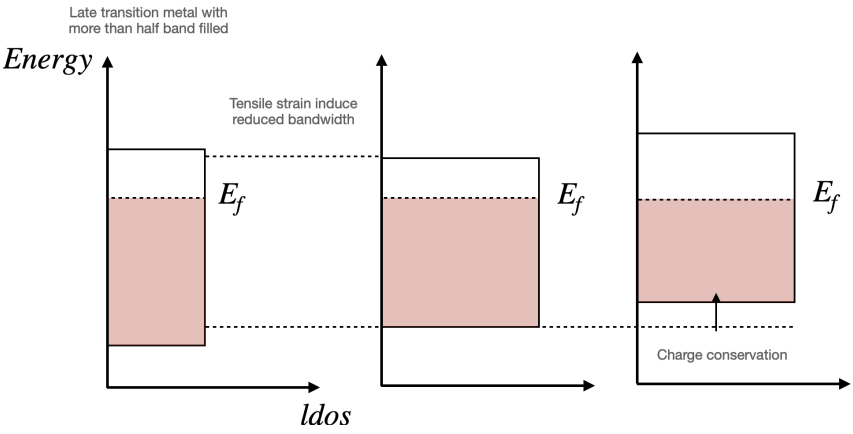

Figure 1.14: Effect of strain on the density of states, simplified as a rectangle. Tensile stress reduce the hopping integral reducing the distance between the Fermi level and μ_1. Figure readapted from [65]

Figure 1.14 illustrates another method to modify μ_1: the use of strain. This approach can narrows the d-band and moves the *ldos* center of mass nearer to the Fermi level by directly increasing the interaction strength with the adsorbate. In Figure 1.15, such effect is clear. The tensile strain increases the chemisorption energy linearly of oxygen on a Ruthenium surface [73]. In a similar manner reducing the coordination number i.e. passing from a surface to an edge or a vertex bands get narrower and μ_1 moves closer to the Fermi level, increasing again the absorption properties.

Tensile strain induce narrows the *ldos* because the distance among atoms is reduced, with a corresponding lower V_{dd}. Compressive strain induced *ldos* spreading, given the increased hopping integral.

One way to introduce nanoparticle strain is to work with a core-shell system. The lattice parameter mismatch induces tensile or ductile strain at the surface, depending on the chosen material. In [61], a combination of Molecular Static and Finite Elements calculations is

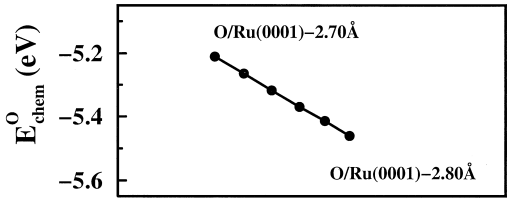

Figure 1.15: Effect of strain on the absorption energy of oxygen on a Ruthenium surface. Tensile strain induces a linearly increased energy. Figure extracted from [73].

used to understand surface strain at the nanoscale. After validating the two methods, FE is applied to find the optimal configuration (size and the number of layers of Pt at the surface) with the best ORR activity. In Figure 1.16, you can observe at the left the stress dependence on the size and the type of core-shell system. At the right, a volcano plot is presented showing that compressive stress initially induces improvement of the activity (as previously explained) and then a reduction.

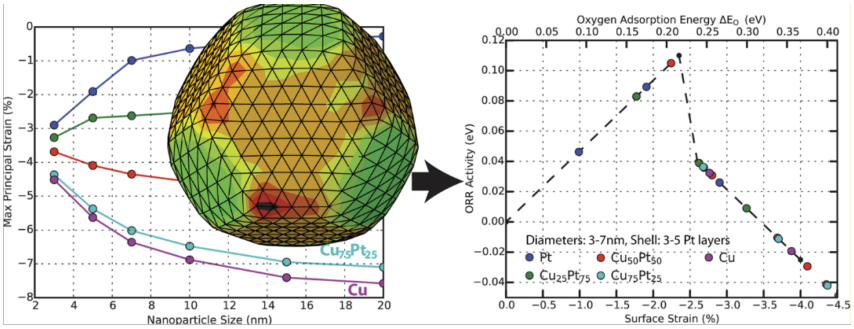

Figure 1.16: Tuning absorption properties of a nanoparticle by playing with the surface strain, imposed by the core-shell structure. The results are produced also with FEM. Absorption properties increase with the compressive strain, the ORR activity shows the typical volcano plot. Result extracted from: [61]

Now that a direct connection between absorption properties and the *ldos* momentum, a parameter we can control, it is possible to design a new structure to maximize the catalytic properties [75]. The connection between absorption and catalysis is not straightforward. Both too strong and too weak binding between the substrate and adsorbate can hinder the reaction, and this is what is observed in the vulcano plot, but this won't be object of this discussion. An example comes from [76], where a compressively strained nanoparticle increases the performance by down-shifting the center of mass (further from the Fermi level), thus reducing the absorption strength and suppressing the adsorption of OH on the surface that blocks surface sites.

1.5 Aim of the present work

As seen in this overview, nanoparticles are captivating objects. Understanding and mastering their mechanical properties is vital for various applications. This subject garners significant attention from the international community, but there are still many aspects to explore.

In this work, spread over four chapters, the mechanical and electronic properties of nanoparticles are delved into. The initial three chapters center on the elastic and plastic responses of pure metallic and bimetallic NPs. Emphasis is placed on how the nanoparticles' *size*, *shape*, and *composition* influence their mechanical properties, including *stiffness* (elasticity), *strength*, and *ductility* (plasticity).

Consistently with some prior work, in Chapter 3, the elastic properties of nanoparticles are computed for various transition metals

(Au, Cu, and Pt). This analysis delves into the role of shape and size in determining both effective and local elastic responses. Two different simulation techniques, Molecular Dynamics and Finite Element Method, are employed. Molecular Dynamics, a commonly used tool at the nanoscale for determining structural and transport properties, is detailed in Section 2.3. The Finite Element Method, which addresses a wide range of problems using partial differential equations, is described in Section 2.4. This research not only deals with the properties of nanoparticles but also compares the results of both techniques. This comparison highlights the efficiency of the Finite Element Method at the nanoscale. Due to its shorter computation time, it enables comprehensive analysis of nanoparticles.

Chapter 4 explores plastic properties, emphasizing the shift from elastic to plastic regimes via critical stress, adopting the methodologies from Chapter 3. The exploration starts with pure transition metals and evolves to encompass bimetallic systems. Following this, Chapter 5 provides an exhaustive evaluation of the elastic and plastic behaviors of the CuAu alloy across a spectrum of ordered and disordered structures.

To conclude, Chapter 6 investigates the behavior of the local density of states under varying loading conditions. It establishes a correlation with the nanoparticle's reactivity following Nørskov theory. For this purpose, a specialized code for Tight Binding analysis is crafted, detailed in Section 2.5, and then validated via DFT calculations.

Methodologies 2

This chapter aims to provide insights into the techniques employed for investigating mechanical and electronic properties at the nanoscale. The initial Section offers a comprehensive overview of nano-indentation techniques, discussing the common experimental methods currently utilized (Section 2.1). This is followed by an introduction to the subject of our investigation, namely nanoparticles, with particular emphasis on their shape and size which play a central role in our analysis (Section 2.2). The subsequent sections present the fundamental principles of Molecular Dynamics (MD) (Section 2.3) and the Finite Element Method (Finite Element Method (FEM)) (Section 2.4). These sections specifically focus on how these methods can be employed to replicate nano-indentation experiments.

Finally, the chapter shifts its focus to electronic properties. Section 2.5 introduces the methodology used to calculate the local density of states based on the tight-binding Hamiltonian.

2.1 The nano-indentation experiment

As seen for bulk material (Section 1.2.2), where with an indenter of a given shape a load is applied to a specimen to extract a force-displacement curve, at the nanoscale where sizes are reduced, mechanical properties are probed using pico-indenter [33, 38, 77]. This experimental setup allows for simultaneous imaging (SEM, TEM... [1]) and nanomechanical testing. The procedure involves applying a controlled compressive loading to the surface of a nano-object using a hard indenter (typically made of diamond and available in various shapes) such as a flat punch or a more rounded shape. The indenter moves at speed of the order of nanometers per second, and the magnitude of the loading is usually below approximately 10 mN. In Figure 2.1 an example for an extremely small silver nanoparticle (20 nm) is proposed. By performing nano-indentation experiments, researchers

1: TEM: Transmission Electron Microscope

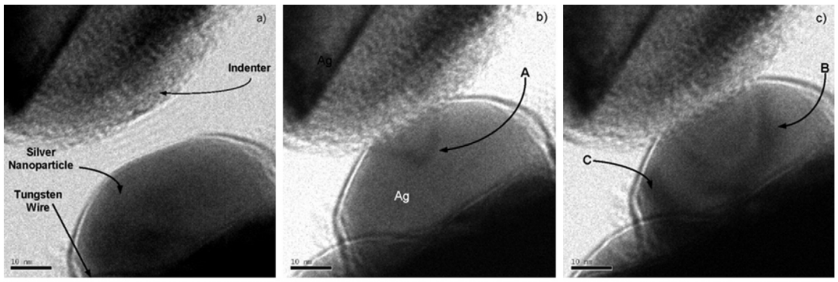

Figure 2.1: TEM images taken from the diffraction contrast of an in situ nano-identation experiment. Figure (a): probe and the nanoparticle before the nano-indentation experiment. Figure (b-c) during deformation. Figure extracted from [78].

can obtain force-displacement curves. The stress (force divided by area) and strain values are obtained through area calculations using SEM imaging, while the nanoparticle's height (the size) measurements are typically obtained using an Atomic Force Microscope (AFM). As the area calculation is performed in real-time during the experiment, the resulting stress-strain curves are referred to as true stress-strain curves, and in this study we refer to them simply as stress and strain.

From an experimental standpoint, numerous factors can influence the results and hinder reproducibility. For example, residual roughness on the samples or on the indenter can alter the stress distribution within the nano-structure. Other factors include: accurate area calculations, the presence of residual defects and the strain rate sensitivity. These are just a few symbolic examples to provide a general understanding of the experimental conditions and techniques involved. Of course, the topic itself is much more complex. In this context, modeling comes into play, aiding in understanding the physics of nano-mechanics, and facilitating the reproduction of experimental conditions as closely as possible.

2.2 Nanoparticles

Nanoparticles are systems of finite size that cannot be considered simple fragments of a crystalline solid, thus adopting structural arrangements that differ from those of bulk [79]. In this context, Wulff established a well-known rule to describe the equilibrium forms of free polyhedral crystals [80]. Among all the possible identified structures, we focus our study on morphologies experimentally observed, i.e., truncated cube, cuboctahedral, and Wulff shapes.

In Figure 2.2a, nanoparticles chemically produced are presented; this technique allows perfect shape control. From left to right you can observe cubes, cubo-octahedra and octahedra [81, 82]. The particular case of icosahedral and other non crystalline NPs, common for small aggregates, are not considered here since they are unstable for particles larger than 4-5 nanometers [83].

In the domain of nano-mechanics, nanoparticles usually have sizes in the range of 50-1000 nm and are produced with top-down approaches [33, 82]. FCC metals usually show truncated-octahedral shapes, exposing the (111) and the (001) facets. Nevertheless, many different shapes and sizes have been probed over the years producing various spectrums of different configurations.

From a numerical and atomistic standpoint, nanoparticles have a limited size due to the high computational cost for systems with more than 10^6 atoms, and the control over shape is reached by tuning the surface energies. In the present work, the tool employed for structure

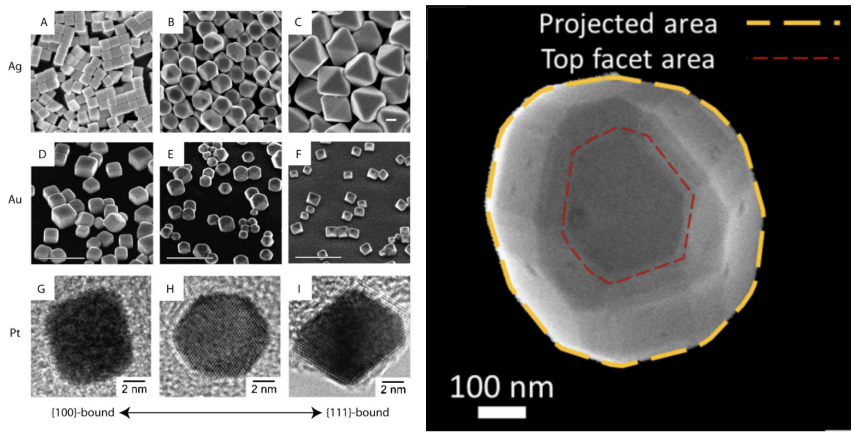

(a) (b)

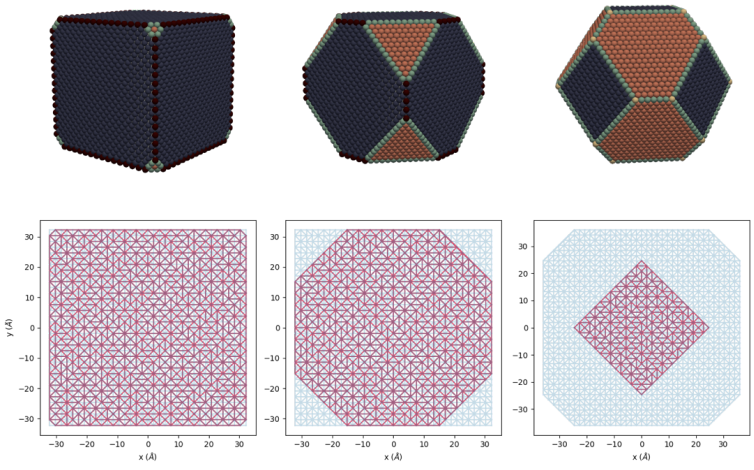

(c)

Figure 2.2: Figure (a): Chemically produced nanoparticles of different material (Ag, Au and Pt) with many different shapes, from cubic to octahedral shape. Figure extracted from [81] Figure (b): Shape parameter extracted from an experimental SEM image of a NP corresponding to the ratio of the top surface area to its projection on the x and y plane. Figure extracted from [33]. Figure (c): Shape parameter extracted from numerical (001) nanoparticles. At the top some of the different possible nanoparticles, truncated cubes and a truncated octahedron and, at the bottom, the top surface area (in red) and the projected area (in blue).

generation is the Atomic Simulation Environment (ASE) [84], used as a Python package to provide a fast and effective way to generate nanoparticles with different sizes and shapes. As seen in Figure 2.2a., the shapes addressed in the present work are based on the FCC lattice, leading to the presence of outer facets of (111) and (001) orientations. NPs with sizes (d) ranging from 4 to 25 nm (around 10^2 to 10^6 atoms, respectively) are considered. More precisely, d is defined as follows:

$$d = 2 \cdot \left(\frac{3V_{eff}}{4\pi} \right)^{1/3}$$

with V_{eff} being the effective volume of a sphere equal to the exact volume of the considered nanoparticle. Thanks to this definition of d, the size is strictly related to the number of atoms of the NP and allows us a more methodical study of different shapes at the same size.

To distinguish between the different shapes of nanoparticles, a descriptor can be defined as done in a previous study by *Zimmerman et al.* [33], based on the calculation of the top surface area, and the nanoparticle

shape projection on the x, y plane. In Figure 2.2b, the extraction of the top and projected areas from a SEM image by *Zimmerman et al.* is illustrated. From these values, an effective radius is determined, and the shape parameter is calculated by taking their ratio as follows:

$$G = \frac{d_{top}}{d_{proj}} \tag{2.1}$$

Figure 2.2c displays (001) oriented faceted nanoparticles, with (001) direction upwards: the top surface highlighted in red and the projected area in blue. As the structure evolves from a truncated octahedron to a cube, this parameter changes from $0 \rightarrow 1$. The Wulff structure is a unique form of the TO class, its truncation is determined by surface energies. For gold nanoparticles oriented along the (001), the TO ranges from 0 to 0.45. At G = 0.45 we have the cubo-octahedron, and for larger G values TC, as shown in Figure 2.3. The Wulff structures have around $G = 0.14$ (this value depends on the surface energies considered).

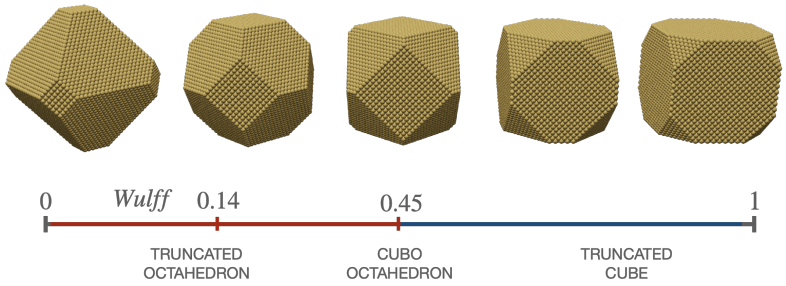

Figure 2.3: Different shapes with the corresponding shape parameter G.

2.3 Molecular dynamics

In this Section, we explore the application of MD calculations to nano-indentation studies. MD is a computational technique that simulates atomic behavior, while nano-indentation measures nanoscale mechanical properties. Below we provide an overview of MD principles followed by the nano-indentation procedure. The final part of this section discusses the importance of the inter-atomic potential, the main families, and the choice for our study.

2.3.1 Theory

Molecular dynamics is a classical simulation technique that can be used to compute transport and equilibrium properties in a many-body problem. By classical, it is meant that the equation of motion of atoms is completely classical, i.e. the Newton's equation of motion. This approximation is excellent when dealing with a large system and negligible quantum effects on motion. One of the interesting characteristics of MD is that simulations are similar to real experiments,

as to prepare the sample, waiting for equilibrium and the motion of atoms.

The basic idea is that every atom interacts with all other crystal atoms through an inter-atomic potential. Therefore each atom feels the potential contribution of the whole structure. For a given configuration of atoms, the computed potential energy can be classically related to force and, through Newton's second law, to the position. This process can be repeated iteratively until equilibrium, a condition in which the resultant of the force acting on atoms is close to zero, is achieved. Each MD code must follow a few basic steps:

- **Initialization** At the beginning of the simulation, the problem must be initialized, i.e., the initial position $\boldsymbol{r}(t)$ and the velocity $\boldsymbol{v}(t)$ of atoms must be defined. The initial position will determine the final structure, and the velocity is defined by temperature thanks to the energy equipartition theorem.
- **Force Calculation**. What we want to calculate is the force $\boldsymbol{f}(\boldsymbol{r})$ that acts on all the elements of the system to observe its evolution. This is done by considering the gradient of the potential $U(\boldsymbol{r})$:

$$\boldsymbol{f}(\boldsymbol{r}) = -\nabla U(\boldsymbol{r}) \tag{2.2}$$

  Whereas for a potential acting on one atom, we should consider the contribution of all the $N-1$ atoms in the structure. This is the most time-consuming part of the whole MD simulation; in a system where we consider that each atom interacts with all the system atoms, the computing time will scale with N^2. To avoid this problem, the contribution of an atom is considered only if the distance is smaller than a fixed cutoff distance.
- **Integration**. Once the forces on each atom are calculated, time integration is fundamental to compute the new position $r(t \pm \Delta t)$. It can be done numerically and the most used choice is the **Verlet Algorithm** where considering the Taylor expansion around t, we can derive:

$$\boldsymbol{r}(t + \Delta t) = 2\boldsymbol{r}(t) - \boldsymbol{r}(t - \Delta t) + \boldsymbol{a}(t)\Delta t^2 \tag{2.3}$$

  The acceleration ($\boldsymbol{a}$) can be derived by the force ($\boldsymbol{F} = m\boldsymbol{a}$), so the position of any atom at the time $t + \Delta t$ depends only on the force and not on its velocity. This is the most simple, commonly used and effective integration technique, even if others exist [85].

With this scheme, energy is conserved: it is an NVE ensemble, where the three letters stand for a constant number of particles, constant volume, and constant energy. For our analysis, we need to introduce a different type of ensemble where the temperature is constant. From a statistical point of view, this means bringing the sample into contact

with a thermal bath. Thus, the atom's energies follow the Boltzmann distribution and, on average, the temperature is equal to the thermal bath. There are two main thermostat types, *Andersen* and *Nose-Hoover*. The first can be considered as a half-Monte Carlo method because the interaction with the thermal bath is simulated by introducing random force on atoms. In the second, and most used one, the effect of the bath is completely deterministic thanks to the extension of the Lagrangian, where the effect of the temperature is reproduced with artificial coordinates and velocity.

Nowadays, molecular dynamics is a well-established simulation technique. Therefore, to analyze the mechanical properties of nanoparticles in this work, we choose to use the LAMMPS code, which is widely used in the scientific community. LAMMPS stands for Large-scale Atomic/Molecular Massively Parallel Simulator, developed by the Sandia National Laboratories [86].

2.3.2 Nano-indentation simulations based on MD calculations

To model NPs compression via the nano-indentation procedure, MD calculations are the most widespread technique [23, 27, 32, 53]. In this procedure, the Verlet algorithm with a timestep of 1 fs, combined with the Nose-Hoover thermostat at 0.01 K, integrates equations of motion in the NVT canonical ensemble. The size of the simulation supercell in all directions must be large enough to avoid artifacts due to interaction between images caused by periodic boundary conditions. Before compression, the NPs are relaxed at 0.01 K until convergence of the total energy (a relative error of $\epsilon_r = 10^{-5}$ is considered) to get the equilibrium configuration.

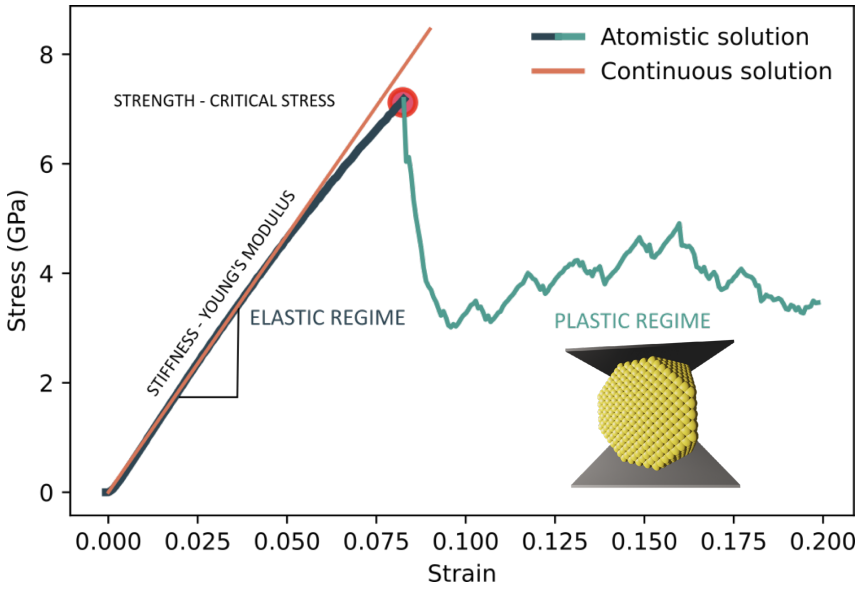

Figure 2.4: Typical stress and strain curve, together with the configuration used for the indentation, two flat indenter compressing a nanoparticle.

As seen in Fig. 2.4, the indenter and substrate are simulated with two rigid infinite planes parallel to the (001) or (111) facet of the NP. The effect of an indenter is implemented by introducing fictitious repulsive forces to be integrated into MD simulation. In the present studies, we used a quadratic repulsive force: $F(r) = -K(r - R)^2$ with $K = 1000$ eV Å^{-3} and R corresponding to the indenter position in agreement with previous works [22, 27]. During the simulation, we use two moving indenters (bottom and top plane in Fig. 2.4), each of them applying a strain rate of about $3 \cdot 10^7 s^{-1}$ which corresponds to an indenter velocity of roughly 0.06 to 0.6 m s^{-1}. As stated by *Mordehai et al.* [27], the velocity has to be less than the speed of sound in the considered material to allow the atoms to reorganize before a new displacement is imposed. [2]

2: $v_{sound} = 3240 ms^{-1}$ in gold

Choosing the right temperature is crucial. In our scenario where we are working with very low temperatures, we are moving away from the typical experimental settings. As discussed in chapter one, this leads to a loss in the random nature of dislocation nucleation. Studies have shown that mechanical properties, specifically dislocation nucleation and the corresponding critical stress, can vary significantly at finite temperatures and with different strain rates, except at 0 K where the results converge[87].

The force applied by the indenter is calculated by default by the LAMMPS options and can be monitored step by step. Knowing also its position, size, and surface area, the stress and strain curve can be reproduced. The size is defined as the height in the z direction to be coherent in the strain definition. Care is needed for the area calculation; its value can deeply influence the slope and the critical stress even without changing the compression's physics. Given that our interest relies more on the physics than on breaking new records in the critical stress value, to correctly compute the indented area a Delaunay triangulation of the top atoms, at a distance smaller than 1 from the indenter is performed, as described in previous works [27, 39].

The typical results of a nano-indentation experiment obtained with MD are sketched in Figure 2.4. During the very early stages of the loading, the stress variation is initially linear corresponding to an elastic regime. The slope of this curve can be called in many different ways; in a bulk material it is the Young's modulus or sometimes even the stiffness. In this work, we will talk about effective Young's modulus E_{eff}, since we will also extract it in inhomogeneous materials and nanoparticles of different shapes, where the classical definition is not properly valid. Then, the stress has a peak value, which defines the yield point corresponding to the largest stress that the NP can handle in the elastic regime. Above this point, a meaningful stress reduction is noticed, indicating the onset of plastic deformation. More precisely, the emergence of plasticity in NPs results from the

heterogeneous nucleation of dislocations from the contact surfaces. This drop is not only due to the nucleation but depends on how the loading is controlled. Experimental results are carried on by controlling the force acting on the nanoparticle through the indenter and looking at the displacement. With this type of control, when nucleation occurs, flat and constant stress would be recovered (see Figure 1.7), until a strain burst is observed, causing the destruction of the nanoparticle. Due to the burst, nano-structures rarely show a ductile behavior or a hardening process in experimental sample. When modeling, experiments are reproduced in a displacement-controlled mode, where the indenter is moved down a certain amount every step and the force is calculated. In this condition when the first dislocation is nucleated in a defect-free nanoparticle, we observe the typical drop of Figure 2.4.

2.3.3 Interatomic potential

In Chapter 1, we introduced the crystal Hamiltonian and the different ways to simplify it for a given application. The best approach for atomistic simulation is to develop an effective potential that considers the interaction among ions and electrons. There are four main techniques for constructing such a potential, as shown in Figure 2.5: pair potential, cluster potential, pair functional, and cluster functional; usually more the strategy is complex, and more it can be applied to general different problems. Typically, longer computation times are required for the Functional Cluster, while a simpler approach, such as the Pair Potential, can be used for a limited application case. A compromise is represented by Pair Functional and Cluster Potential where the computation time is still reasonable, but a good level of accuracy can be achieved [5, 88–90].

A pair potential model is a simple approach that works well within a certain range of applications. An example of this is the Lennard-Jones potential, which relies solely on the distance between atoms ($V(R_{ij})$) and requires two parameters to be tailored for specific problem. A more effective approach is the cluster potential, which introduces a many-body interaction term to the pair interaction. The three-body interaction, which requires angular forces to stabilize the structure not accounted for in the pair potential, is the first and most common approximation (as seen in Figure 2.5). The Stillinger-Weber potential is a well-known example of this type, developed to analyze liquid silicon and phase transitions [91].

Our case of study centers on the mechanical properties of nano-structures, with a particular focus on phenomena like defect introduction and motion linked to broken bonds. When a bond breaks, there is a substantial shift in electron density surrounding the atom. To more accurately capture this change, pair functionals have been

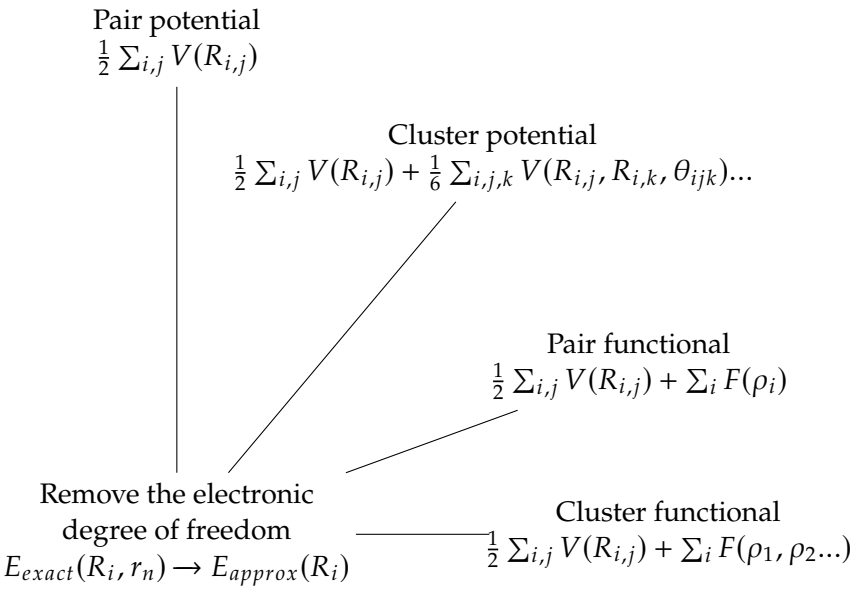

Figure 2.5: Different families of interatomic potential.

introduced. These functionals use a parameter to describe the electronic structure around the atom. The functional is represented as $F(\rho)$ in Figure 2.5, where ρ is a parameter that characterizes the local environment. There are two main types of potentials in this class: the first uses the tight-binding formalism to determine the shape of the functional and the local parameter, which is the local electronic density bandwidth ($\rho \rightarrow \mu_i$ second moment) in the SMA [89, 92]. The second type constructs the bonding theory around the electronic background density (n_i), known as the Embedded Atom Method (EAM) [93]. The embedding function, denoted by $F(\rho)$, represents the gain in energy when an atom is embedded in a background charge density $\rho \rightarrow n_i$ (local electronic density of atom i). The function is typically constructed with several fits of the $n_i = \sum_{j \neq i} n_{at}(R_{ij})$, where n_{at} is some radial function.

Local environment function:

$$\rho_i = \sum_{i \neq j} f(R_{i,j})$$

where f is pairwise function, that represents the electronic density decay at a given site.

In this study, the SMA potential are the preferred choice. The work of Ducastelle [89], started in what later became the LEM laboratory, and it is based on the moment theory. Moreover, the SMA potentials are simple in their form and, above all, in connection with the quantum physics of crystal especially in the case of transition metals (considered here).

The model assumes that the cohesion in a solid is determined by how the d-band is filled, as proposed by Friedel [71]. This prediction is based on approximating the local density with a simple rectangular shape.

$$F(\rho) \rightarrow E_{bond} = 2\int (E - \alpha) dos(E) dE \rightarrow \alpha\sqrt{\mu_2(i)} \qquad (2.4)$$

In the tight-binding formalism, μ_2 is strictly related to the hopping

integral and the coordination number, establishing a direct connection from the quantum mechanical world to the macroscopic one.

Considering only the bonding energy, the crystal would implode. This does not happen because repulsive forces exist due to ion repulsion. For this contribution, the choice is much simpler and a pair exponential potential is chosen. The SMA potential finally shows as follows:

$$\frac{1}{2}\sum_{i,j} V(R_{i,j}) + \sum_i F(\rho_i)$$

$$\Downarrow$$

$$\frac{1}{2}\sum_{i,j} V(R_{ij}) - \sum_i \alpha\sqrt{\mu_2(i)}$$

$$\Downarrow$$

$$\sum_{ij} A\cdot\exp\Big[-p\big(R_{ij}/r_0-1\big)\Big] - \sum_i \sqrt{\sum_j \xi^2 \exp\Big[-q\big(R_{ij}/r_0-1\big)\Big]}$$

where A and p are fitted parameters on the repulsive component and ξ and q on the attractive one, with r_0 the lattice parameter. We can observe the two components in Figure 2.6, with the predominant attractive behavior at larger distances and a repulsive behavior dominating at short distance: the sum of the two contributions results in the red curve, where an equilibrium position at a given atomic distance appears. In the following chapters, the parameter values are provided for the materials or the alloys of interest.

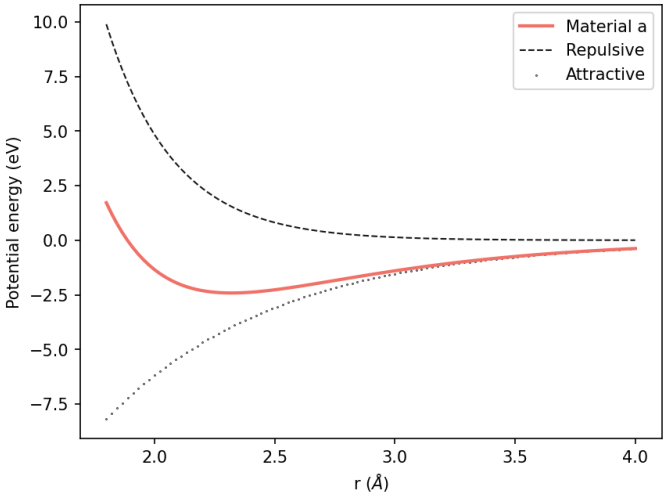

Figure 2.6: Sketch of an interatomic potential, where the two contributions (attractive and repulsive) are highlighted.

2.4 FINITE ELEMENT AT THE NANOSCALE

This Section aims to provide a detailed description of the FE method employed for extracting the mechanical properties of nanoparticles.

The objective is to replicate the experimental nano-indentation experiment by calculating the displacement field, stress, and strain within the nanoparticle under a given displacement applied at boundary conditions.

The Section is divided into two main parts. The first one provides an overview of the Finite Element Method, along with the fundamental theory used to replicate the experiment. The subsequent part provides a more in-depth explanation of the implementation technique applied to generate the results presented in Chapter 3, Chapter 4 and Chapter 5 .

2.4.1 The theory

Numerical techniques for approximating solutions to PDE are essential, especially when exact solutions are only feasible for simple cases. As a result, the Finite Element Method can be employed to study very complex or geometries to calculate approximate solutions to PDEs. The high adaptability of the FEM to different structures and boundary conditions makes it well-suited for intensive use in industrial applications and research. The FEM includes a large family

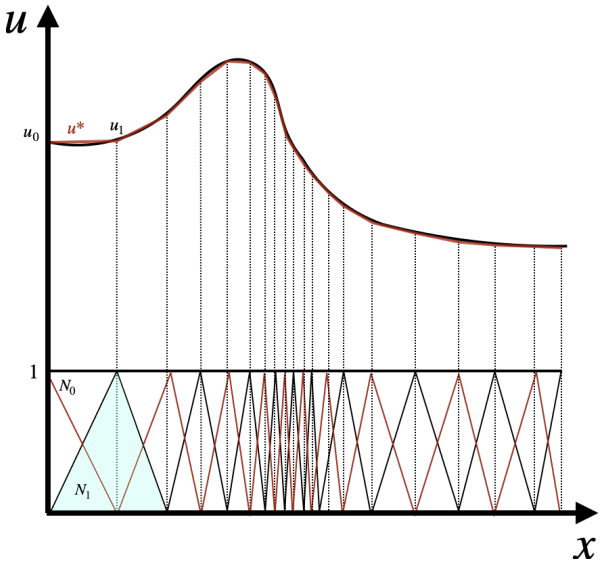

Figure 2.7: Construction of an approximated solution in finite element, revised from comsol manual.

of different techniques that all share a similar pattern. In the following the main characteristics shared by all the different techniques are highlighted, with particular focus on the chosen one.

The first step in the FEM is discretizing a continuous domain into a finite number of elements connected through nodes. This process is known as meshing or discretization. Different element types are used depending on the geometry: line elements for 1D systems, triangular or quadrilateral elements for 2D systems, and cube or tetrahedral elements for 3D systems. Each element is classified as a beam or bar based on whether moments are allowed at the nodes.

In the discretized space, the solution to the problem, specifically the displacement function u, is also discretized as $\boldsymbol{u}^*$:

$$\boldsymbol{u} \approx \boldsymbol{u}^*(x) = \sum_i \tilde{\boldsymbol{u}}_a \boldsymbol{N}_a$$

Here, $\tilde{\boldsymbol{u}}_a$ represents the unknown displacement value at the nodes, and $\boldsymbol{N}_a$ denotes a basis or shape function. $\boldsymbol{N}_a$ is equal to the identity matrix at node a and 0 at all other nodes. Figure 2.7 illustrates an example where the real solution $\boldsymbol{u}$ is approximated by the function $\boldsymbol{u}^*$, with the displacement values $\tilde{\boldsymbol{u}}_a$ accurately calculated, for a one dimensional case. Moreover the importance of generating a good mesh is evident, as the node density should be higher in regions where the solution varies rapidly. Once the solution is calculated at each node, it is approximated in the space between them using an element order such as linear, quadratic, or cubic, determined by the shape function $\boldsymbol{N}_a$.

Let us explore now how the approximated solution $\boldsymbol{u}^*$ can be determined. The equations we aim to solve for the calculation of the displacement $\boldsymbol{u}$ are explained in the previous chapter (see Eq. (1.6) together with Eq. (1.5)). Two main families adopted for this task are the variational and weighted integral solutions. The first relies on the minimization of the system's total energy, such as the elastic energy in our case, and the second on the minimization of residual, more a mathematical and general approach that can be used even when the variational principle is invalid.

Our equations are usually transformed to a linear system of the type:

$$a(\boldsymbol{u}, \boldsymbol{v}) = L(\boldsymbol{v}) \tag{2.5}$$

From the literature, a is known as the bilinear form and L as a linear form, $\boldsymbol{u}$ is the solution, and v is a trial solution introduced in the following. The idea of reducing the complexity of the problem is commune to all the different techniques; all of them aim to simplify it by reducing the problem to a linear one, also reducing the derivative order of the equations, this is known as the weak form.

To derive the weak form, we introduce a test function $\boldsymbol{v}$ in equation 1.6 and consider the integral. By using the divergence theorem, it can be shown that:

$$\begin{cases} a(u, v) = \int_\Omega \boldsymbol{\sigma}(u) : \boldsymbol{\epsilon}(v) d\boldsymbol{r} \sim \int_\Omega \boldsymbol{\sigma}(u^*) : \boldsymbol{\epsilon}(v) d\boldsymbol{r} \\ L(v) = \int_\Omega \boldsymbol{f} \cdot v d\boldsymbol{r} \int_{\partial\Omega} \boldsymbol{T} \cdot v d\boldsymbol{r} \rightarrow 0 \end{cases} \tag{2.6}$$

$L(\boldsymbol{v})$ for our application is considered as zero, given that no body forces $\boldsymbol{f}$ are used, no traction $T = \boldsymbol{\sigma} \cdot \boldsymbol{n}$ is imposed on the external surfaces as a boundary condition, with $\boldsymbol{n}$ the normal vector to the

surface. The system left is $a(u, v) = 0$, where $\boldsymbol{\sigma}(\boldsymbol{u}) : \boldsymbol{\epsilon}(\boldsymbol{v})$ represents the inner product between the stress tensor defined in the space of the solution function, and the strain tensor defined in the space of the trial function. [94].

In modern FEM codes, many of the steps mentioned above are performed partially by the software and the user. Defining the problem correctly and ensuring a good discretization of the domain is crucial. The definition of the stiffness matrix and its solution are handled numerically, and in most cases, there is no need for manual intervention.

Following this high-level approach, post-processing is essential for result validation, and a detailed analysis of this aspect is presented in the following Section. The Finite Element analysis code used is FEniCS [95], an open-source platform that allows high-level coding with Python or C++.

2.4.2 Nano-indentation simulations based on FE calculations

The nano-indention experiment can be reproduced in Finite Elements, assuming a linear elastic material.. The main steps to be followed are depicted in Figure 2.8. As previously underlined the first step

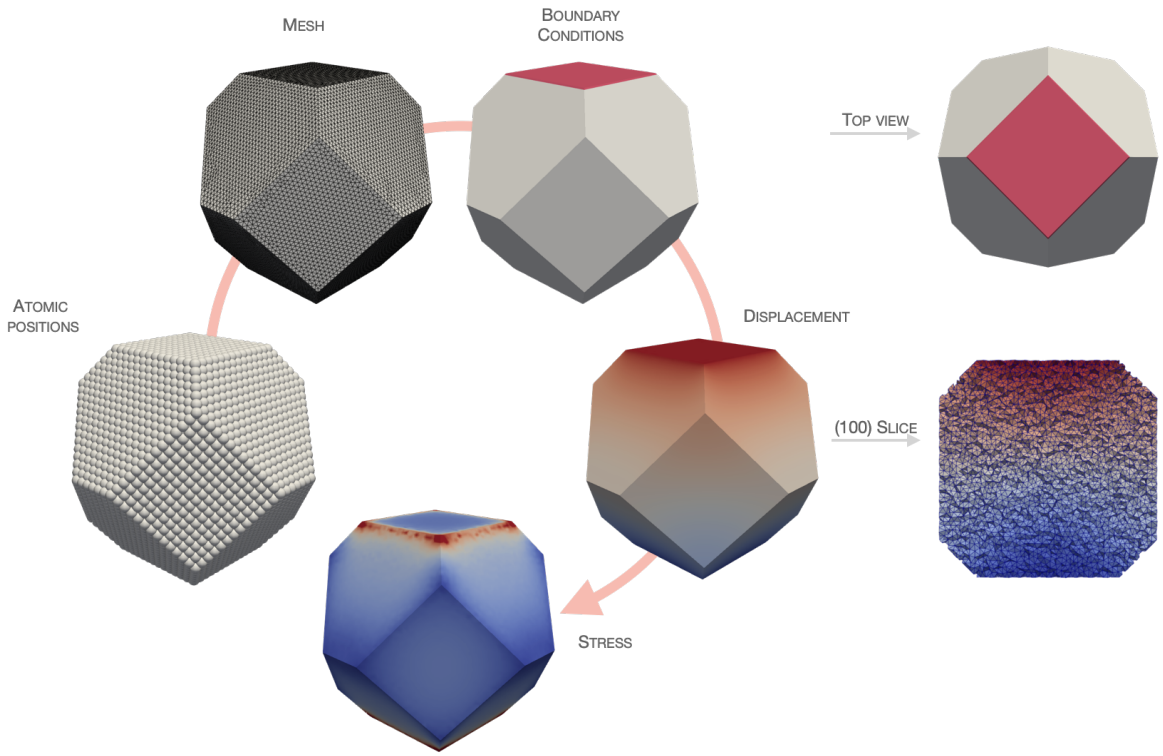

Figure 2.8: Main steps followed to compute elastic properties in nanoparticles. Mesh generation from the atomic positions, choice of proper boundary conditions, and finally displacement and stress calculations.

is the discretisation. For this task a mesh is generated starting from

the atomic positions of the nanoparticle, using the *gmsh* code[96]. To ensure accurate results, it is essential to consider the distribution of mesh elements throughout the computational domain. The mesh should be finer in regions with high displacement gradients (like the nanoparticle top and bottom surface and, in general, edges and corners) and coarser in region where the displacement field is smooth. One should be careful to avoid excessive mesh density in coarser regions; this may lead to unnecessary computational costs without significant improvements in solution accuracy.

When the desired mesh is ready, the boundary conditions can be specified. To emulate, at best, the Molecular Dynamics simulation conditions, a displacement, u_{top}, is imposed normal to the indented top surface (pink surface in Figure 2.8), fixing the NP bottom. An alternative solution (not adopted here) consists in imposing a force acting at the top surface, the traction $\boldsymbol{T}$ in equation 2.6. When the mechanical equilibrium is computed, the solution u^* is known at every mesh nodes. Then, the stress and strain can be calculated following equations 1.5 and 1.6, as depicted in Figure 2.8. Notice that the forth order elastic tensor of equation 1.6, is reconstructed with the elastic constants extracted from SMA potentials to be consistent with MD simulations.

An important average factor useful for the comparison with MD is the extraction of the slope of the stress and strain curve, the Effective Young's modulus ($E_{eff} = \Delta\sigma/\Delta\epsilon$, see Figure 2.4). Here, $\Delta\sigma$ is the stress of the top surface (pink region in Figure 2.8); this can be obtained by integration of the reaction force over the domain and dividing it by the relative area. The strain, on the other hand, is directly calculated knowing the imposed displacement and the size of the nanoparticle $\epsilon = (d - u_{top})/d$.

Different simulations are carried out to ensure a good refinement of the glsfem solution. To this end E_{eff} is computed as a function of the mesh density, as highlighted in Figure 2.9. The mesh is iterativeley refined, the optimal mesh density has been chosen when an error lower than 1% with respect to the previous E_{eff} value is reached. Applying this criterion the convergence is found for density larger than 1Å^3 (number of nodes divided by the NP volume). The nanoparticles used to generate the mesh has an atomic density of $\sim 0.08^3$. So, at mesh density larger than 1Å^3 the nodes have a distance between them smaller than the interatomic distance: it can be argued that there is no sense in using a sub-atomic mesh, that the physical model solved with the method holds only at a larger scale, and so on. Such an argument misses the global view of FEM; what we are interpreting as a 10nm size nanoparticle could also be seen as a 10m nanoparticle, and given that we are working at imposed strain, the result would not change. Solutions computed on the same shape with the same

dimensionless boundary condition (such as the strain) are said to be *self-similar*, and the same result is always recovered. So even if a mesh can seem sub-atomic, it is not; the quality of the mesh has to be judged only by the quality of the solution. This point can be better understood in the following Section, where the elastic response does not depend on size (until an important surface effect takes place).

Other secondary but still crucial factors that can influence the solution are the solver type, the convergence criterion, the type of the element, and the choice of accurate boundary conditions. Solver type significantly impacts the efficiency and accuracy of the solution. Direct solvers are accurate but computationally expensive for large-scale problems, while iterative solvers offer scalability but require a careful selection of preconditioners and convergence criteria. Considering the size of the mesh, an iterative solver is preferred, either the *coniugated gradient* or the *GMRES* solver. Convergence criteria are vital for assessing solution accuracy. Both relative and absolute errors should be considered, and the value of 10^{-5} is considered a reference. Moreover, different element types (linear, quadratic, etc.) can deeply influence the response. The results in Figure 2.9 use first-order elements; slightly better results can be obtained with second-order elements, but there is a considerable increase in computing time as drawn back.

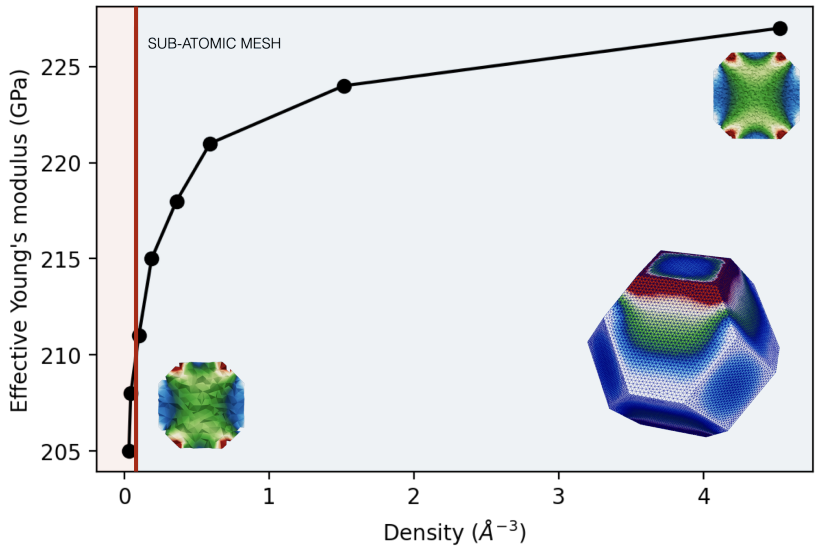

Figure 2.9: Effective Young's modulus as a function of the mesh density, results convergence with sub-atomic meshes

2.5 CALCULATIONS OF ELECTRONIC PROPERTIES

With the ultimate goal of investigating the properties of deformed nanoparticles, we now turn our focus to their electronic properties. In Chapter 1 we introduced the Tight-Binding Hamiltonian. In this section, we will present the techniques we employed to diagonalize the matrix and determine the energies. However, direct diagonalization

can be computationally expensive, particularly for larger systems, as in tit is the case in this study.

Here a different method, with respect to direct diagonalization, which is more effective in our case of analysis, is presented and implemented in the code described in Chapter 6, all details can be found in [97]. Two main steps are involved: tridiagonalization of the Hamiltonian matrix and the calculation of the density of states using the Green's function (as shown in scheme 2.7).

$$H \xrightarrow{\text{Recursion}} \begin{pmatrix} a_0 & b_1 & & & \\ b_1 & a_1 & b_2 & & \\ & b_2 & a_3 & b_3 & \\ & & \cdot & \cdot & \cdot \\ & & & \cdot & \cdot & \cdot \end{pmatrix} \xrightarrow[\text{fraction}]{\text{Continued}} G(E) \rightarrow ldos(E) \quad (2.7)$$

Before explaining the adopted technique used to tridiagonalize H, we need to introduce Green's function of the Hamiltonian:

$$G = \frac{1}{E + i\epsilon - H} \quad (2.8)$$

E represents the system's energy, and ϵ is an infinitesimal quantity. Green's function has a fundamental property that connects it with the density of states as follows:

$$d_n(E) = -\frac{1}{\pi} \lim_{\epsilon \to 0+} Im(G_{nn}) \quad (2.9)$$

Obviously, determining G enables us to calculate the *ldos*. To achieve this, we can use the continued fraction expansion. For instance, by considering the matrix term $G_{00}(E)$ of the Green matrix in equation 2.10-1, we obtain:

$$G_{00}(E) = \langle 0 | \frac{1}{E + i\epsilon - H} | 0 \rangle = \cfrac{1}{E - a_0 - \cfrac{b_1^2}{E - a_1 - \cfrac{b_2^2}{E - a_2 - \ldots}}} \quad (2.10)$$

Note that a_i and b_i are called the coefficients of the continued fraction. Looking again at equation 2.10-1, we observe that the recursion can be stopped at any desired point, as the contributions eventually become negligible.

Without excessive details, this expansion can be reconstructed based on the tridiagonal matrix's properties and the matrix's minors. Tridiagonalization involves transforming the original Hamiltonian (sparse matrix) into a tridiagonal matrix. The power of this process corresponds to simplifying whatever system (nanoparticle, bulk, amorphous...) to a linear chain of atoms, where only nearest-neighbor interactions are considered. In Figure 2.10, we can see the ideal final system. The advantage of this process is that we avoid diagonalizing

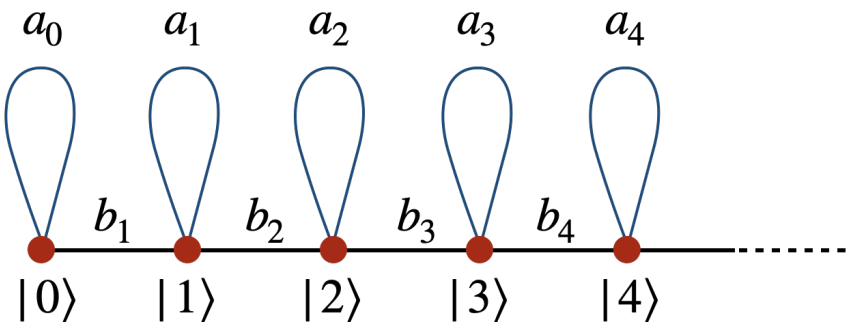

Figure 2.10: Equivalent system produced by the recursion method, all the system can be transformed in a linear chain

a large sparse matrix. Tridiagonal matrices have simple and elegant mathematical properties, and a common method used for tridiagonalization is the Lanczos or Recursion method. An alternative is represented by the moment's method [97]. The final Hamiltonian figures as follows:

$$H = \sum_i |i\rangle\, a_i\, \langle i| + \sum_i b_{i+1}(|i\rangle\, \langle i+1| + |i+1\rangle\, \langle i|) \tag{2.11}$$

a_i and b_i represent the equivalent system's hopping integral and the on-site energy. The tight-binding model emerges as an optimal tool for studying large (few thousand of atoms) and complex systems (nanoparticles, defected structures, amorphous, disordered, ...). Moreover, within the framework of the recursion method, it makes it possible to work in direct space while providing access to local electronical properties. In Chapter 6, this method is employed to analyse the local electronic properties of nanoparticles, taking into account variations in size and shape. We investigate perfect structures without internal stress, those subjected to uniaxial compressive loading, and scenarios with one or more stacking faults in the nanoparticle. However, while this method offers a broad overview, there are gaps in the information it provides. Building on the insights from the first chapter and drawing a clear connection to the realm of catalysis, especially the absorption of hydrogen on the surface, Nørskov's theory aids in addressing and filling these informational gaps.

Tuning elastic properties of pure metallic nanoparticles by shape controlling

3

In this section, we explore the influence of size and shape on the elastic response of nanoparticles. We employ both the Finite Element Method and Molecular Dynamics simulations and compare their respective outcomes. Our analysis focus on the local results, taking into account stress maps, but also considers the effective Young's modulus (E_{eff}), a global parameter. While MD is widely regarded as the method for studying structural properties at the nanoscale, the answer is not as straightforward for Finite Element analysis.

Surprisingly, there is a lack of comprehensive studies regarding the effects of size and shape on the elastic properties of nanoparticles. Most of the previously published works have focused on uniaxial compression along specific orientations for relatively large NPs (above 10 nm), and the variety of NP shapes considered is rarely observed (e.g., cubic, spherical, truncated spherical). However, these studies are insufficient for fully understanding and predicting the elastic deformation properties of metallic NPs. To address this gap, we investigate NPs with different sizes (ranging from 4 to 25 nm) and shapes (truncated cube, cuboctahedral, truncated octahedral, and Wulff structures) that closely resemble those observed experimentally. We employ complementary approaches, i.e., MD and FE, to comprehensively analyze the elastic properties. Differently from *Yang et al.* [57] and *Moseley et al.* [61], a full comparison is proposed in size and shape at the same time (by means of size and shape map), from both a local (stress map and local stress solution) and global (by means of the effective Young's modulus). The methodology outlined in Section 2.4 for nano-indentation is tailored to our case study. Further details are provided, and a dedicated section the study of per-atom stress in atomistic simulations. This thorough approach ensures a deeper insight into the elastic behavior of nanoparticles.

The results exposed in the following chapter are object of a publication in the journal Small: *Tuning Elastic Properties of Metallic Nanoparticles by Shape Controlling: From Atomistic to Continuous Models* https://doi.org/10.1002/smll.202302116.

3.1 Modeling conditions

Molecular Dynamics simulations are performed according to the procedure described in Section 2.3 for gold, copper and platinum nanoparticles. A SMA potential is used, and the fitted parameters of Equation 2.3.3 can be found in Table 3.1. The nanoparticle sizes ranged approximately from 4 nm to 20 nm, with a varying number of atoms between 10^3 and 10^6. Indentation is carried out on both (001) and (111) facets, with shape factors (see Section 2.2) ranging between 0.1 and 1 for the (001) facet, and 0.1 to 0.5 for the (111) facet.

Table 3.1: SMA parameters (see equation 2.3.3) for Au, Cu and Pt. More detail on the potential in [98–100]

	r_0 (Å)	p	q	A (eV)	ξ (eV)
Au	2.885	10.29	4.020	0.206	1.802
Cu	2.565	11.06	2.463	0.094	1.287
Pt	2.814	10.80	3.1976	0.199	2.232

Table 3.2: Comparison with SMA model with experimental or DFT results: lattice parameter a (Å) and Binding energy E_b from [6], Surface energies γ_{001} and γ_{111} (eV/at) from [101], Elastic constants (GPa) $T = 4K$ values, for Au and Cu from [6]. Pt Elastic constants from [102].

	a	E_b	C_{11}	C_{12}	C_{44}	γ_{001}	γ_{111}
SMA (Au)	4.08	-3.81	186	154	44.5	0.30	0.22
Experiment or DFT (Au)	4.08	-3.81	192	163	42.0	0.78	0.68
SMA (Cu)	3.63	-3.39	171	125	74.0	0.48	0.39
Experiment or DFT (Cu)	3.62	-3.50	168	121	75.4	0.73	0.63
SMA (Pt)	3.98	-5.53	267	196	100	0.67	0.51
Experiment or DFT (Pt)	3.92	-5.86	373	241	77.6	0.91	0.64

Finite Element simulations are also performed using the procedure outlined in Section 2.4. As previously mentioned, the elastic constants for stress calculations are extracted from MD simulations, and the values for the three chosen materials can be found in Table 3.2. For the study of the (111) facet, the elastic constant tensor C_{ijkl} is rotated according to:

$$C^{(111)} = RCR^{-1} \rightarrow R = \begin{pmatrix} -2/\sqrt{6} & 0 & 1/\sqrt{3} \\ 1/\sqrt{6} & -1/\sqrt{2} & 1/\sqrt{3} \\ 1/\sqrt{6} & 1/\sqrt{2} & 1/\sqrt{3} \end{pmatrix} \tag{3.1}$$

3.2 Virial vs Cauchy stress

In the following sections, one of the comparisons discussed concerns stress maps and local solutions. While computing them with the Finite Element Method is straightforward, the process with Molecular Dynamics can be quite intricate. Before delving into this analysis, a comparison of the main available techniques for atomistic stress study is provided.

The most commonly used method for mapping stress onto the volume of a nanoparticle is the one used by *Kilymis et al*. [39]. The stress tensor can be calculated as follows:

$$S_{ij,k} = -mv_iv_j + W_{ij} \tag{3.2}$$

Here, i and j are the cartesian coordinates x, y, and z, and k represents the atom. The first term in the equation accounts for the kinetic energy contribution, where m is the mass of the atom and v_i is the velocity in the i-th direction. In our specific case, this contribution can be considered negligible ($T \sim 0$). The second term, W_{ij}, incorporates all

the inter-atomic interactions arising from the potential and is referred to as the Virial contribution. This term can be directly computed using the LAMMPS software. The quantity $S_{ij,k}$ has units of $[Pa] \cdot [m^3]$ and to obtain the stress, it must be divided by the volume of the atom. This volume can be calculated using the Voronoi tessellation which is already integrated in LAMMPS code. It is worth noting that while the volume is well-defined within the nanostructure, it becomes less reliable near the surfaces. Since nucleation often starts at the surfaces, this can limit the interpretation of results obtained from the last layer of atoms.

Alternatively, a second option involves post-processing with OVITO software [103]. This enables the calculation of displacement and strain tensors based on a reference structure, typically an unstrained structure. Once the strain is computed for each atom, the stress tensor can be obtained from Hooke's law. Using this method, surface artifacts are no longer a concern, making it suitable for comparison with Finite Element results. However, it is important to note that this method does not capture intrinsic strain and stress (*residual stress*) of the unloaded nanoparticle important when dealing with surfaces compression [104], and alloys, lattice mismatch can induce very high local stress. In Figure

Hooke's law:

$$\sigma_{ij} = C_{ijkl}\varepsilon_{kl} \tag{3.3}$$

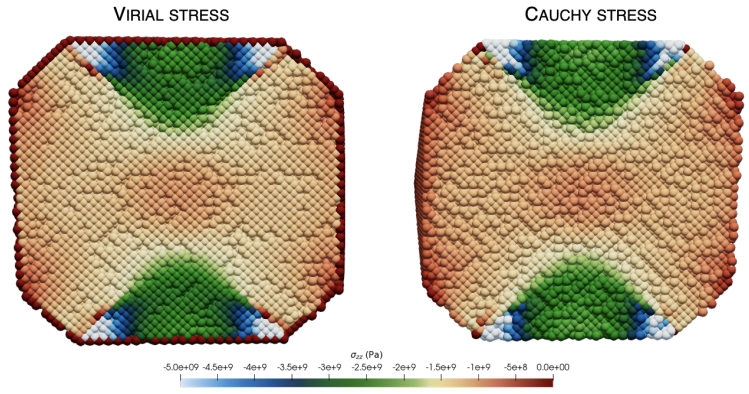

Figure 3.1: Comparison between Cauchy, and the new Virial stress maps (σ_{zz} component) for a gold truncated-octahedron nanoparticle containing around 10^5 atoms. Simulations are performed at T=0.1 K by imposing nanoindentation of 4.8% deformation on (001) facet. Stress map view obtained with Paraview software [105].

3.1, a comparison between two methods, the Virial stress (left) and the Cauchy stress (right), is presented. The nanoparticle chosen for this comparison is a (001) oriented gold truncated octahedron (15 nm size and containing 10^5 atoms). The deformation of the nanoparticle is pushed to its limits close to the nucleation point (here 4.8% deformation), in order to amplify and observe any potential non-linear effects. In this case, we are specifically examining the σ_{zz} component of stress. The Virial stress map shown in the Figure 3.1 is obtained by subtracting the residual stress to the stress calculated by LAMMPS at the nucleation point. As seen in Figure 3.1, both approaches give similar tendencies with especially a conical region located near the plane indenters. Within the nanoparticle, the values of the σ_{zz} component are also very close, this indicates that the impact of potential non-linear effects is negligible. The white-blue-green atoms, which

represent the sites where nucleation is likely to occur, are located in the same region and exhibit similar magnitudes of stress. On the surface of Virial solution, due to an incorrect Voronoi volume calculation the first layer of atoms is compromised: all information on surface compression are lost.

The same comparison can be done more clearly with the histogram presented in Figure 3.2. By removing the initial stress, an almost perfect agreement is achieved between the new Virial stress and the Cauchy stress. With this in mind, the most suitable method is used for

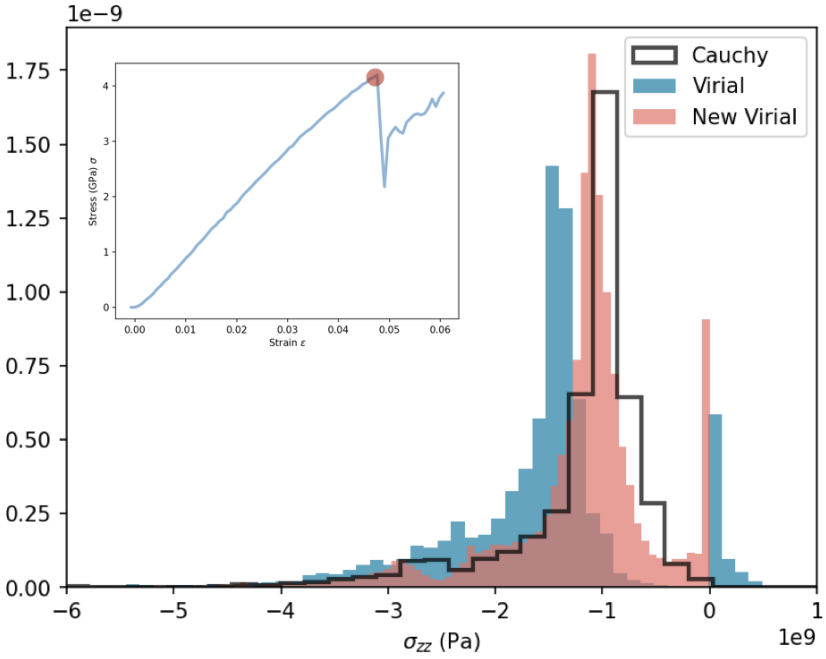

Figure 3.2: Comparison among Cauchy, Virial, and the Virial without the residual stress (termed 'New Virial') is presented in a normalized histogram for the σ_{zz} component for a gold truncated-octahedron nanoparticle containing approximately 10^5 atoms. Simulations were conducted at T=0.1 K, with an applied strain of 4.8% on the (001) facet. At the top left, the stress and strain curve for the analyzed nanoparticle is provided, with the red dot marking the specific configuration being examined.

the given application. When comparing with Finite Element analysis and studying plasticity, the Cauchy stress is preferred. This approach is simpler and analogous to Virial stress. On the other hand, when studying alloys, particularly nano-alloys, the Virial stress becomes crucial. The presence of residual stress due to lattice parameter contraction for substitutional defects is fundamental to understand the mechanical behavior of nano-alloys.

3.3 GOLD NANOPARTICLES UNDER ELASTIC DEFORMATION

In Section 2.4 and 2.3, we discussed the extraction of stress and strain curves from MD and FE experiments, respectively. Based on the results obtained in the previous section, we introduce an ultimate control on the distribution of the stress map. In the subsequent sections, we compare the two methods and analyze the specific effects of shape and size. The analysis initially focuses on local (stress maps) and global (stress-strain curves) elastic properties in Wulff structures and is subsequently generalized to include all the investigated shapes.

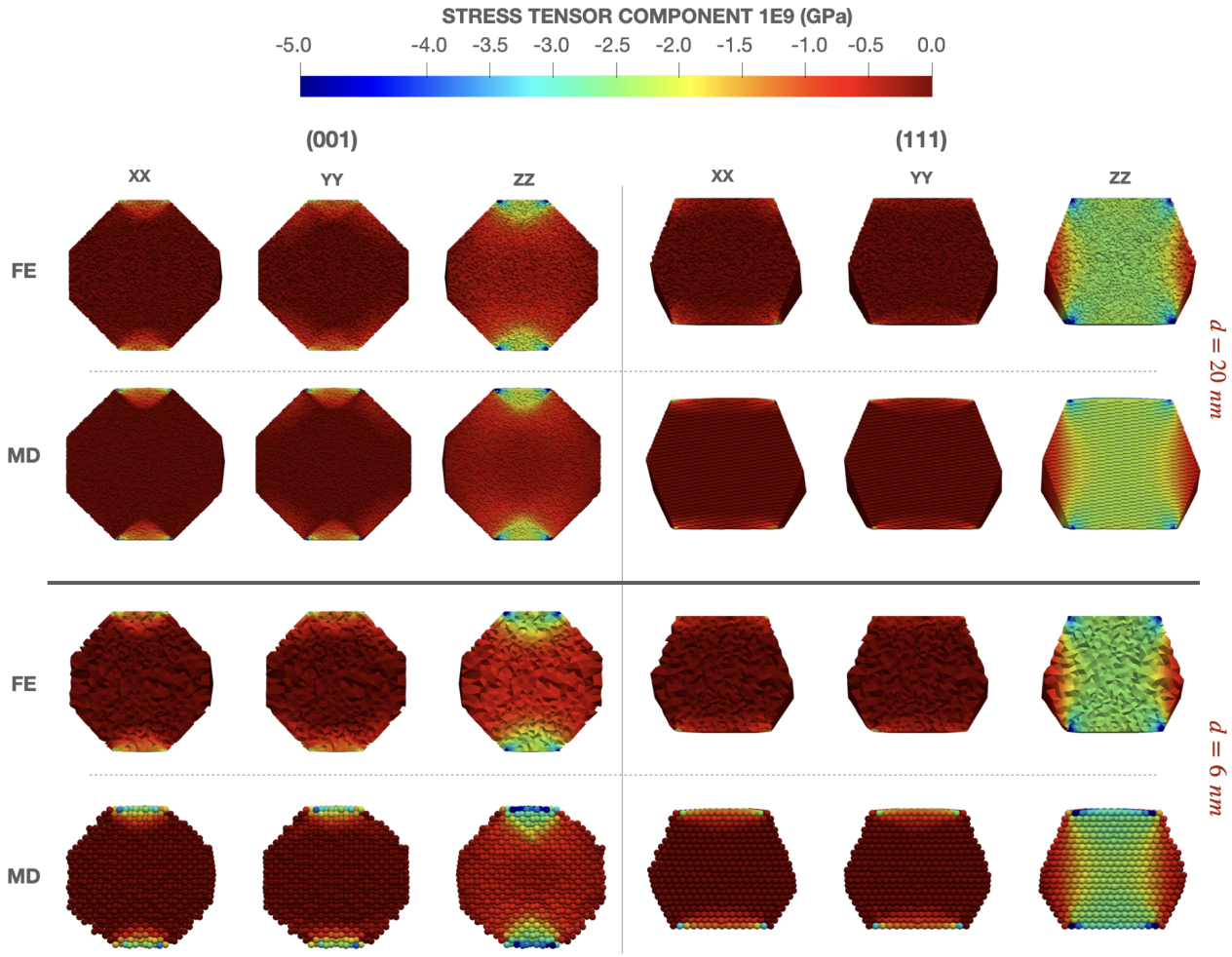

Figure 3.3: Stress maps calculated with MD and FE approaches for Wulff-shaped gold nanoparticles of (top) 20 nm and (bottom) 6 nm diameter NPs and by imposing nanoindentation on (001) and (111) facets.

3.3.1 The stress map

Now that we have discussed the different ways to obtain the stress field in atomistic simulations, we can move forward and compare the results obtained from the two methods by examining the local solutions in detail. The MD stress map was constructed by following the Cauchy stress definition, while the FE method provides the solution of the Partial Differential Equation in the nanoparticle domain straightforwardly.

In Fig. 3.3, the stress distributions obtained from MD and FE calculations are presented for small (6 nm) and large (20 nm) Wulff structures with $G \sim 0.15$ for the (001) surface and $G \sim 0.38$ for the (111) (see Section 2.2 for more details). These correspond to nanoindentations on a (001) facet (left) and on a (111) facet (right) at 2.5% strain, within the linear regime. Regarding the (001) indentation, the stress is concentrated in two conical regions near the plane indenters. As previously discussed in [22, 27], the maximum stress values are observed at

the corners for all components of the stress field. Specifically, for the σ_{ZZ} component, the stress field is negative due to the compression imposed by the applied loading. Additionally, it is worth noting that the presence of free surfaces causes the stress to decrease rapidly from the top or bottom surface to the center of the nanoparticle.

Remarkably, both FE and MD calculations yield very similar results for both NP sizes. The values of the stress tensor components computed using the two approaches are very close, with differences of less than 5%. Similar trends are observed for nanoindentations on the (111) facets, regardless of particle size and shape. The only difference compared to (001) indentation is that the stress distribution is more homogeneous in the z direction. This is due to the larger contact area of the plane indenters, as Wulff structures have wider (111) surfaces compared to (001). To conclude, both finite elements and atomistic simulations are perfectly adapted to capture the elastic properties on a local viewpoint from stress map analysis.

3.3.2 Stress-strain curve

In the previous section we discussed the mechanical properties of NPs from a local point view via the stress maps. Here we want to analyze global elastic properties, by the means of stress–strain curves, comparing MD and FE outcomes.

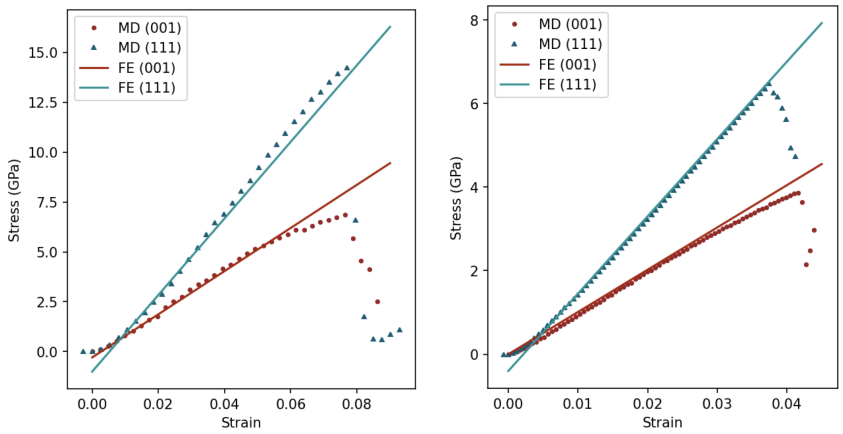

Figure 3.4: Compressive stress as a function of strain of Wulff-shaped NP of different sizes: (a) 4 nm and (b) 18 nm. Comparison between FE and MD calculations with indentation on (001) and (111) facets.

For this purpose and to highlight elastic size effect, the mechanical responses of NPs of different diameters d are considered. Figure 3.4 depicts the stress-strain curves of a small ($d = 6$ nm) and larger ($d = 20$ nm) Wulff NPs nanoindented with plane indenter on the (001) and (111) facets. The same G factor defined in the previous section was considered. In the case of MD simulations, deviation from linearity in the elastic regime is observed for the small NP as seen in Fig. 3.4a. This trend is found for all particles below 5-6 nm in agreement with previous calculations [34, 39, 53] where the influence of surfaces on

the mechanical behavior inside small NPs is emphasized and the non-linear effect of the potential are exploited, given the high deformation $\sim 8\%$. Smaller nanoparticles become stiffer, a non negligible part of atoms are on the surfaces, where they are naturally compressed. For the larger NPs, a linear trend is observed in the elastic regime until plastic deformation, whatever the facet considered (see Fig. 3.4b).

Obviously, finite elements fail to reproduce the deviation from the linear regime observed for small particles (intrinsically, no deviation from linearity can be observed); this is due to different reasons. First, in case of few atoms it is very difficult to precisely define a NP shape in MD calculations. Second, surface/volume ratio increases so surface relaxation [104] (not included in the FE model) plays an important role in the mechanical response. Last, the effect of corner and edges become important. The last two point could be included with some extra work in our FE formulation, but it was not the topic of our study. We made a pragmatic choice: MD simulations nowadays are very fast for NPs smaller than 5 nm. So, the idea is to use MD to model mechanical behavior of NPs smaller than 5 nm, with a simple FE model for larger system where MD simulations become computational demanding. In contrast, the agreement between MD and finite elements for larger particles is quite remarkable proving that a linear elasticity framework can be used to model mechanical properties at the nanoscale

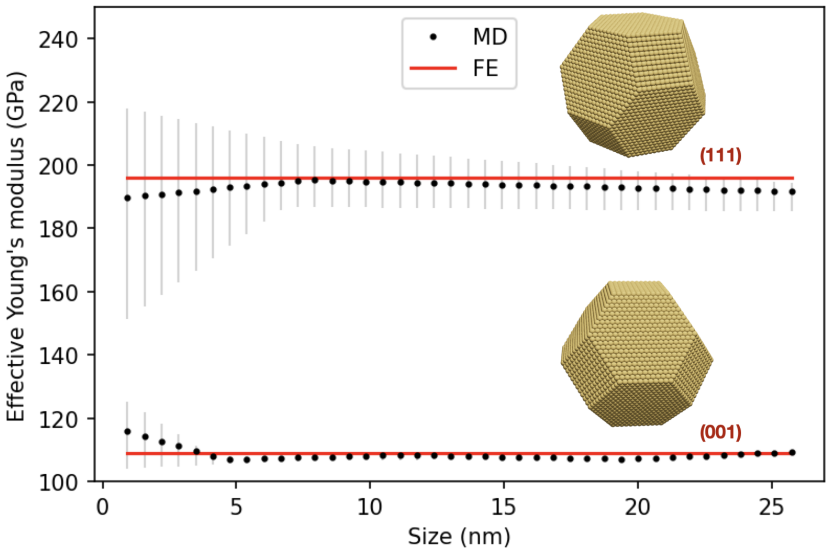

Figure 3.5: Effective Young's modulus as a function of the size for Wulff-shaped gold nanoparticles. Comparison between continuous and atomistic calculations with indentation on (001) and (111) facets

To better analyse the elastic behaviour of NPs, effective Young's modulus (defined in Section 2.3) are extracted from the stress-strain curves for all NP sizes. E_{eff} is a quantity directly by uniaxial loading experiments or simulations (being the slope of the experimental stress-strain curve that can be different from the bulk Young's modulus value) and, for this, is a key parameter for developing reliable applications [106–109].

The results for indentation on both facets are presented in Figure 3.6. Above 5 nm, it can be observed that MD and FE calculations provide very similar results with extremely low errors. This is not so surprising for large particles since finite elements reproduce the elastic domain very well as revealed in Fig. 3.4b. For smaller particles, it is clear that the deviation from linearity already discussed in Fig. 3.4a is not reproduced with FE calculations. Furthermore, the parameter E_{eff} is also difficult to be defined for small NPs. For this reason an error bar is introduced that consider different possible linear fit for the elastic part of a given nanoparticle stress-strain curve. Due to the deviation from linearity using MD calculations, E_{eff} values for small NP have larger error bars than the large ones. Nevertheless, when comparing results from FE and MD calculations even for small NPs, the global slope of the curve is rather correct enabling to get effective Young's modulus values in agreement between both approaches. As the size of the nanoparticles increase the value of the effective Young modulus for both (001) and (111) indentation converges to a plateau [54]. While the $E_{eff}^{(111)}$ is larger than $E_{eff}^{(001)}$, as expected in anisotropic media ($E^{(111)} > E^{(001)}$ for bulk), the value of the plateau depends on the shape of the NP, as it the following sections.

In Figure 3.6, we can observe the dependence of the Young's modulus on the crystallographic direction for bulk gold. As the direction changes from [001] to [111], the Young's modulus, E, increases accordingly. See Appendix 8.3 for more details.

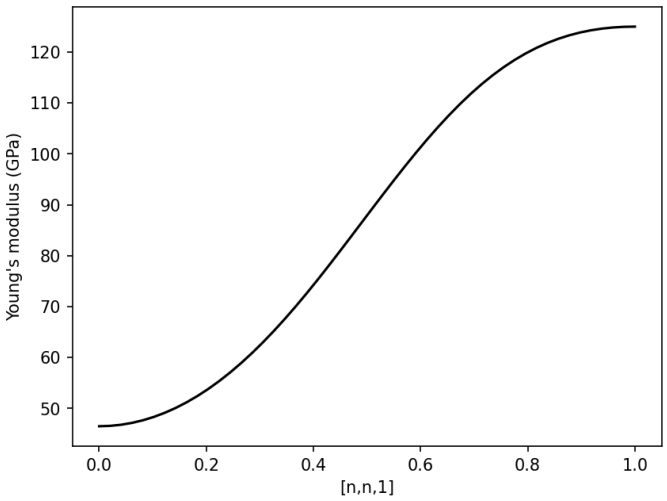

Figure 3.6: Gold bulk Young's modulus as function of the direction, from (001) to (111). Computed using the MD elastic constant that can be found in table 3.2.

Studying nanoindentation of a Wulff Au nanoparticle, we have shown both finite elements and atomistic simulations are perfectly adapted to capture the elastic properties on both a local (stess map) and a global (stress-strain curve) viewpoint. The agreement between the two different approaches is good, notably for NPs with diameter above 5 nm. Consequently, for small NPs, surface sites are prevailing and FE calculations are not able, by definition, to reproduce their influence, hence the discrepancies observed in our study between the two

approaches for small particles. On the other hand, beyond a certain size of NPs (here 5 nm), the role of facet becomes of primary importance give results in very good agreement between finite elements and the atomistic approach.

3.3.3 SHAPE EFFECTS

To highlight shape effect on the elastic properties, the mechanical responses of different Au NPs are considered. In Figure 3.7, the calculated effective Young's modulus for various NP shape as a function of size are presented with indentation on (001) facet.

First, we can notice that the general observation of the previous section for Wulff shape NPs are valid also for truncated-octahedra and truncated cubes: for NPs larger than 5 nm the value of E_{eff} converge to a plateau and no visible size effect is observed. In the case of the truncated-octahedron, there is a stronger variation of the E_{eff} values for small size NPs (< 5 nm) in MD calculations, from ~ 200 to ~ 175 GPa. For larger particles, E_{eff} reaches a constant value around 175 GPa. Again, FE approach is not able to reproduce such a size dependence, suggesting that the role of specific surface sites cannot be neglected in small NPs.

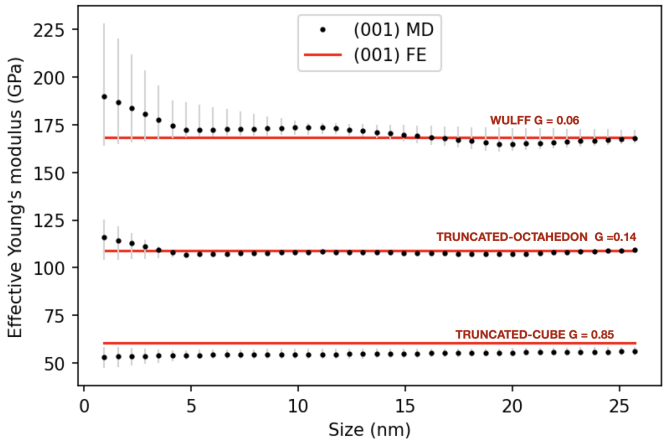

Figure 3.7: Effective Young's modulus as a function of the size for gold nanoparticles with different shapes. Comparison between continuous and atomistic calculations with indentation on (001) facets.

On the other hand, the agreement between FE and MD for larger particles is quite remarkable. More interestingly, a strong shape effect is observed in Fig. 3.7, where the E_{eff} plateau value changes depending on the shape. Indeed, wide differences are obtained ranging from ~ 50 GPa (truncated cube) to ~ 175 GPa (truncated octahedra). To go beyond in our analysis, Figure 3.8 depicts the variation of the effective Young's modulus for different shapes at a given NP size (here 18 nm). Again, a very good agreement is found between FE and MD calculations. A maximum difference of about 4% is revealed and corresponds to the truncated-cube shapes. Such deviation is due to the non linearity of the stress-strain curves in approaching a cubic system (for cubes a very large elastic deformation of about 10% is

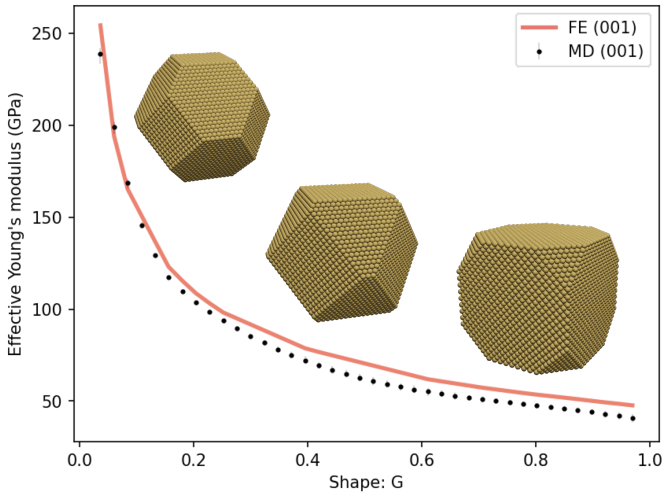

Figure 3.8: Effective Young's modulus as a function of the shape for gold nanoparticles. Results correspond to an indentation on (001) facets for a 20 nm diameter NP.

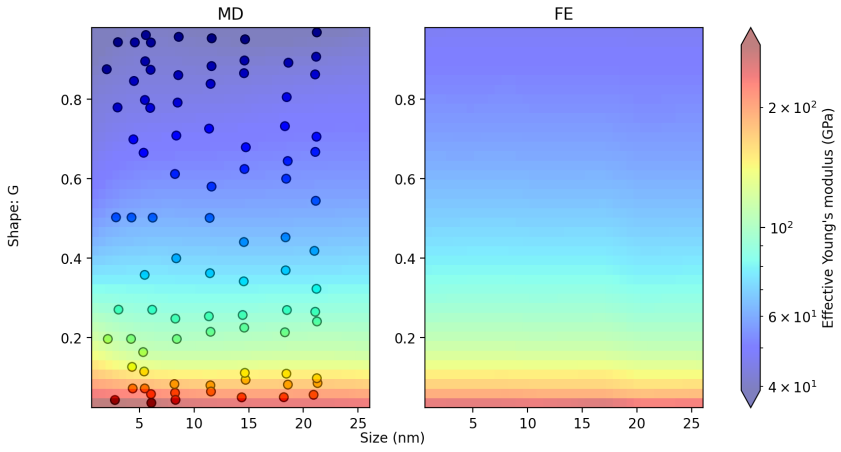

Figure 3.9: Effective Young's modulus as a function of the size and shapes for gold nanoparticles plotted on a bi-dimensional map. Comparison between atomistic (on the left) and continuous (on the right) calculations for an indentation on (001) facets.

observed before the plastic onset, so non-linear behaviour is observed in MD simulations). Convergence is expected for bigger systems, where surface effect and the critical strain are lower.

Very interestingly, a significant variation of the order of 200 GPa can be observed between the two limiting shapes. This considerable effect illustrates that the influence of the NP shapes on the elastic properties is huge for a 18 nm nanoparticle.

To generalize, E_{eff} computed values in function of different shapes (G descriptor) and of NP sizes ranging from 4 to 25 nm is presented in Fig. 3.9 in a bi-dimensional map for MD simulations (left panel) for FE simulation (right panel). On one hand, no size effect is identified (above 5 nm). Indeed, the variation of the E_{eff} with the size of the NP is negligible, never exceeding few GPa for a given NP shape. On the other hand, significant variation of the effective Young's modulus are remarked with NP shape. From truncated-cube to truncated-octahedron structures, a difference of about 150 GPa on the effective Young's modulus is reported. Here again, we can note that the agreement between the atomistic and finite element calculations is remarkable whatever the shape and size of the NP.

It is worth noting that as the G factor approaches 1, the effective Young's modulus (E_{eff}) tends to converge towards the bulk value shown in Figure 3.5. This indicates that when the nanoparticle shape approaches an homogeneous stress distribution, the mechanical response becomes more similar to that of the bulk material. Conversely, when the G factor decreases, the stress distribution cannot homogeneously distribute as in the bulk material. Instead, it becomes more concentrated in the corners and edges of the top surface. This localized stress concentration contributes to the deviation from the bulk behavior and the emergence of shape effects in the nanoparticle's mechanical response. It is important to stress that our analysis show that the shape, not the size, of the gold NPs has a wide impact on its macroscopic measured elastic properties.

3.4 GENERALISATION TO OTHER FACETS AND SYSTEMS

As a next step, it is crucial to investigate if the shape effect in the elastic response can be extended to the (111) facet. This is particularly important since transition metal nanoparticles often expose this facet when produced experimentally.

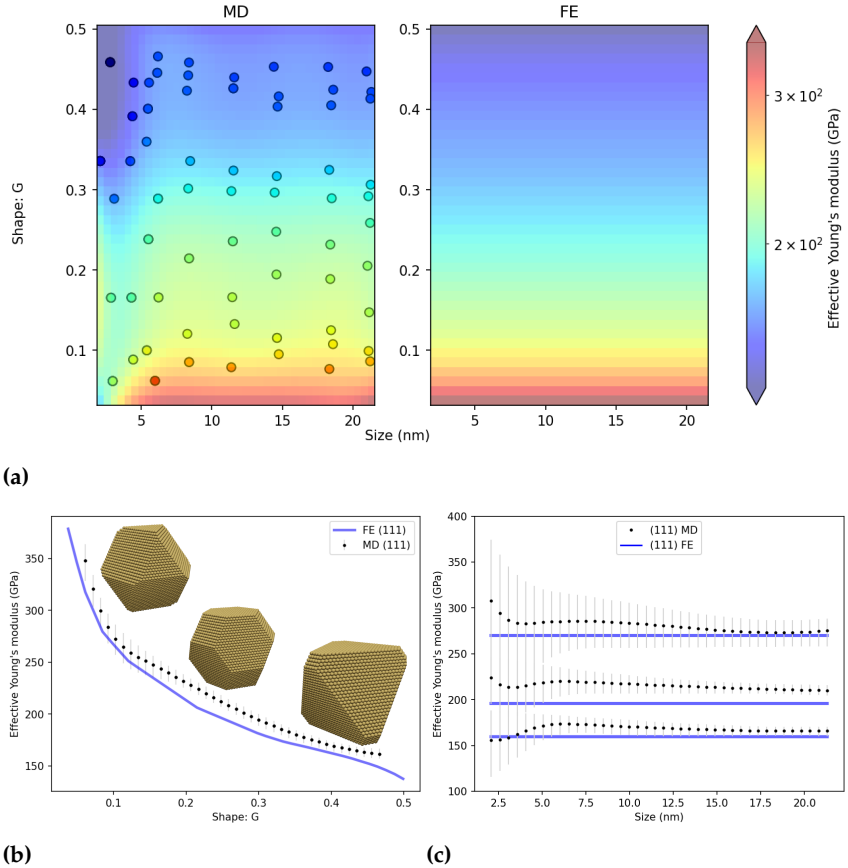

Figure 3.10: Figure (a): Effective Young's modulus as a function of the size and shapes for gold nanoparticles plotted on a bi-dimensional map. Comparison between atomistic (on the left) and continuous (on the right) calculations for an indentation on (111) facets. Figure (b): Effective Young's modulus as a function of the shape for gold nanoparticles. Results from continuous and atomistic calculations correspond to an indentation on (111) facets for a 20 nm diameter NP. Figure (c): Effective Young's modulus as a function of the size for three different shapes.

In Figure 3.10a, we observe the shape-size map for the comparison between Finite Element and Molecular Dynamics simulations. The

agreement is very good, similar to the (001) facet. However, surface effects emerge earlier, and small oscillations due to a poor fit are present in the MD map. The range of shapes considered in the (111) analysis is smaller compared to (001), ranging from 0.1 to 0.5, due to the geometry of nanoparticles.

A more detailed view of the agreement can be seen in Figure 3.10b, where the shape effect on E_{eff} is investigated, and as a function of the size in Figure 3.10c. Again, the agreement is excellent. It is noteworthy that the map in Figure 3.10a follows a similar trend to that in Figure 3.9, with higher values for lower G factors and lower values approaching the bulk counterparts for $G \rightarrow 1$. When G is equal to 1, the stress distribution becomes completely homogeneous, and if the effect of lateral surfaces is negligible, the system becomes analogous to a bulk system. This is true for the (001) nanoparticle and slightly more complex for the (111) nanoparticle.

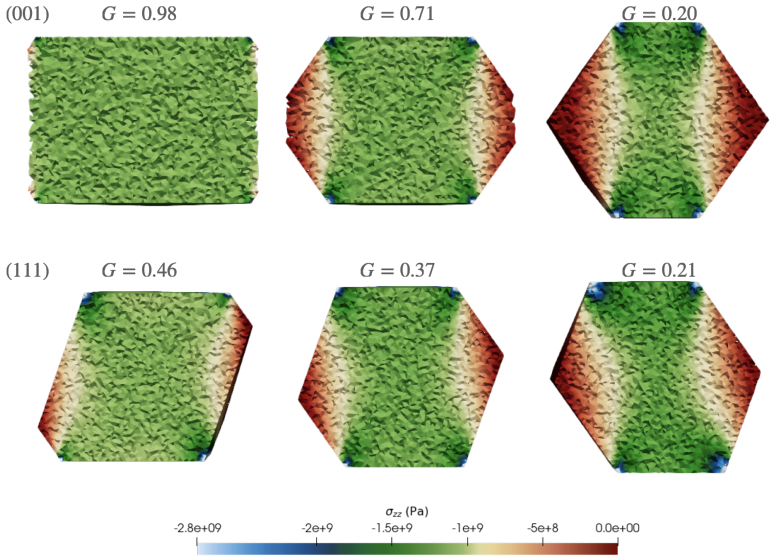

Figure 3.11: Inhomogeneous stress distribution of different shapes with different exposed facets (001) and (111), Slice perpendicular to [010] for the (111) and to [110] for the (001) with a further rotation of 45 degree. $\epsilon = 0.1\%$

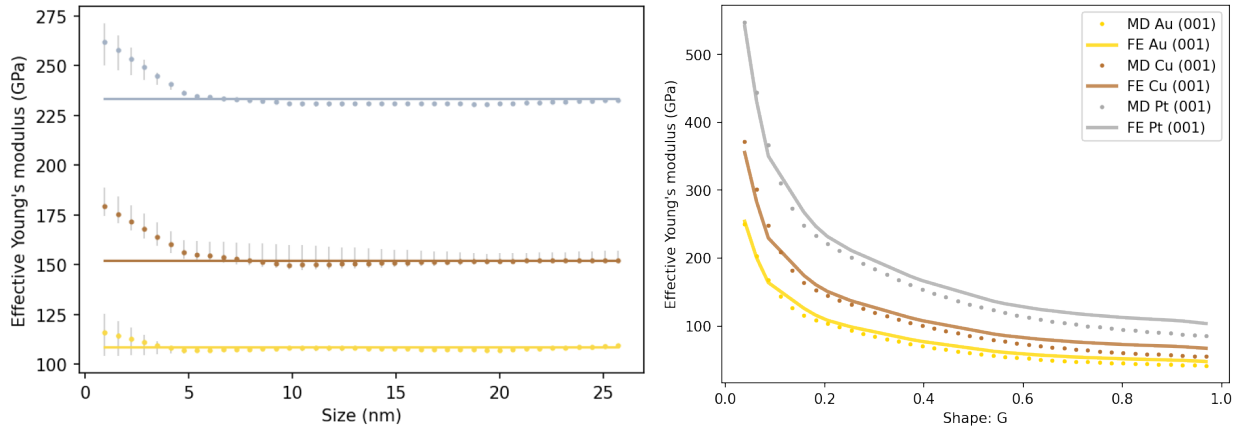

(a) **(b)**

Figure 3.12: Effective Young's modulus as a function of the size (Figure (a)), and shape (Figure (b)) for Au, Cu and Pt Wulff nanoparticles.

Figure 3.11 provides a clearer visualization of this effect. It can be observed that the stress distribution is influenced by the G factor. This factor plays a crucial role in determining the stress distribution and, subsequently, the resulting elastic response, specifically the effective Young's modulus. For the (001) facet, this influence of the G factor on the stress distribution is particularly pronounced, and it directly impacts the final elastic response, leading to variations in E_{eff}. Similarly, for the (111) facet, the same trend can be observed. However, the key distinction is that the shapes of the nanoparticles are not symmetric along the z direction. This asymmetry introduces an additional level of complexity to the stress distribution and the resulting elastic response, as seen in Figure 3.10a. To generalize our conclusions, the analysis of the elastic properties of NPs is extended to other metals, such as Cu and Pt. The calculated effective Young's modulus are presented in Figure 3.12a for different sizes with truncated octahedron shape for the (001) facet. Whatever the material considered, we first see that the finite elements reproduce the atomistic calculations for NP sizes exceeding 5 nm. For smaller diameters, the differences are fairly notable for Cu and Pt ($<$ 40 GPa) but minor for Au NPs ($<$ 15 GPa). Beyond this limit, no size effect is reported with a constant value for E_{eff}. Considering this time the shape dependence, it can be seen that the elastic properties vary strongly with the shape of the particle. As shown in 3.12b, significant variations in the elastic properties are highlighted across all the transition metals. Indeed, E_{eff} varies by hundreds of GPa, moving from smaller values to larger values of G.

3.5 Conclusion

In this chapter, we have presented an extensive study on the elastic deformations of metallic nanoparticles with different shapes and sizes. We applied mechanical loading through nano-indentation on (001) and (111) facets of the nanoparticles. By combining atomistic and continuous calculations, we found that there is no size effect for nanoparticles with a diameter larger than 5 nm. Interestingly, we also observed that the elastic properties of nanoparticles are highly influenced by their shape. We identified the ratio between the top area and the projected area as a suitable descriptor to address this shape dependence.

Moreover we can conclude by distinguishing three main size regimes: small nanoparticles with sizes below 5 nm, intermediate nanoparticles with sizes between 10 and 25 nm, and large nanoparticles with sizes exceeding 25 nm. Small nanoparticles exhibit extremely high internal stress before nucleation occurs, leading to non-linear elastic behavior. MD simulations are particularly useful in this regime as they provide fast and reliable results. For nanoparticles within the normal range of

sizes (below 25 nm) that do not exhibit non-linear behavior, bothFE and MD simulations offer accurate descriptions of the elastic problem. However, FE simulations are generally faster than MD simulations in this size regime. In the case of larger nanoparticles (above 25 nm), MD simulations become increasingly time-consuming. Nanoparticles are characterized by smaller critical strains and stress levels therefore, FE simulations are more suitable for studying the mechanical behavior of larger nanoparticles. Overall, the choice of simulation method depends on the nanoparticle size, the presence of non-linear behavior, and the computational resources available. Both FE and MD simulations provide valuable insights into the elastic deformations of metallic nanoparticles in different size regimes.

These findings are demonstrated by nanoindentation on Au, Cu, and Pt nanoparticles, suggesting that our conclusions can be extended to different transition metal nanoparticles. This study highlights that controlling the shape of nanoparticles can be a viable approach for engineering nano-objects with unique and targeted mechanical properties.

Plastic properties of nanoparticles 4

In the earlier work by *Ferruz et al.* [34], size effect in Wulff nanoparticles is investigated. The authors demonstrate that the exponential dependence between critical stress (σ_c) for the onset of plasticity and the size (d) of a Wullf nanoparticle is universal with $\sigma_c = Ad^{-\alpha}$. The same α parameter is recovered with only a rigid shift depending on the material (transition metals) elastic constants is observed. Following this, *Kilymis et al.* [39] have studied silicon nanoparticles with various shape such as Wulff and cubes, faceted or with blunt edges. Their results reveal a complex relationship between the shape of the nanoparticle and the onset of plasticity. Interestingly, no size effects are found for perfect cubic or spherical nanoparticles, specifically on the (001) surfaces. This led to an intriguing question: might the same principles apply to transition metals? These earlier findings are the outcomes of atomistic simulations. More recently, a model based on experimental results is proposed, focusing on the shape-dependent mechanical response of Pt nanoparticles [33]. This model suggests that the shape of a nanoparticle may also influence the size effect.

It is in this context that our analysis takes place. As suggested in Chapter 3, a broad approach that include all differently faceted nanoparticles is required. We intend to extend the work of *Kilymis et al.* by exploring whether their findings can be generalized to transition metals, for different nanoparticle shapes. Furthermore, we aim to investigate whether the observations made by *Ferruz et al.*, concerning the universal size effect, can be extended to all shapes of nanoparticles. By doing so, we aspire to enrich our understanding of the plasticity onset, i.e. the dislocation nucleation process, in faceted transition metal nanoparticle.

This chapter is organized into two distinct sections. In the first section, we examine the onset of plasticity, mirroring the analysis conducted in Chapter 3. The findings are thoroughly analysed with the aim of complementing the previous studies reported above. In the second part of this chapter, we turn our focus towards the understanding of the underlying physical processes that give rise to the plasticity onset.

4.1 Onset of plasticity

In a nano-indentation experiment, nanoparticles are first elastically deformed, and then, when a certain stress is reached, they undergo plastic deformation. This plastic transition is determined by the nucleation of dislocations. In the case of FCC nanoparticles, $1/6\langle 112\rangle$

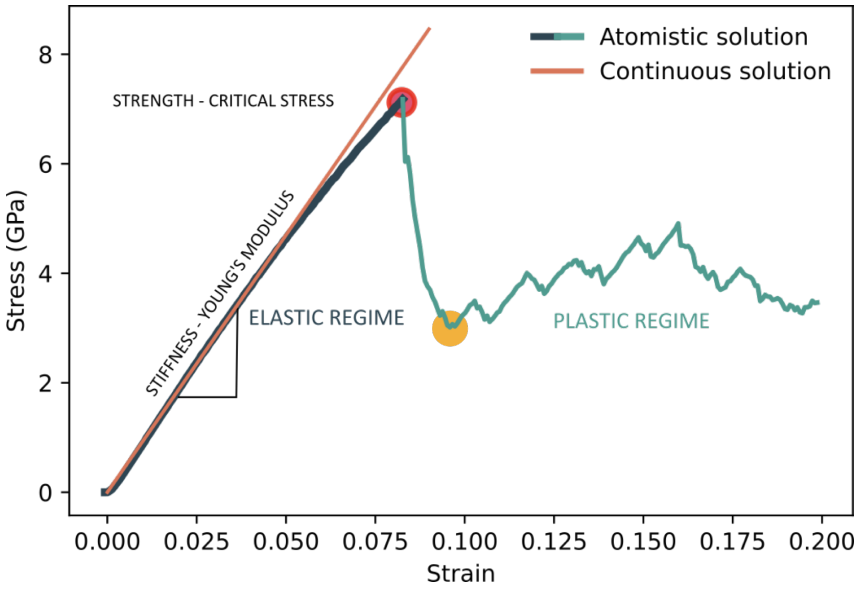

Figure 4.1: Typical stress and strain curve calculated with Molecular Dynamics. The onset of plasticity is highlighted with a red dot whereas the orange dot represents the point where the first dislocation shears the whole structure.

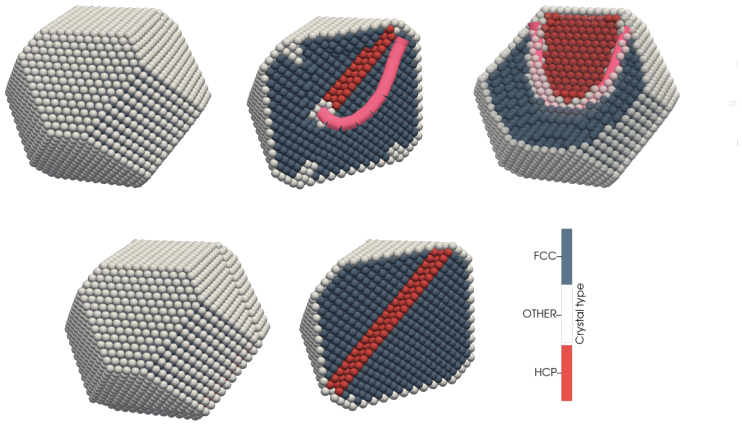

Figure 4.2: Typical dislocation nucleation, top row the dislocation is inside the system, down line the dislocation has slid out of the nanoparticle and a complete stacking fault is formed.

Shockley partial dislocations are nucleated, as discussed in Section 1.2.3 and 1.3. Figure 4.1 shows a typical stress-strain curve obtained using Molecular Dynamics, for a truncated-octahedron structure. The elastic regime is depicted in black. When a critical stress (σ_c) is reached (represented by the red point), dislocation nucleation occurs resulting in a drop in the measured stress value due to the displacement-controlled method. The green region represents the subsequent plastic regime, where dislocations glide out of the nanoparticle or interact with each other. In most of the cases, the orange dot typically represents the point where the first dislocation shears the whole structure, leaving steps at the surface and a complete stacking fault inside the NP. Moreover, the region between the two dots (red and orange) on the stress-strain curve corresponds to the regime of reversible plasticity. Unloading the nanoparticle causes all the dislocations to shrink and to disappear leading to its recrystallisation [110].

Figure 4.2 provides a local view of the nanoparticle at the atomistic scale of different moment of the indentation: the reversible plasticity regime in the three snapshot at the top and the orange dot regime the two at the bottom. In the top figure, the presence of a partial dislocation (pink line) containing a stacking fault is visible. The dislocation defines the boundary between the unslipped and slipped regions. The stacking fault reaching the surface indicates that only first partial dislocation is nucleated. The stacking fault region is interpreted as an Hexagonal Close-Packed (HCP), $ABCABC \rightarrow ABABCA$) crystalline structure, as discussed in Section 1.2.3. In the bottom figure, the dislocation has sheared the system leaving behind the trace of its passage, the stacking fault, and steps at the nanoparticle surface. Such observation is in agreement with previous results[20]. In this chapter, the plastic behaviour of the subsequent nanopartciles is not analysed. Here, we will investigate the nucleation of the first dislocation and the critical stress σ_c at which this phenomenon occurs.

To this end, stress and strain curves similar to those shown in Figure 4.1 were obtained utilizing the methodologies outlined in Section 2.3. This was carried out on nanoparticles varying sizes and shapes, as detailed in Chapter Chapter 3. The ultimate aim was to create a size and shape map for the critical stress values, σ_c.

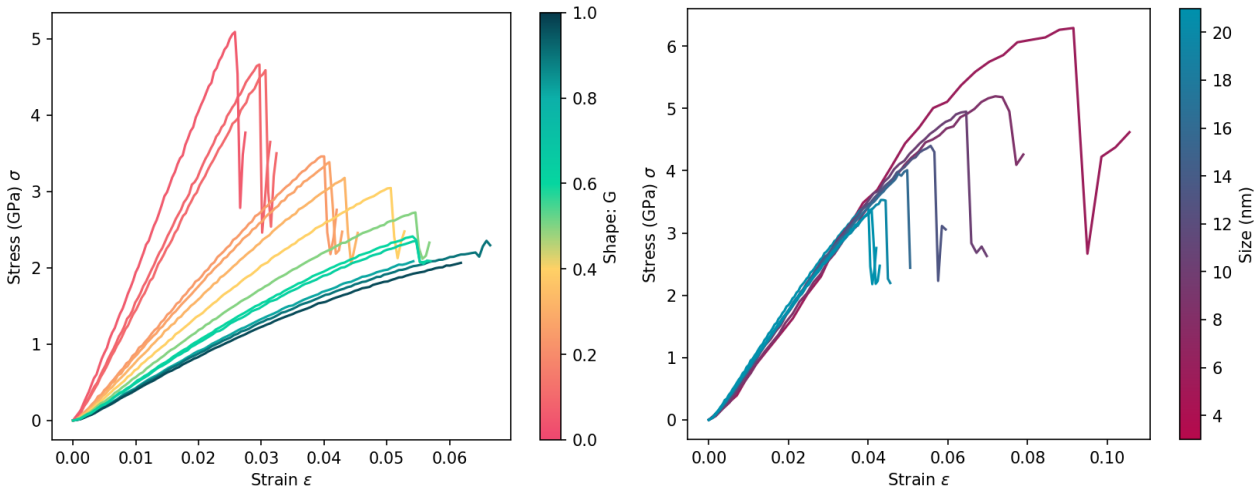

(a) **(b)**

Figure 4.3: Figure (a): shape effect in stress and strain curves for a 20 nm size Au nanoparticles . Figure (b): size effect in stress and strain curves for Au nanoparticles with truncated-octahedral shape ($G \sim 0.25$). In both cases, this corresponds to MD calculations with indentation on (001) facets.

In Figure 4.3, the stress-strain curves calculated for gold nanoparticles are depicted. In Figure 4.3a, the size is fixed while the shape G is represented by different colors. When G increases, the slope of the curve reduces as seen in Chapter 3. This leads to a decrease in the critical stress but it is also accompanied by a considerably larger elastic strain and a small deviation from linearity. In Figure 4.3b, we maintain a constant shape factor ($G = 0.25$), changing the size. This analysis

Since the stress is uniformly distributed in a cubic nanoparticle, the nucleation becomes challenging. This leads to a larger elastic strain and the subsequent non-quadratic behavior of the potential. This outcome is characteristic of cubic structures and is commonly observed in MD simulations.

distinctly shows a size effect: smaller nanoparticles are stronger than their larger counterparts. To go beyond, the maximum value from

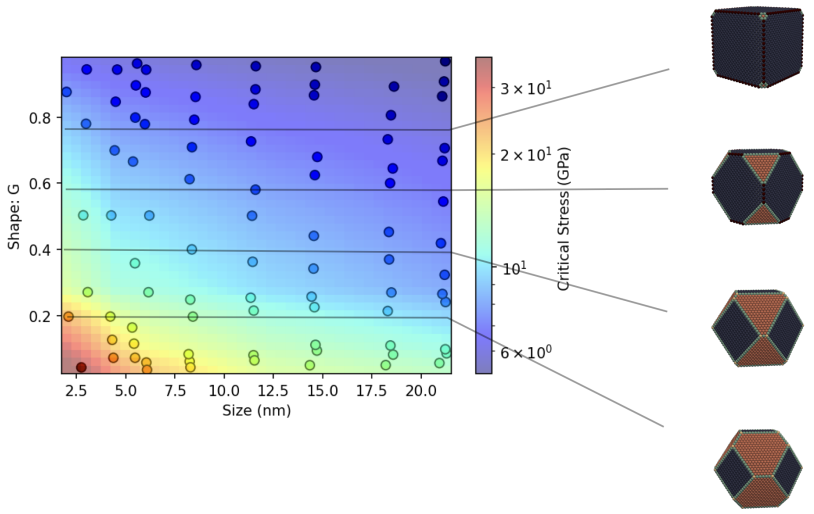

Figure 4.4: Shape and size map for the critical stress σ_c. Result for Gold nanoparticles by imposing nanoindentation on (001) facet.

each curve can be extracted and plotted as a function of size and shape, allowing us to construct a map from this data. Figure 4.4 offers a visual representation of this mapping, focusing on indentation of the (001) facets of gold nanoparticles. Note that the same map was computed also for copper and platinum with similar conclusions. At first glance, the critical stress appears to exhibit a stronger dependence on size for certain structures when compared to their elastic properties. It is noteworthy that a flatter size behaviour is visible for $G \longrightarrow 1$ where the size effect becomes more pronounced as $G \longrightarrow 0$.

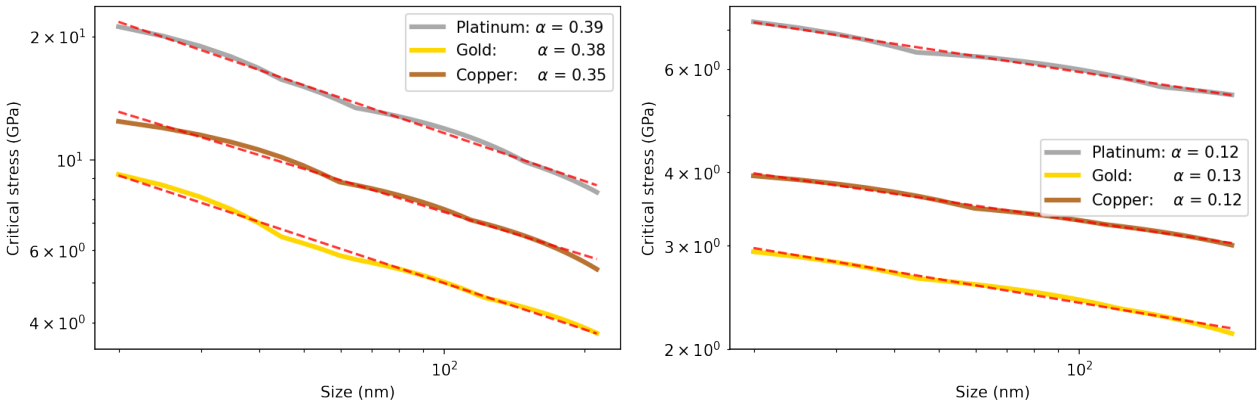

(a) **(b)**

Figure 4.5: Size effect for two different shapes. Figure (a): $G = 0.9$. Figure (b): $G = 0.2$. Results for gold, copper and platinum by imposing nanoindentation on (001) facet.

By creating sections of the shape and size map presented before around $G = 0.2$ and $G = 0.9$ (which correspond to approximately to the Wulff and truncated cube structures) and considering different materials, we can study the variation of the critical stress with the size. As seen in Figure 4.5, we can confirm but also extend the

universal size effect highlighted by *Ferruz et al.* where only Wulff NPs were investigated. Interestingly, the curves obtained for Pt, Cu and Au,exhibit consistent size effects, with a rigid shift similar to what is observed by [34]. The slope remains shape-dependent, implying that identical shapes display the same slope α. This is a significant accomplishment: the Universal size effect can be replicated across diverse FCC shapes of transition metals. Furthermore, as suggested by *Kilmys et al.*, it's plausible that this effect extends to numerous other non-FCC and non-metallic systems. We further explore the role of

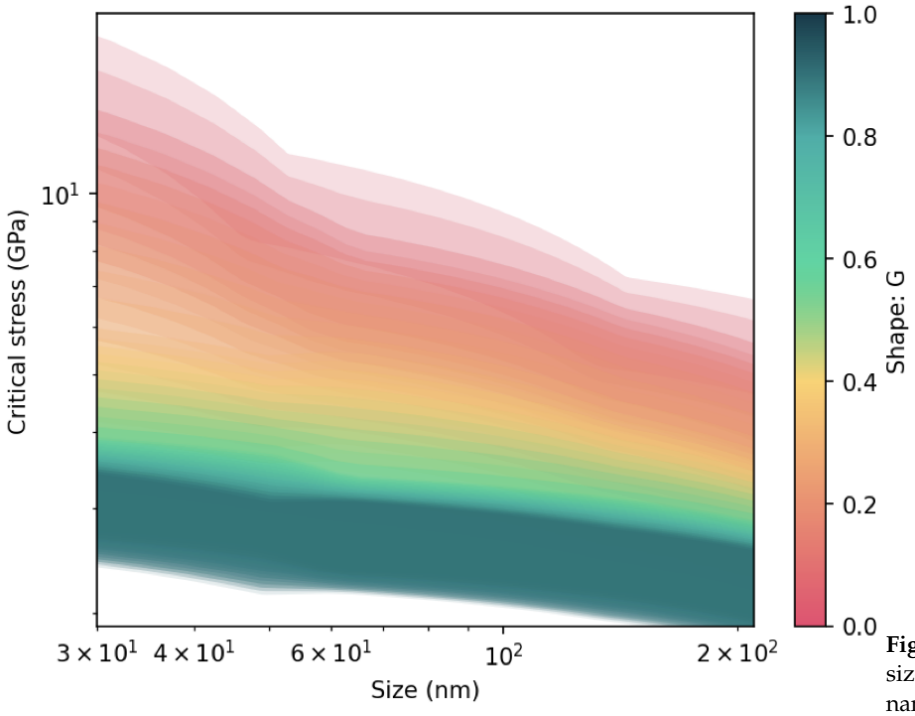

Figure 4.6: Shape effect on the size dependencies of σ_c, for gold nanoparticles on (001) facet.

shape in leading the critical stress in gold nanoparticles through a map presented in Figure 4.6. The size effect weaken as we transition from an octahedron ($G = 0$) to a cube ($G = 1$). This observation is reinforced by analysing the dependence of α (extracted exponent from Figure 4.6) with the shape.

As seen in Figure 4.7, a strong variation is highlighted since α decreases from ~ 0.5 to ~ 0.1 for different G values ranging from 0 to 1. This tendency is observed for the three different materials, namely gold, copper, and platinum. Moreover, around the shape $G = 0.4$ there is a net change in slope suggesting that two different families of nanoparticles can be distinguished. In fact that point represents the transition between truncated-octahedron to truncated-cube structure, the cube-octahedron (see Figure 2.3). The two families differs from the number of corner at the top (001) surface and G tends to 1, resulting in a more homogeneous distribution of the stress field inside the nano-object. This effect was also observed in the analysis of the variation of the effective Young's modulus with respect to the shape, plotted in

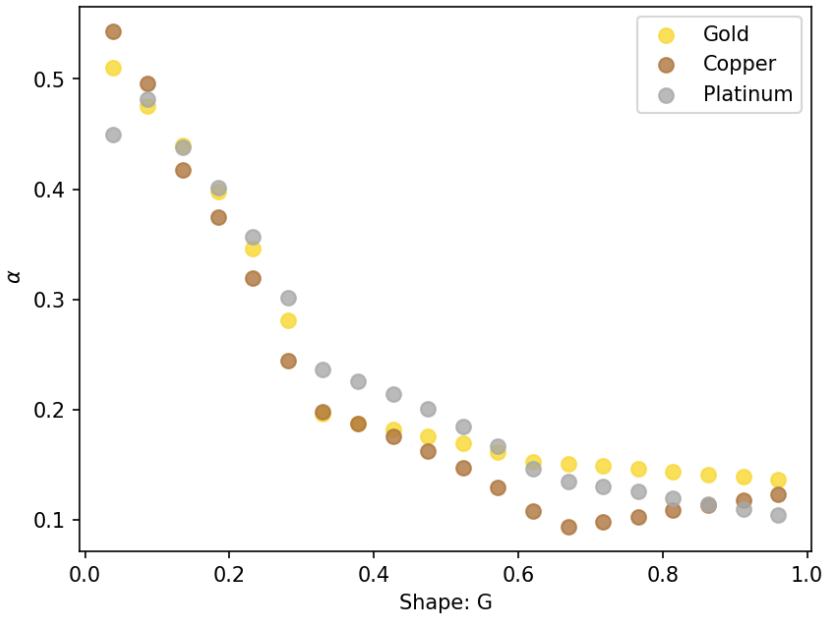

Figure 4.7: Variation of α (extracted from MD simulations) with the shape. Results for gold, copper and platinum nanoparticles with indentation on (001) facets.

Figure 3.7.

This leads us to our first finding: both the shape and size of a nanoparticle are key factors in modulating the onset of plasticity. This suggests that the results obtained by *Kilmys et al.* are not limited to cubic and Wulff silicon nanostructures, but can be extended to all intermediate forms within FCC metals. Furthermore, our findings expand the universal size effect to encompass a wider range of shapes.

The influence of the shape on the plastic onset can be further understood by examining the results for nanoindentation on the (111) facets. By computing the same size and shape map as shown in Figure 4.8a, we can discern a pattern similar to that of the (001) facets. This pattern exhibits higher critical stress for smaller G values and smaller sizes, although the behavior is not identical, possibly due to variations in top surfaces, the number of top corners, and other geometric differences. As discussed in the previous chapter and shown in Figure 3.11, the (111) shapes lack symmetry in the z direction, which could possibly contribute to the less uniform behavior observed in Figure 4.8a. Taking into account an exponential fit of the critical yield stress and extracting the exponent α, we obtain the results depicted in Figure 4.8b. Here, the exponents α for the (111) surface, calculated for different values of G, are compared with those for the (001) surface. Interestingly, both sets of curves seem to exhibit the same shape-dependent behavior. The observed rigid shift can be interpreted by considering the two facets as having distinct geometries. This outcome reinforces our earlier findings: the shape, the size and the loading (depending on the facet being indented) are all key parameters in determining the plastic onset of nano-objects. This represents our final result and a broad generalization applicable to FCC transition metals, and in principle to

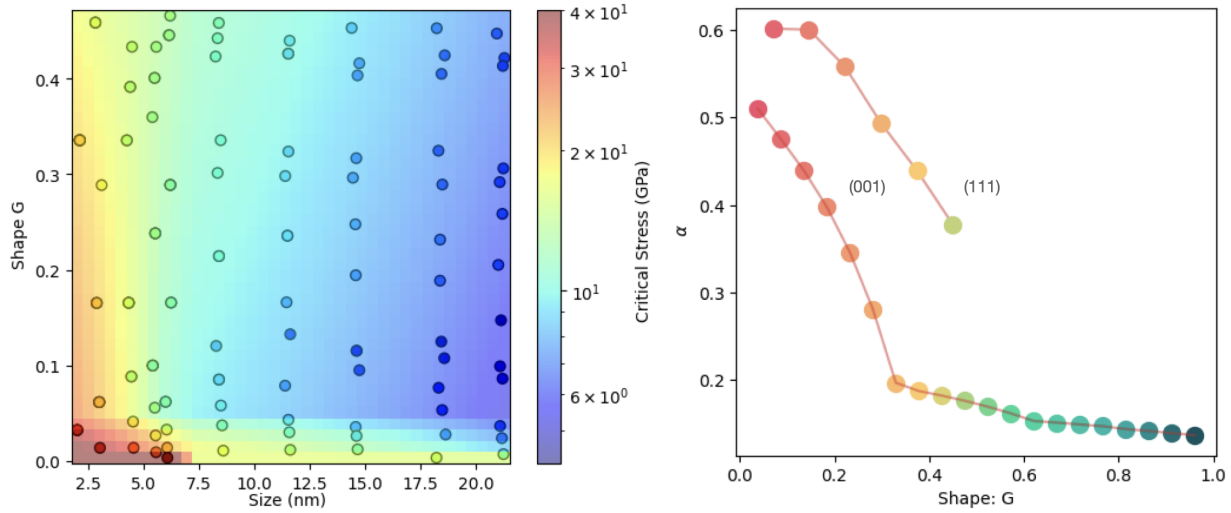

(a) (b)

Figure 4.8: Figure (a): Shape and size map for the critical stress σ_c. Result for Gold nanoparticles by imposing nanoindentation on (111) facet. Figure (b): Variation of α (extracted from MD simulations) with the shape. Comparison Results for gold nanoparticles with indentation on (001) and (111) facets.

other nanostructures.

4.2 BEYOND THE RESULTS: DISLOCATION NUCLEATION

Nucleation is an intricate phenomenon, often discussed statistically in terms of activation volume to identify the most probable dislocation nucleation sites [24, 25]. Moreover, a different approach can be to predict nucleation sites by means strain or stress distribution inside the nanoparticle. This approach aims to identify a critical local stress/strain value that is reached before nucleation [111–114]. In Chapter 3, we observed that the elastic response of the nanoparticles is largely governed by their shape. Moreover, the resulting responses can differ significantly due to the distribution of stress within the nanoparticles. In cubic objects, stress is distributed homogeneously, leading to a bulk-like mechanical response. On the other hand, as we approach $G \rightarrow 0$, the response alters, and the stress distribution is heterogeneous. Based on these previous observations, we opted in the following to define a nucleation criterion based strain or stress distribution using von Mises stress and the resolved shear stress.

It is important to note that these two stresses are considered in different contexts. Resolved shear stress, i.e. the projection of the stress tensor on the glide plane and on the slip direction of a given dislocation, is used to compute the effective stress acting on a dislocation, while von Mises stress is more general, such as determining when a ductile material will begin to yield under complex, three-dimensional loading. These two scalar quantities, despite their simple form, can provide significant insights of the phenomenon of nucleation.

4.2.1 VON MISES CRITERION

The von Mises stress (Equation 1.11), derived from the Cauchy stress tensor, is computed from a FE model since the resulting stress map is identical to that obtained with the Virial stress approach depicted in Chapter 3. As inputs for the FE simulations, elastic constants and critical strain are extracted from MD calculations. A linear interpolation of the MD stress and strain curve was done to reduce non-linear effect, the critical strain is extracted when the linear fit reaches the critical stress.

Based on the critical strain value, the indentation is simulated in the FE framework. Figure 4.9 illustrates the different outcomes in the case of 21 nm gold nanoparticle for two distinct shapes, i.e. the truncated octahedron and truncated cube. As seen in the histogram plot (Figure 4.9a), the truncated cube structure presents a highly localized von Mises stress distribution (a high peak $\sim$ 2.5 GPa), while the Wulff structure exhibits a more dispersed distribution (centered $\sim$ 1.6 GPa for a width of $\sim$ 3 GPa). Again, this demonstrate that NP shape has a strong influence on the internal stress distribution. To

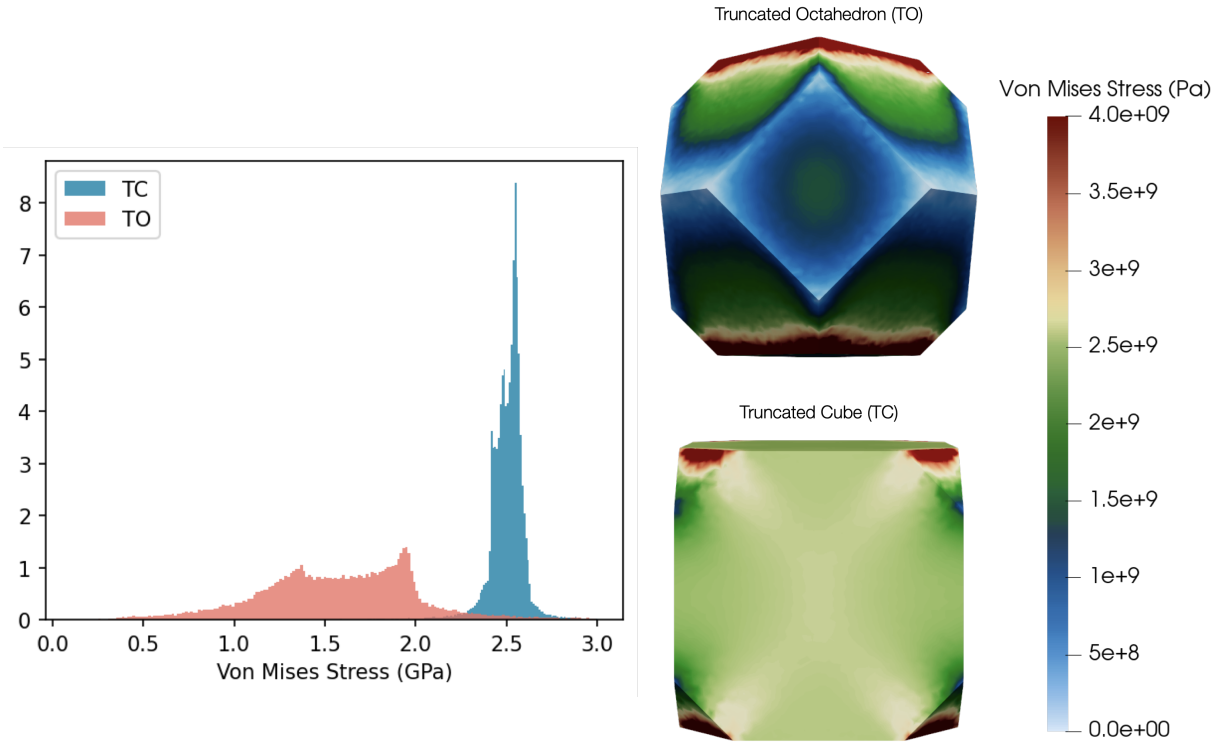

Figure 4.9: FE von Mises analysis for a 21 nm gold nanoparticle with nanoindentation on (001) facet. Results for applied strain $\epsilon = \epsilon_c$ (extracted from MD simulation). TC and TO stand for Truncated Cube and Truncated Octahedron respectively. (a) Histogram form and (b) map form of the surface of the NP.

get a direct insight into the stress distribution at the surface, von Mises maps are presented in Figure 4.9b for both shapes. Thus, it is interesting to emphasize that for the Wulff structure, the stress is strongly localized around the top end the bottom corners leaving the center virtually unstressed. Conversely, in the truncated cube structure, a less important localisation around the top and the bottom corner is observed and the stress is homogeneously distributed around a mean value in the NP volume.

An other intriguing observation is that the tails of the two distributions appear to converge for the maximum von Mises stress to values around 3 GPa, as shown in Figure 4.9a. A visual inspection makes it possible to realize that it corresponds to the corners (top and bottom). Very interestingly, such regions are the place where stress concentration and dislocation nucleation is observed. To link these two information and analyse the shape effect, we can integrate around one of the top corner the values of von Mises stress for different shapes. In this context, the average stress is defined by the following equation:

$$\langle \sigma_v \rangle = \frac{1}{V_{tot}} \int_V \sigma_v(V) dV \tag{4.1}$$

Here, σ_v is the von Mises stress and V represents the volume of

integration. In our case, a sphere is centered at the corner and the intersection between the sphere and the nanoparticle is designated as the total integrated volume V_{tot}. A typical example is presented in Figure 4.10a where we can observe the computed stress map as well as the volume extracted from the sphere where the calculation of $\langle \sigma_v \rangle$ is done. In Figure 4.10b the computed values of $\langle \sigma_v \rangle$ at different sphere radius and shapes are presented.

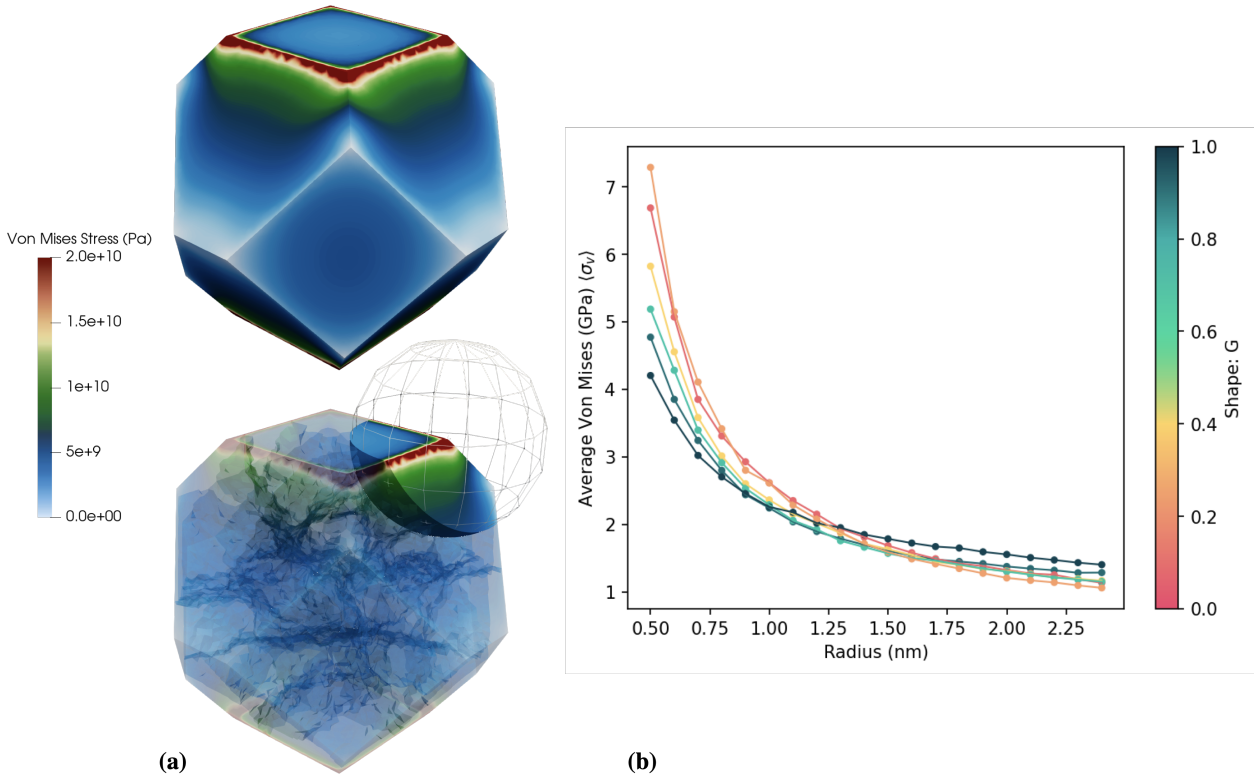

Figure 4.10: Figure (a): von Mises stress map external (top left) calculated at critical strain for a 21 nm gold nanoparticle. At the bottom left, representation of the volume inside the sphere where the stress is averaged to obtain $\langle \sigma_v \rangle$. Figure (b): $\langle \sigma_v \rangle$ for different shapes as a function of the sphere radius.

We note that the mean values demonstrate significant variability for lower R values across different shapes. It is clear that when $G \rightarrow 0$, stress concentrates predominantly at corners and edges leading to large $\langle \sigma_v \rangle \sim 7$ GPa. Unlike the case of $G \rightarrow 1$ where $\langle \sigma_v \rangle$ decreases significantly (~ 4 GPa) corresponding to situation where the stress is more uniform. Yet, as the radius expands, all $\langle \sigma_v \rangle$ begin to converge to reach a converged value ~ 1 GPa from a sphere radius larger than $\sim$ 2 nm the same value. This suggests that nucleation initiates at similar values irrespective of shape. This tendency persists even when we replicate the process for different materials as depicted in Figure 4.11 where the $\langle \sigma_v \rangle$ obtained for a sphere radius equal to 2.5 nm is presented as a function of G for Au, Cu and Pt. No shape effect is noted and this is particularly true for Au and Cu. Only a marked shift is observed between the different elements.

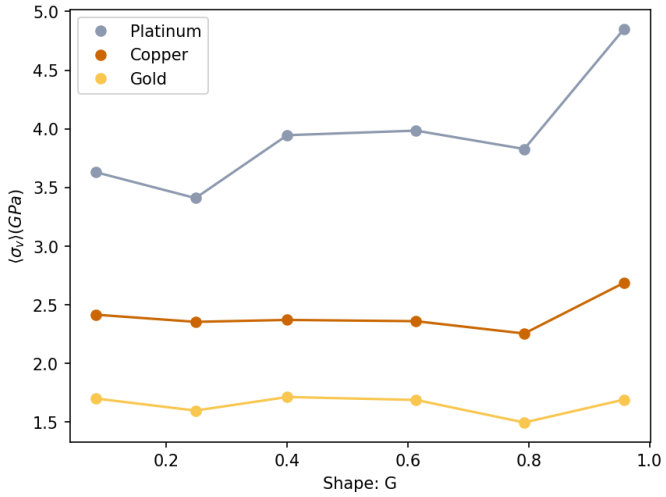

Figure 4.11: Converged value of $\langle\sigma_v\rangle$ for different shapes and different materials. Result for 21nm nanoparticle, for a radius equal to 2.5nm.

By calculating an average of the values exhibited in Figure 4.10 and showing this value as a function of the sphere radius, we can normalize each curve using the corresponding C_{44}, producing the results in Figure 4.12. Initially dispersed values for small sphere radii eventually converge to the same value for the three different materials. The error bar represents the variation $\langle\sigma_v\rangle$ across all shapes from Figure 4.11. It appears that given a specific shape, there exists a universal $\langle\sigma_v\rangle$ condition for nucleation, at least for the transition metals. The normalisation by C_{44} follows what previously done by *Frenkel*, *Cottrel* and applied on nanoparticles by *Ferruz et al.*[34] (see Chapter 1 for more details).

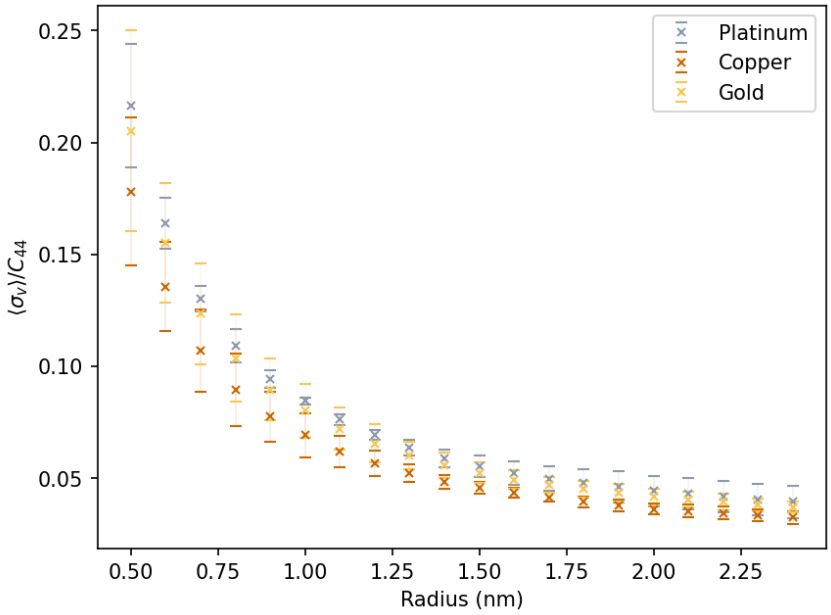

Figure 4.12: Normalised $\langle\sigma_v\rangle$ for different material, error determined by the different shapes.

Our findings lend important insights into how shape impacts plastic behavior in materials. By maintaining a constant size, we can understand why the critical strain, ϵ_c, increase together with the shape factor, G. In the case of $G \to 1$, the stress distribution is homogenous, which

requires higher strain to achieve a specific average von Mises stress, $\langle\sigma_v\rangle$. As for the critical stress, it is important to note that $\sigma_c = E_{eff}\epsilon_c$. The effective Young's modulus, E_{eff}, scales significantly when $G \to 0$, while ϵ_c is reduced. Moreover, our improved understanding of nucleation reveals that even the simple von Mises stress can capture key information about its physics. Nucleation occurs when a certain stress level is reached within a specific volume for all the different shapes, and this value, when normalized by the elastic constant C_{44}, appears to be universal. This observation offers a simplified yet effective method to study the complex phenomenon of nucleation in transition metals, that can be used to model dislocations nucleation in mesoscale models.

4.2.2 The resolved shear stress analysis

In Section 1.3, we mention that *Mordehai et al.* refined Cottrell's model to develop a nucleation criterion based on a non-uniform stress distribution of the form $\sigma_{rss} \sim (R/r)^{-\alpha}$. Here, R is the nanoparticle's height, r is the distance from the singularity, and α is a parameter determined by fitting. This analysis shows the relationship between critical stress and size, indicating a power law of the form $\sigma_c \sim R^{-\alpha}$, where the exponent governing the stress distribution also controls over the size effect. By repeating these calculations for various shapes, we extend the study of size effects to a wider range of structure.

σ_{rss} is calculated using Equation 1.10, taking into account the (111) slip plane and 1/6[112] Burger's direction. Given the lack of clarity on the methodology for extracting σ_{rss} in [27], we present two primary methods for calculating the spatial dependence of σ_{rss} which is a tricky point. The first one involves selecting a plane and line centred at the maximum value of σ_{rss} and extracting the spatial dependence. The second method computes the average stress within a spherical volume centred at the maximum, using the sphere radius as the spatial dependence (as seen in the previous Section already) leading to the following equation:

$$\langle\sigma_{rss}\rangle = \frac{1}{V_{tot}}\int_V \sigma_{rss}(V)dV \tag{4.2}$$

This approach appears more reliable and is considered in the following. The first one oversimplifies the complexity of the stress distribution within a volume and slight variations in the maximum position could lead to significantly different distributions. Conversely, the second formulation averages the behaviour within the volume and it is then less susceptible to local variations.

The Finite Element maps are computed by imposing a critical strain ϵ_c extracted from molecular dynamics, as in the previous Section.

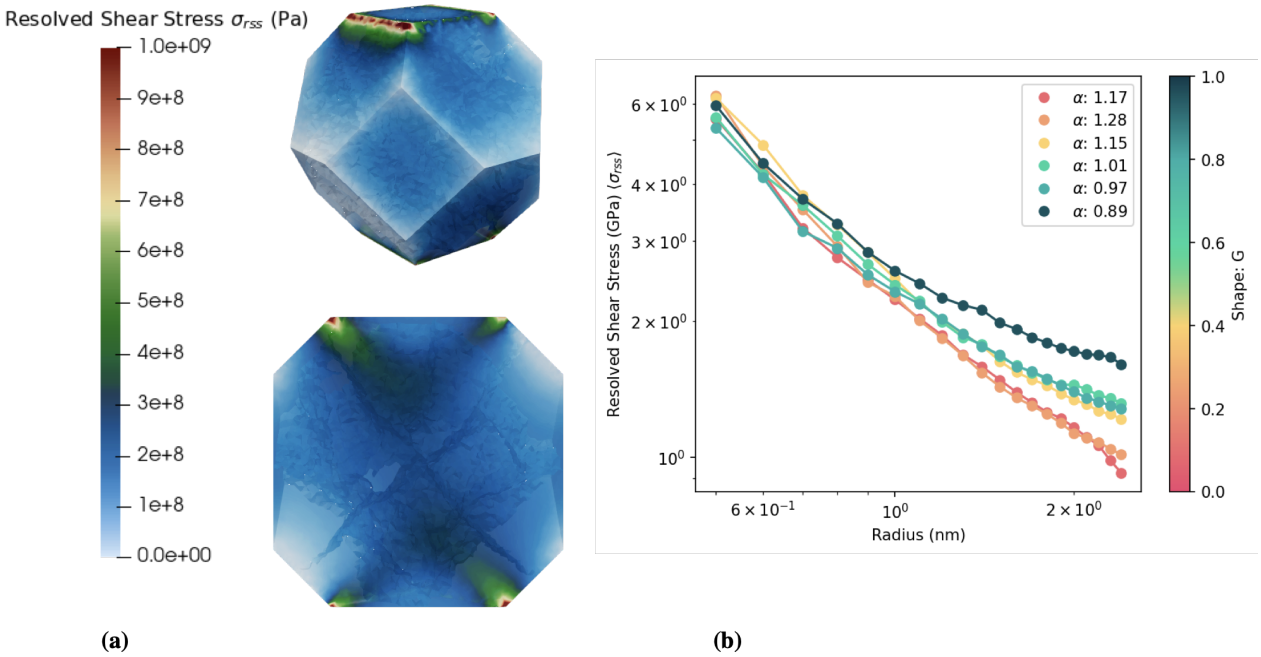

(a) **(b)**

Figure 4.13: Resolved Shear Stress analysis. Figure (a): stress map and local solution, top external view, bottom slice view. Figure (b): $\langle \sigma_{rss} \rangle$ for different shapes of platinum as a function of the sphere radius. The logarithmic scale is used to put in evidence the power law.

Again, a 21 nm Au nanoparticle is selected. In Figure 4.13a we can observe the computed map of the resolved shear stress (σ_{rss}). As expected the stress concentrate at the top left vertex more than in the right one, differently from a von Mises map it is asymmetric. This is due to the projection of stress tensor on specif direction and in a specific plane. Once the stress map is computed the integration for different sphere radius can be repeated, as in the previous Section. The results of this integration is shown in Figure 4.13b on logarithmic scale to evidence the power law. $\langle \sigma_{rss} \rangle$ appears to poorly fit the power law, but with an exponent being shape-dependent, but deviating from the expected values, for example with $G = 0.26$ the expected is ~ 0.4 and we get around 1.28. When $G \rightarrow 1$ the stress distribution tends to be homogeneous and the slope of $\langle \sigma_{rss} \rangle$ has a flatter trend compared to truncated - octahedron structure, where very high stress resides in corner and edges and rapidly goes to zero in the core of the nanoparticle. What seems to drive the size effect is finally a purely massive consideration with almost no effect due to surfaces. The shapes determines the distribution that drives the plastic onset.

Analogous to the method employed in the previous section, we apply the same procedure to the resolved shear stress by calculating an average $\langle \sigma_{rss} \rangle$ obtained for different G values and analyzed its variation as a function of the sphere radius. This has been done for gold, copper and platinum. The results of this analysis are depicted in Figure 4.14 together with the previous concerning the $\langle \sigma_{vm} \rangle$. Again all the curves are normalized using the corresponding C_{44}. These

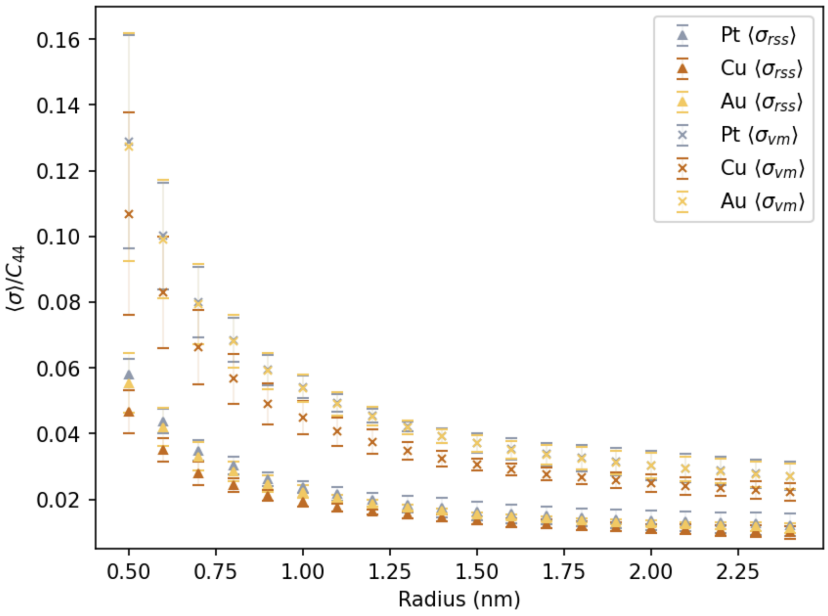

Figure 4.14: Resolved Shear Stress analysis. Normalised $\langle\sigma_{rss}\rangle$ and $\langle\sigma_{vm}\rangle$ for different material, error determined by the different shapes.

findings align with those observed earlier, the convergence of the resolved shear stress seems faster and with lowers errors, reinforcing the observation that a universal value is reached across different shapes and materials prior to nucleation.

4.3 Conclusion

In this chapter, we have determined the significant influence that both shape and size exert on the plastic properties of nanoparticles. Our investigations extend the previously established results of *Kilmys et al.* concerning cubic and Wulff Silicon nano-structures to a more general context, including different transition metals and different shapes (defined by the variation of the geometrical parameter G from 1 to 0). Moreover, our work broadens the universal size effect theory proposed by *Ferruz et al.*, indicating that the shape determines the strength of the size effect, while the material accounts for the rigid shift. In essence, the parameter G is not only representative of a nanoparticle's shape but also serves as an indicator of the nanoparticle's elastic response to a load. It dictates how stress disperses within the nanoparticle, linking this information to the onset of plasticity.

The von Mises stress analysis reveals the reason behind the high deformability of nanocubes in comparison to Wulff structures. This is predominantly due to the presence of a critical local stress that needs to be attained before nucleation can occur. Moreover, our exploration of the Resolved Shear Stress shows the principal driving force behind nucleation: an exponential stress distribution within the nanoparticle, with the exponent diminishing as G tends to 1. Both stress measurements highlight that nucleation can be understood in

a rather straightforward manner; nucleation occurs when a certain normalized stress value is reached within a sufficiently large volume around nanoparticle vertex. While this study exclusively focused on nanoparticles of fixed sizes, it would be interesting to expand this research to encompass size variations, providing a more comprehensive understanding of the complex phenomena associated with nucleation.

Consequently, our findings reaffirm the fundamental role of shape, together with size, in determining the behaviour of nanoparticles under deformation. Its impact seems to be stronger than the crystalline structure, material type, and the indented facet. Our study, therefore, set the way for a new method of analysing nanoparticle data, emphasizing that size effects can no longer be explored without meticulous consideration of the NP shape.

Mechanic properties of bimetallic nanoparticles

5

The investigation of the mechanical properties of nanoalloys is a relatively recent development, emerging mainly after the beginning of this Phd project. As we discussed in Chapter 1, solid solutions have been employed to enhance the mechanical properties of materials at the macro scale. However, the situation appears to become more complicated at the nanoscale.

In the case of NPs, recent studies have revealed that many type of solid solution, (including NiCo and NiFe), exhibit a softer behavior compared to their bulk counterparts. This phenomenon is primarily attributed to the instability of stacking fault energy at the surface, where the formation of clusters intensifies local stress, thus triggering early nucleation (see Figure 1.10). Intriguingly, solid solutions also seem to demonstrate a higher level of toughness, exhibiting strain hardening behavior not observed in pure nano-metals [43, 45, 46]. Moreover, in certain cases, such as NiFe, a transition from ordered, $L1_2$ structure, to disordered systems results in order hardening [46, 115].

In light of these emerging trends, we decided to explore the mechanical properties of Copper-Gold system. Understanding the stability and structural properties of Cu_xAu_{1-x} alloy is a significant area of research because its extensively use in catalytic applications, such as the selective hydrogenation of butadiene or CO oxidation [116, 117]. Additionally, being a different FCC system with respect from NiCo solid solution, mentioned above, this analysis could help to clarify our understanding of existing findings. In this chapter we first begin to characterise Cu_xAu_{1-x} bulk properties, by phase diagram analysis and the extraction of elastic constants. After this, the focus shifts to nanoparticles where the elastic and platic properties are closely inspected with Molecular Dynamics and the Finite Element Method. The primary goal of these investigations is not only to deepen our understanding of the CuAu system, but also to enhance our overall understanding of how plasticity begins in such complex systems, thus enriching our collective knowledge in this field. In this study, we also introduce a general method of analysis that is not only applicable to the Copper-Gold system but it can be readily extended to investigate other systems, particularly those with FCC structures

5.1 Bulk - Copper-Gold alloys

The phase diagram of a material or alloy provides crucial information about its potential phase and crystalline structure under different conditions. Although these diagrams can include changes in both temperature and pressure, in this study, we focus specifically on variations triggered by temperature and concentration. Both gold and copper, on their own, are typically found in the FCC structure, and the same is observable in the copper-gold system, for all the different concentrations.

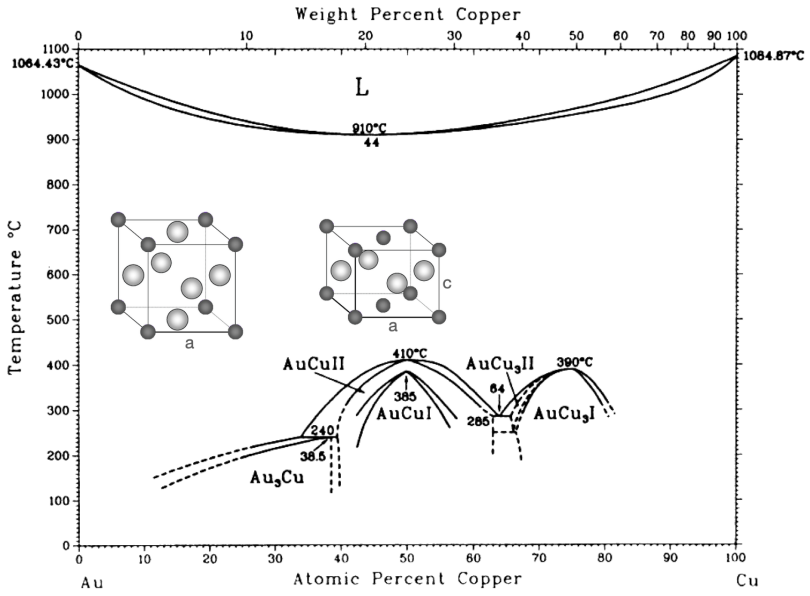

Figure 5.1: Phase diagram of the copper gold system, at different temperature and different concentration (extracted from [118]). The ordered structure $L1_2$ and $L1_0$ are shown, together with the lattice parameters a, c in two different directions, in this case x, y and z.

As shown in Figure 5.1, which represents the phase diagram of the copper-gold (CuAu) alloy, the structural transitions are influenced by temperature and composition. Above 900 K, the alloy is in the liquid state. For intermediate temperatures, the system adopts the form of a solid solution (called phase A_1). Solid solutions are a unique form of alloys wherein two or more types of atoms are uniformly distributed throughout the material. In these solutions, the solute atoms, which can be thought of as the 'guest' atoms, are interspersed within the host lattice. They may either replace the host atoms at regular lattice sites, substitutional solid solutions, or occupy the spaces between the lattice sites. In our analysis we will deal only with substitutional solid solutions.

As the temperature is lowered further, ordering takes place, leading to the formation of different phases. Of special interest are the $L1_0$ phase for the CuAu alloy and the $L1_2$ structure for the Cu_3Au and $CuAu_3$ alloys. The $L1_0$ phase denotes an ordered alloy structure, typically evident at lower temperatures, where copper and gold atoms inhabit alternating layers in the CuAu alloy along a specific direction (refer to Figure 5.1, alternating layers in the z direction). This unique

arrangement often leads to asymmetries in the lattice constants, where c, the parameter along the z direction, is distinct from a, the in-plane lattice parameter.

In contrast, the $L1_2$ structures, applicable to Cu_3Au and $CuAu_3$ alloys, represent a situation where either copper or gold atoms reside at the vertices of the cubic FCC structure, with the rest of the sites occupied by the other metal. This configuration leads to pure and 50% mixed layers, along the direction indicated as a in Figure 5.1.

5.1.1 Validation of the SMA potential for bulk properties

The evaluation of mechanical properties in nanoparticles is carried out using Molecular Dynamics, with support from the Finite Element method. Prior to the analysis, it is essential to verify the suitability of the selected CuAu potential. For this analysis, we have chosen a SMA potential. The parameters for Au-Au and Cu-Cu interactions remain the same as those defined in Table 3.1. These parameters are displayed in Table 5.1 including now the Au-Cu bond parameters.

	r_0 (Å)	p	q	A (eV)	ξ (eV)
Au-Au	2.885	10.29	4.020	0.206	1.802
Cu-Cu	2.565	11.06	2.463	0.094	1.287
Au-Cu	2.725	10.68	3.242	0.132	1.515

Table 5.1: SMA parameters (see equation 2.3.3) for Au-Au, Cu-Cu and Au-Cu interactions. More detail on the potential in [98]

In order to test the potential, different quantities are computed for different concentration and different phases: lattice parameters, elastic constants and enthalpy of formation, ΔH_f. All the values can be found in Table 5.2. The formation enthalpy, is defined as the enthalpy change that occurs when one mole of a substance in its standard state is formed from its pure elements under similar conditions. For the copper-gold alloy represented as Cu_xAu_{1-x}, the formation enthalpy is expressed as:

$$\Delta H_f = E_{tot}(Cu_xAu_{1-x}) - xE_{tot}(Cu) - (1-x)E_{tot}(Au)) \tag{5.1}$$

where $E_{tot}(Cu_xAu_{1-x})$ is the total energy of the mixed Cu +Au system containing xCu atoms and $(1-x)$Au atoms in a given structure, $E_{tot}(Cu)$ is the energy per atom of the FCC Cu and $E_{tot}(Au)$ is the energy per atom of the FCC Au. If there are various potential mixing patterns for a certain concentration and temperature, this parameter can indicate which pattern is more stable or even if the alloy is likely to exist, $\Delta H < 0$ condition. The higher the formation enthalpy, the greater the likelihood of a specific pattern or structure. As seen in Table 5.2, all the three phases ($L1_0$, $L1_2$ and A_1) are stabilised, for the CuAu alloy, the ordered structure is more stable compared to the A_1, not astonishing considering that all the formation energies

Table 5.2: SMA calculations for different mixing patterns and different concentrations. Lattice parameters in two different directions (a and c) and the enthalpy of formation. Comparison with literature (*lit.*) values.

-	a (Å)	c (Å)	ΔH (eV)
$CuAu\text{-}A_1$	3.87	3.87	- 0.078
lit.	-	-	-
$CuAu\text{-}L1_0$	3.92	3.83	-0.276
lit.	3.966	3.673 [119]	-0.091[120]
$Cu_3Au\text{-}L1_2$	3.74	3.74	- 0.226
lit.	3.74	3.74[6]	-0.074 [120]
$CuAu_3\text{-}L1_2$	3.93	3.93	-0.158
lit.	3.98	3.93[6]	-0.059 [120]

Table 5.3: Elastic constants and Young's modulus E values calculated with the SMA potential for different mixing patterns and different concentrations. All quantities are in (GPa). The E values for the $L1_0$ can be imprecise, they are computed considered a simple average as $C'_{11} = (C_{11} + C_{22} + C_{33})/3$ and similarly for the C'_{44} and C'_{12}. Comparison with literature (*lit.*) values.

-	C_{11}	C_{12}	C_{44}	E_{001}	E_{111}
Au	186	154	44.5	46.5	125
$CuAu_3\text{-}L1_2$	193	149	53.7	63.2	145
lit.	189	145	47 [121]	63.1	128
$CuAu\text{-}A_1$	175	143	54.8	46.4	147
lit.	-	-	-	-	-
$CuAu\text{-}L1_0$	200/174	138/164	68.2/47.1	70.3	152
lit.	198/148	144/127	84/100 [119]	-	-
$Cu_3Au\text{-}L1_2$	187	134	68.1	75.1	178
lit.	189	132	74 [121]	80.4	191
Cu	171	125	74.0	65.4	189

are computed at 0K. Regarding the lattice parameters, as previously noted the $L1_0$ structure displays distinct lattice constants for the x, y, and z directions, with x and y being invariant. As illustrated in Figure 5.1, the lattice parameter a varies from c, giving a ratio of $c/a = 0.97$. Contrarily, for the $L1_2$ structure, the lattice parameter remains uniform across all directions, represented as $c = a$.

The table 5.3 presents the values of the calculated elastic constants and the directional modulus of elasticity. These are computed using the methodology outlined in the supplementary material 8.3. Understanding these values is crucial for studying the elastic response in nanoparticles. For the elastic constants, we observe a good match with the literature values for the $L1_2$ system, though a larger deviation is noticed for the $L1_0$ system. This discrepancy can be attributed to the unique structural properties of the $L1_0$ phase, which induces an asymmetric elastic tensor[1] where $C_{11} = C_{22} \neq C_{33}$, $C_{12} \neq C_{13} = C_{23}$, and $C_{44} = C_{55} \neq C_{66}$. Solid solutions have been more deeply tested at many different concentrations. In this case, we consider ten different simulation boxes (each containing approximately 10,000 atoms) for each concentration, with a completely random atom distribution. We perform bulk simulations with periodic boundary conditions aiming to extract elastic constants and lattice parameters. The resulting values are averaged across all the generated boxes. In table 5.2, we can find

1: Computed elastic tensor for the $L1_0$ structure, in the Voigt notations shows as:

$$\begin{bmatrix} 200 & 138 & 144 & 0 & 0 & 0 \\ 138 & 200 & 144 & 0 & 0 & 0 \\ 144 & 144 & 174 & 0 & 0 & 0 \\ 0 & 0 & 0 & 68.2 & 0 & 0 \\ 0 & 0 & 0 & 0 & 68.2 & 0 \\ 0 & 0 & 0 & 0 & 0 & 47.1 \end{bmatrix}$$

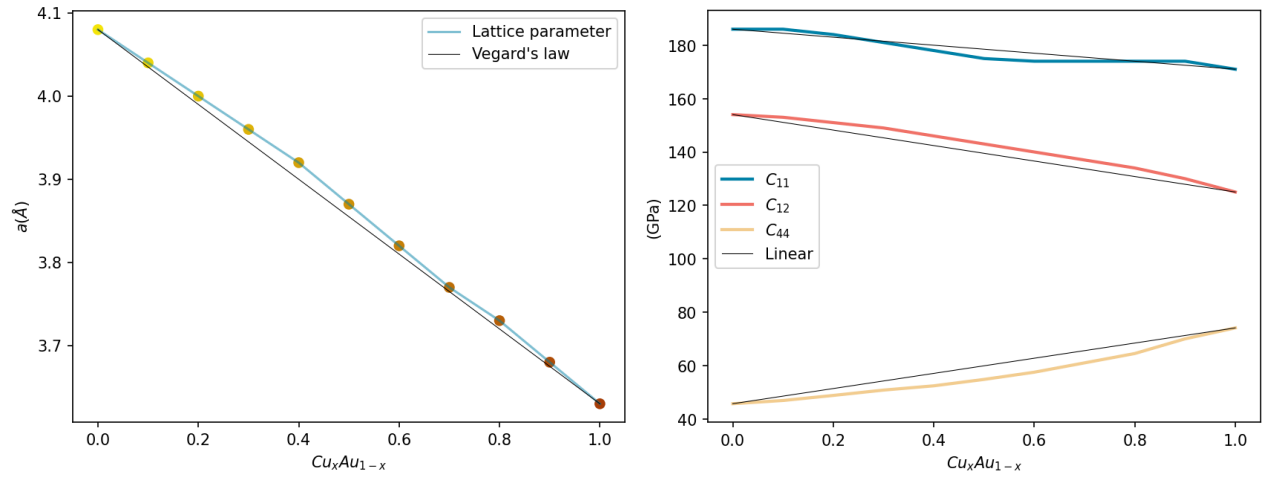

(a) **(b)**

Figure 5.2: Figure (a). Lattice parameter as function of copper concentration in Cu_xAu_{1-x} systems, together with the Vegard's law. Figure (b). Elastic constant as function of the copper concentration in Cu_xAu_{1-x} systems.

the calculated values of ΔH_f for the A_1 structure, and as expected the mixed pattern is stable. It is worth noting that the differences in the elastic constants and lattice parameters due to different randomly generated structures are minor and negligible. This suggests that any local variations due to potential clustering are not significant, and the global behavior of the alloy can be effectively represented as an average.

Furthermore, the lattice parameter demonstrates a linear decrease as the concentration of gold in the alloy diminishes, a behavior that aligns well with Vegard's law[2] as shown in Figure 5.2a. Likewise, the elastic constants appear to scale from gold to copper, following a slightly nonlinear trend as depicted in Figure 5.2b. These subtle non-linearities are more evident when calculating the Young's modulus (see how in Appendix 8.3). Particularly in the (001) direction, we can observe that the Young's modulus stays almost constant in all the Au-rich region (see Figure 5.3a), while in the copper rich, it transitions from gold to copper. A less pronounced deviation is found in the (111) direction (see Figure 5.3b). Understanding the Young's modulus of the bulk solid solution is fundamental step for interpreting the results obtained with the nanoparticles, which are elucidated in the following sections. An intriguing aspect to discuss involves the validity of the results presented in Figure 5.2b. The minor non-linearities leading to significant deviations in the Young's modulus behavior could be artifacts of an imprecise potential or fluctuations due to the cutoff. However, they could also be a manifestation of real physical behavior, which would have profound implications for nanoparticle mechanics. Previous studies have also documented similar nonlinear behaviors of the Young's modulus in the case of NiCo solid solutions [43] suggesting that our results are not the result of an artefact of potential

2: Vegard's law: named after the Norwegian physicist Lars Vegard, is an empirical rule in materials science which describes the relationship between the composition of a solid solution alloy and its lattice parameter. According to Vegard's law, the change in the lattice constant of an alloy is linearly related to the change in the concentration of its constituents. It is not always valid.

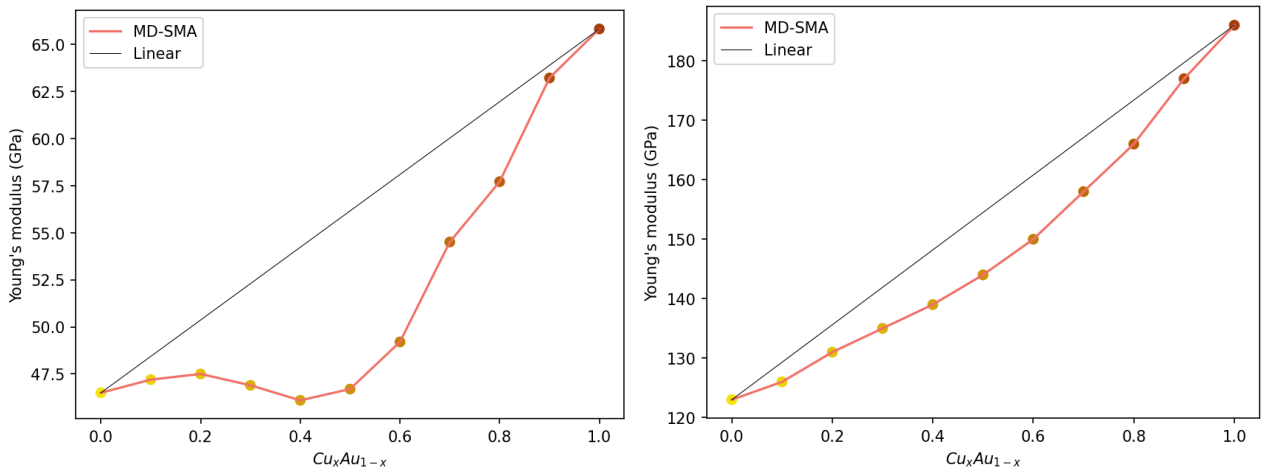

Figure 5.3: Young's modulus as a function of the copper concentration in Cu_xAu_{1-x} systems. Figure (a). (001) direction. Figure (b). (111) direction.

but of real physics to be understood.

An important step to confirm the applicability of the chosen SMA potential in mechanical studies involves the computation of stacking fault energies and unstable stacking fault energies. While these parameters might not significantly influence the analysis of elasticity, they play a vital role in understanding the onset of plasticity and ductility, affecting interactions and movements of dislocations. More details on this subject are available in Appendix 8.6.

5.2 Copper-Gold Nanoparticles

5.2.1 The system

Nanoparticles can exhibit different mixing patterns, which are influenced by various factors, including relative binding energy, surface energy, and atomic size. Elements with lower surface energy tend to stay on the surface to minimize the total energy, while smaller atoms typically occupy the core. Other factors, although less relevant in this context, can also play a role [42].

The main mixing patterns in nanoparticles can be segregated or mixed configuration. Segregated nanoparticles can take the form of core-shell structures, with one or more shells, or Janus nanoparticles, where two different clusters of the same material share a common interface. Mixed nanoparticles, on the other hand, can exhibit ordered or disordered mixing, and a critical temperature defines the transition between the two. Moreover the spectrum of possible pattern is broader, local ordering could vary, segregation at the surfaces can appear also in ordered structures, but this case is not here analysed. In Figure

5.4 we can observe different mixing patterns for a generic system. The phase diagram of the copper-gold nanoparticles is similar to the

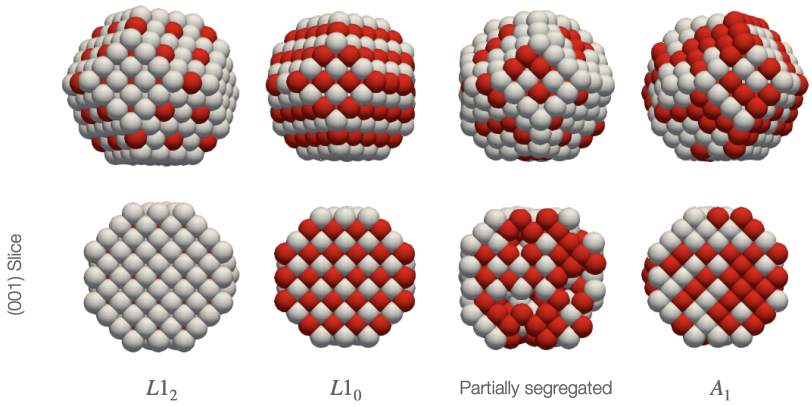

Figure 5.4: Different mixing patterns, starting from the left: the $L1_2$, $L1_0$, partially segregated and solid solution. At the top the nanoparticles and at the bottom a (001) slice.

bulk one presented in Figure 5.1. We encounter ordered $L1_0$ structures for CuAu alloys and $L1_2$ structures in Cu_3Au and $CuAu_3$ at low temperatures. As the temperature increase, the system undergoes a transition towards a solid solution A_1. However, as mentioned before, relative binding energy, surface energy, and atomic size potentially result in segregation.

The copper-gold bulk system exhibits surface segregation, with gold favoring migration to the surface [122, 123]. Furthermore, a recent investigation revealed that gold segregates to the surface while still maintaining a satisfactory degree of mixing at the core [124]. As shown in Table 5.4, gold presents surface energy values approximately 35% lower than those of copper and exhibits a larger lattice parameter. Even if the alloying effect should obviously not be neglected, these characteristics suggest that a certain degree of gold segregation at the surface is to be expected.

For our study, 20 nm with shape $G \sim 0.24$ (from a (001) perspective) nanoparticles are generated with varying concentrations ranging from pure gold to pure copper, using a completely random configuration. The solid solution nanoparticles were then subjected to Monte Carlo minimization (at $T = 800$ K) to look for configurations with lower energy, so as eventually take into account gold segregation at the surface. This approach allows for a more reasonable computational time compared to molecular dynamics simulations.

In Figure 5.5a, we can observe a solid solution nanoparticle on the left-hand side and the same nanoparticle after the Monte Carlo minimization on the right-hand side. Evident segregation can be observed on the surface, indicating a partial segregation phenomenon. It is interesting to note, observing the slice of the two NPs, that at the center of the right nanoparticle, the atoms still appear to be randomly distributed, indicating a lack of significant segregation in the core region as already discussed in [124].

	E_b	a	γ_{001}	γ_{111}
Au	-3.81	4.08	0.30	0.22
Cu	-3.49	3.61	0.48	0.39

Table 5.4: Lattice parameter a (Å) and Binding energyE_b from [6], Surface energies γ_{001} and γ_{111} (eV/at) from [101]

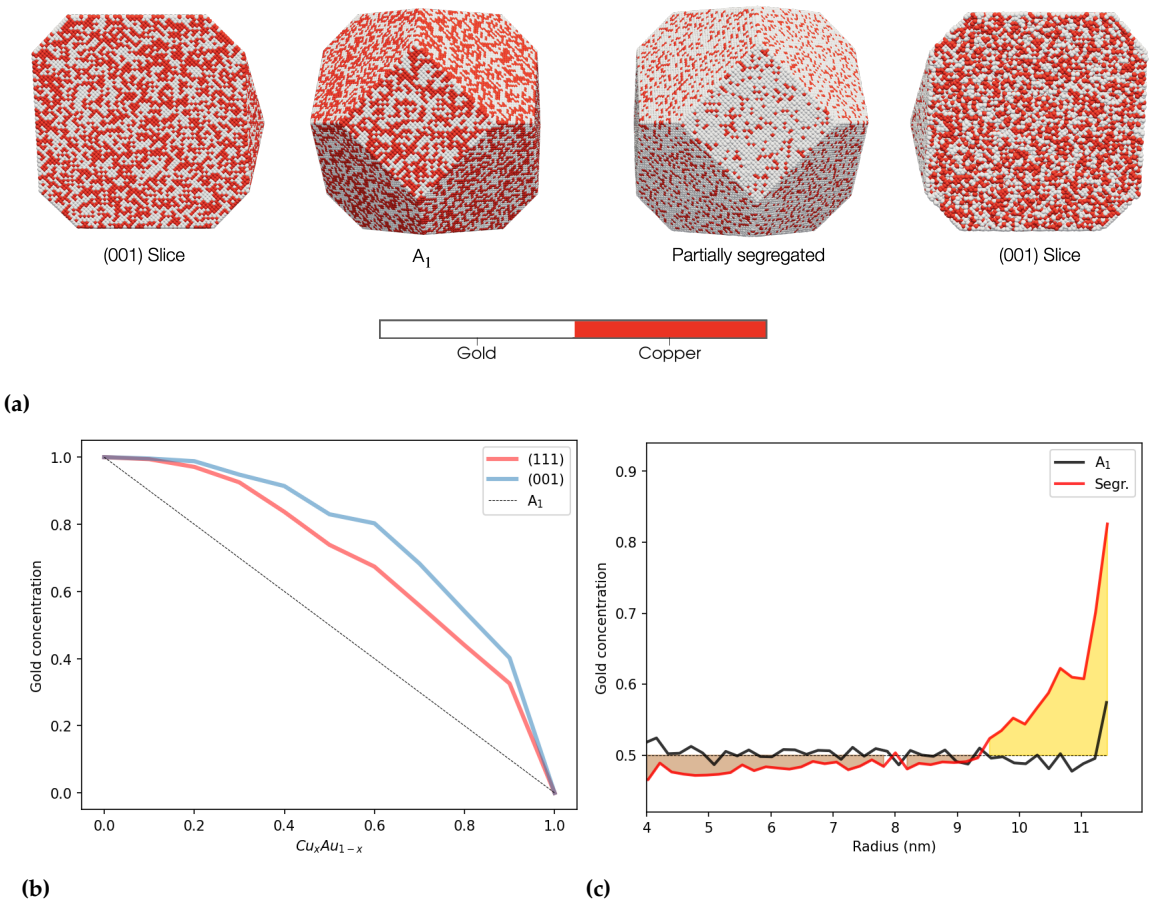

Figure 5.5: Copper gold segregation in the CuAu nanoparticles. Figure (a) At the center the two configurations: A_1, and the same nanoparticle after Monte Carlo minimisation, showing gold segregation at the surface. At the sides the (001) slice shows how segregation concerns only the external layers, while the core is not affected by the process. Figure (b): Surface concentration of gold at the (001) and (111) surfaces. Segregation is weaker in the closed packed (111). Figure (c): gold concentration as a function of a sphere radius. Gold concentration very high only in the last layers and the system stays A_1 in the core atoms.

It is possible to take the analysis a step further and study segregation by facet. In Figures 5.5b and 5.5c, a quantitative analysis of gold concentration at different surfaces, (001) and (111), for partially segregated nanoparticles as a function of an increasing copper concentration is presented. Thanks to the comparison with the solid solution we see that the (001) surface tends to segregate (the Au content) more than the (111) surface, being a closed packed it tends to segregates less [124].

While, as demonstrated above, Au tends to segregate at the surface it is interesting to understand Au/Cu atoms distribution in the inner layers of a partially segregated nanoparticle. To this end, in Figure 5.5c, for two nanoparticles (CuAu - A_1 and the segregated counterpart), gold concentration is plotted as a function of the radial distance from the nanoparticle center. The solid solution is stable around the value of approximately 50% copper concentration throughout, up to the surfaces. In the case of the segregated nanoparticle, the outer shell

is highly enriched in gold. It is important to consider that while the average data may indicate outer shells rich in gold, the second layer of atoms is actually rich in copper, suggesting a more complex atomic arrangement beyond the surface.

The next section presents mechanical testing on nanoparticles. Each nanoparticle consists of 306043 atoms, measures approximately ($d \sim 20nm$, with a truncated octahedral shape with ($G \sim 0.24$ from (001) perspective). In the solid solution A_1 we cover all concentrations from pure gold to pure copper, including their segregated versions (Segr.). Ordered structures are represented by the CuAu-$L1_0$ structure (only with gold top surfaces) and both $CuAu_3$-$L1_2$ and Cu_3Au structures. Note that also $CuAu_3$-$L1_2$ can be terminated in two different ways, with a full Gold or mixed layer at the (001) surfaces, in this case both configuration are considered, the same is valid for the Cu_3Au-$L1_2$. Segregation in ordered structures, similar to disordered ones, is not discussed here, but represents a possible improvement of this work.

5.2.2 Elastic properties of Cu_xAu_{1-x} nanoparticles.

Figure 5.6 presents the stress-strain curves for a set of different mixing patterns, outcome of nano-indentation MD simulation of CuAu NPs on the the (001) facet. As noted in Chapter 4, gold demonstrates softer elastic behavior than copper. Clearly, the A_1 configuration shows a notable change in slope compared to pure gold and copper NP, evidencing smaller E_{eff}. In this particular case, two different random structures are probed (red lines in Figure 5.6) to show the effect of different local distribution not on the elastic regime but only on the plastic onset. Interestingly, the elasticity limit, rather than the effective elastic modulus E_{eff}, shows greater sensitivity to these different local configurations. This demonstrates that local atom arrangement influences the distribution of the stress field inside the nanoparticle and, consequently, the onset of plasticity. In segregated system (blue line), both elastic and plastic behaviour aligns with that of gold. Lastly, in the $L1_0$ structure (with gold surface), an increasing in slope coupled with a reduction in critical stress is observed (black line). Note that the elastic behaviour is still very close to that of pure Au NPs. $CuAu_3$ NPs mechanical properties are investigated and the results are presented in Figure 5.7. Again, the A_1 configuration shows softening compared with pure copper, but has an elastic behavior close to that of gold. In case of Au segregated in solid solution, as before, we tend towards the behaviour of pure gold but the difference between the configurations is less pronounced. In this case, the E_{eff} is comparable with gold as $CuAu_3$ solid solutions are rich in gold. As in the $L1_0$ system, the ordered $L1_2$ system presents an increase in E_{eff}, along with a significantly higher critical stress.

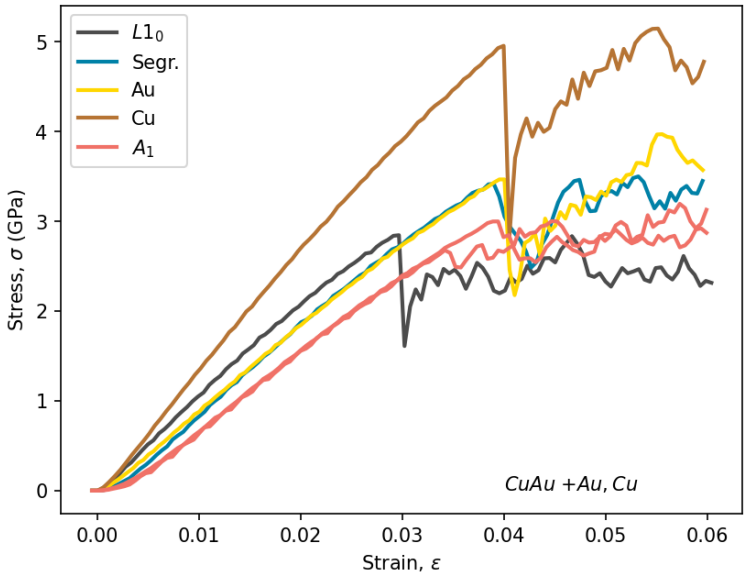

Figure 5.6: Compressive stress and strain curve for 20 nm truncated octahedral CuAu NPs: solid solution (A_1), Au segregation (segr.), ordered compound ($L1_0$) and pure copper and gold. Two A_1 structure are plotted to show the effect of different local distribution not on the elastic regime but only on the plastic onset.

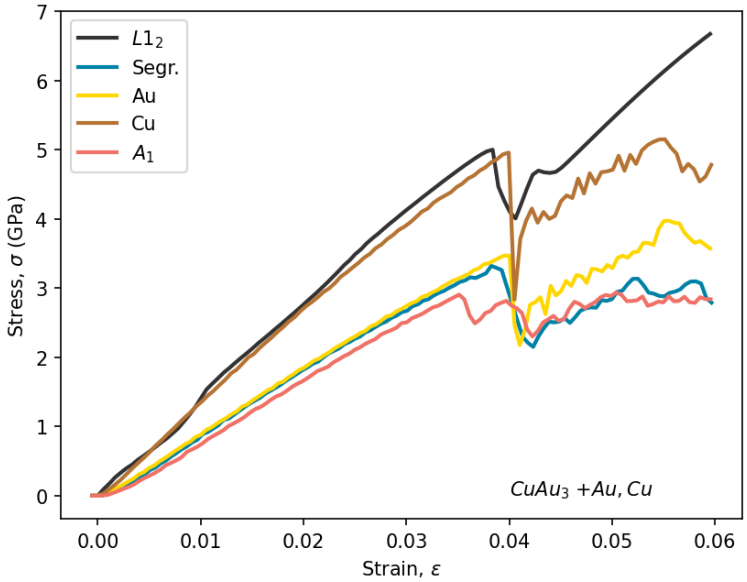

Figure 5.7: Compressive stress and strain curve for 20 nm truncated octahedral $CuAu_3$ NPs: random configuration (A_1), Au segregation (segr.), ordered compound ($L1_2$, with last layer only with gold) and pure copper and gold.

These results are summarized for different concentrations in Figure 5.8. The extraction of E_{eff} is obtained with the method outlined in Chapter 3. Alongside the MD results, the FE elastic calculations are also provided to verify their validity in characterizing the physical properties of alloys. Specifically, this concerns both the A_1 and the ordered structures with the elastic constants extracted as detailed in Section 5.1 (values can be found in Table 5.3). Due to increased complexity, calculations for a segregated structure were not carried out. However, a potential path to undertake could be the method put forth by *Moseley et al.*[61].

Focusing first on the ordered structures, it can be observed that they exhibit higher resistance to deformation on the (001) facet compared to the disordered structures, especially in the case of the $L1_2$ structure. The Finite Element method works effectively for ordered structures,

suggesting that internal stresses from lattice mismatch and the configuration of the structure do not significantly influence the elastic response, keeping it linear. Conversely, in the disordered structures, a significant deviation between the A_1 and the Segr. configurations is observed across all concentrations. This discrepancy is maximal and exceeds 10% for the CuAu system. Counter-intuitively, the FE solution using A_1 elastic constants aligns perfectly with the segregated structure and not with the solid solution. Taking into account what is stated in Chapter Chapter 3, it is not surprising to observe that the FE solution precisely mirrors that of the bulk (see 5.3a), exhibiting a gold-like behaviour up to the 50% concentration. It appears as though gold dictates the mechanical response.

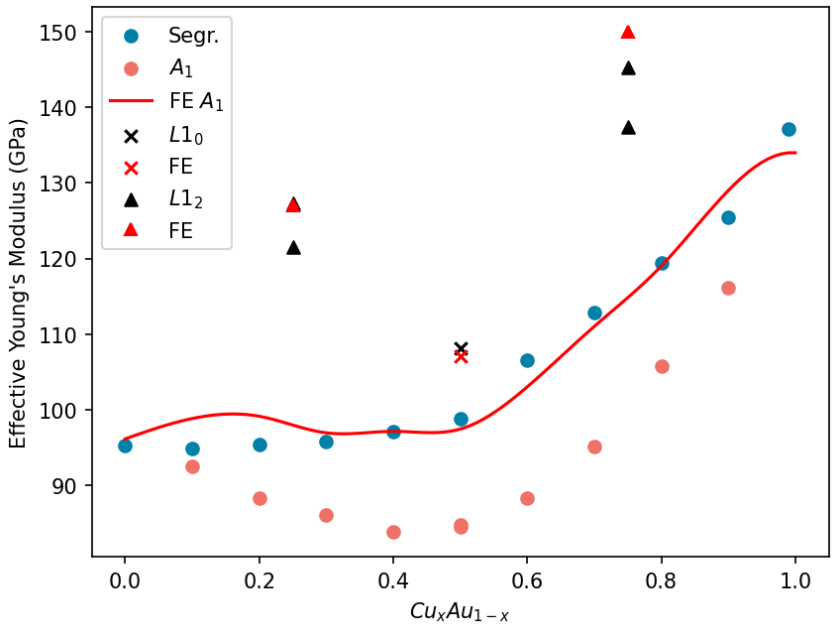

Figure 5.8: (001) Effective Young's modulus at different Cu concentration for 20 nm truncated octahedral NPs, with ordered structure: $L1_0$ and $L1_2$, disordered structure: A_1 and the segregated counterpart. A comparison is proposed with two different methods, Finite Element and Molecular Dynamics.

This distinct disparity may be due to two main factors: a pronounced impact of the outer shell on the comprehensive behavior or a substantial decrease of the residual stress [3] in the segregated configuration, which profoundly transforms the elastic behavior. Importantly, the latter assumption might imply the former. The impact of the shell is probably not the main contribution; the correspondence with the FE results indicates that in the A_1 system, there exists a higher residual stress, resulting in a smaller E_{eff}. As done in case of pure metallic nanoparticles, the calculation of the local stress distribution can be a significant tool to go further in our analysis. Figure 5.9a depicts the σ_{zz} Virial stress distribution in two CuAu nanoparticles: one A_1 and its segregated counterpart. In the segregated nanoparticle, energy minimization results in gold atoms migrating to the surface, thereby significantly reducing the mean (from −100 MPa to 30 MPa) and variance of the stress distribution. The same distribution changes can be observed for σ_{xx} and σ_{yy}. While it is typical for compressed materials ($\sigma_{zz} < 0$) to be stiffer than those under tensile stress ($\sigma_{zz} > 0$), this

3: Intrinsic stress in the undeformed nanoparticle. See Chapter 3 for more details.

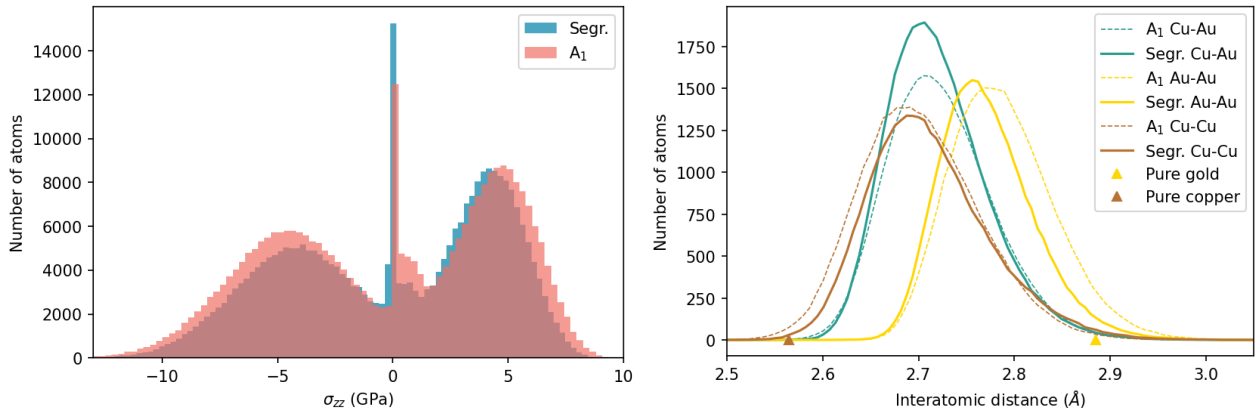

(a) **(b)**

Figure 5.9: Figure (a): residual stress σ_{zz} for indentation on (001) facet, computed with the Virial method for two CuAu configurations : A_1 and the segregated counterpart. Figure (b): comparison of the inter-atomic distances for the three different kind of bond that can be found in a CuAu before and after the segregation: Au-Au, Cu-Cu, and Cu-Au. Results for undeformed nanoparticles.

does not correspond to the observed reduction in stiffness in case of A_1 structures ($\langle\sigma_{zz}\rangle < 0$). This can be explained by recognizing that when a nanoparticle is indented, it is subject to a compressive stress in the z direction and a tensile stress in x and y ones. Thus, the A_1 structure may exhibit a softer response than its segregated version since along the x and y directions, the atoms reduce their compressive stress going towards an equilibrium position, and this effect is not negligible. Figure 5.9b shows the distribution of inter-atomic distances for three bond types (Au-Au, Cu-Cu, and Cu-Au) in CuAu nanoparticles for both the A_1 and the segregated systems. As highlighted by our analysis, the A_1 configuration displays roughly equal distributions for all bond types. Upon segregation, the number of Cu-Au bonds increases with corresponding decreases in the other bond types. Interestingly, the average distances of pure bond types deviate from the lattice parameters found in pure crystals. The system appears to evolve from a random distribution to one predominantly featuring Cu-Au bonds. The predominance of Cu-Au bonds in the segregated NP can also explain the good agreement between E_{eff} computed with FE reported in Figure 5.8: the elastic response of the segregated NP is more similar to an average medium with a fixed value of elastic constants (as in our FE model) than A_1 system, due to the the large number of Cu-Au bonds.

Lastly, let us consider the case of ordered structures. The increased stiffness of $L1_0$ and $L1_2$ structures observed in Figure 5.8 becomes clear when examining Table 5.3. Notably, the Young's modulus of the bulk structure in the (001) direction shows a significant rise compared to both Cu and Au, and this is reflected in the nanoparticle mechanical behaviour. The same analysis is replicated for the (111) facet, preliminary results are available Appendix 8.5.

5.2.3 Plastic properties of Cu_xAu_{1-x} nanoparticles.

As highlighted in the introduction, recent studies indicate that solid solutions often display softer behavior than pure elements. This phenomenon is mainly attributed to the local instability in stacking fault energy, moreover *Bisht et al.* [43] explored and excluded the idea that the strength softening might be linked to an elastic softening, here this idea is reconsidered. Where with elastic softening is meant a reduction in the stiffness.

To investigate the plastic properties of Cu_xAu_{1-x} nanoparticles, we focus our analysis on the critical stress. Figure 5.10 displays the dependence of σ_c on the nanoparticle composition for 20 nm truncated octahedral nanoparticles with indentation on (001) facet. Results are extracted from the stress and strain curves previously utilized for the elasticity study.

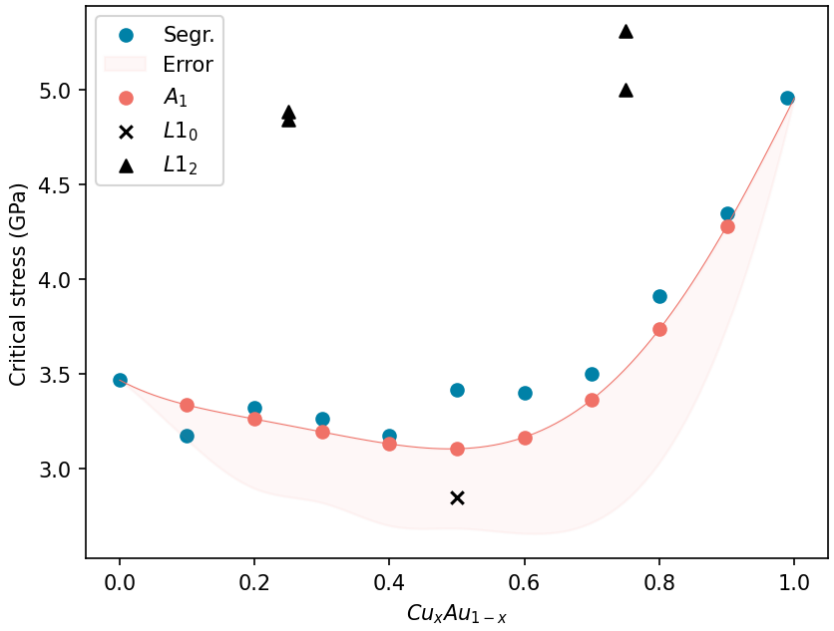

Figure 5.10: Critical stress at different copper concentrations for 20 nm truncated octahedral Cu_xAu_{1-x} NPs with indentation on (001) facet. A_1 and segregated structure for the disordered systems. $L1_2$ and $L1_0$ for the ordered nanoparticles. The red area represents the dispersion for all the tested configurations in case of the A_1 structures.

The first observation here is the softening of the A_1 systems in comparison to the rich states. In other words, if a system is gold-rich, it is softer than gold, and if it is copper-rich, it is softer than Cu. It can also be noted that segregated structure demonstrate a slightly stronger behavior compared to the A_1 systems although it is challenging to make conclusion about the results without adequate statistics. Concerning the results on the ordered structures, the $L1_0$ system is softer with respect its A_1 counterpart. On the contrary, the $L1_2$ structure presents remarkably stronger behavior in both concentrations to reach a critical stress around 5 GPa to be compared with their equivalent in solid solution or segregated system, whose values do not exceed 3.5 GPa. It is useful to specify that the A_1 curve has been produced by considering different local configurations (10

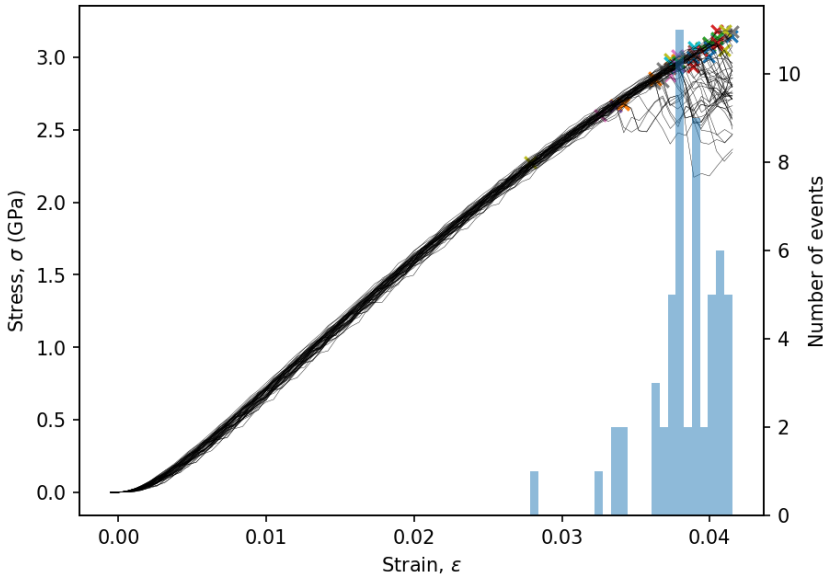

Figure 5.11: Fifty different indentation for the A_1 CuAu structure with different local configuration. A distribution of the critical strain ϵ_c is shown to highlight the dispersion due to different local configuration, that leads to earlier dislocation nucleation.

An analogy for this phenomenon can be found with temperature when temperature is added to a system, atoms start oscillating around an equilibrium position, generating corresponding stress oscillations that introduce stochasticity to the event. The maximum critical stress, $\sigma_{c,max}$, can only be reached at 0K or with a certain probability at a fixed temperature.

per every concentration). This allows us to statistically analyze the nucleation events. The maximum value of critical stress, $\sigma_{c,max}$ is shown with red dots in Figure5.10, while the red area represents the dispersion of σ_c values for all the tested configurations. From these outcomes it is clear that local configurations can trigger nucleation at an earlier stage when the stress due to the local Au-Cu atom distribution is excessively large. Since correct statistics are needed to properly characterize the various plasticity mechanisms, a larger sample size has been considered. In Figure 5.11, the effect of dispersion due to different local arrangement is shown for the A_1-CuAu system from 50 configurations. As seen in the histogram form, ϵ_c (as in the Figure) or σ_c (not shown here) follows a distribution function when copper atoms are present into a gold matrix. This distribution may depend on factors like geometry, alloying concentration, and other possible parameters. While determining these dependencies is beyond the scope of this work, it presents a fascinating direction for future research.

A closer examination of Figure 5.8 reveals a tight correlation between the onset of plasticity (Figure 5.10) and elastic behavior, coherent with the findings of Chapter 4. The $\sigma_{c,max}$ curve is largely dictated by the effective elastic response of the nanoparticles: the elastic softening cause a plastic softening. This is even confirmed by the segregated structures, that consistently demonstrate a higher critical stress compared to A_1 systems.

Bearing this in mind, we can revisit the analysis of nucleation events in solid solutions. First, as highlighted by *Sharma et al.* [46] and *Bisht et al.* [43], various local arrangements can lead to softening: nucleation becomes a statistical event influenced by local clustering. Secondly, strength softening is associated with elastic softening, which

determines the $\sigma_{c,max}$. This second factor is intimately tied to the specific alloy analyzed and might be absent if no elastic softening occurs in the bulk system. This observation aligns with the findings in Chapter 4, where the effective medium response dictates nucleation. The discussion can be further extended to segregated systems: when internal residual stress is reduced, the elastic response is modified (as seen in Figure 5.8), subsequently influencing the plastic response.

On the other side ordered structure ($L1_0$ and $L1_2$) exhibit different behaviors at the onset of plasticity: while one displays softening ($L1_0$), the other shows strengthening ($L1_2$). This discrepancy is likely due to the ease of introducing a stacking fault in the $L1_0$ structure. Since it is not a mixed structure, compared to the $L1_2$ structure, it might facilitate the initiation of plastic deformation. The strengthening mechanism of the $L1_2$ was already observed by *Sharma et al.* [46] and it can be linked again to the stiffer elastic response.

5.2.4 Plastic Behavior in the $L1_0$ structure

An interesting ductile behavior has been observed deforming the $L1_0$ structure. This behavior is reported in this section, for a 20nm cubic CuAu NP. Figure 5.12 shows the stress and strain curve obtained for (001) nano-indentation using MD simulations. We can notice that for low strain, we have a first (usual) elastic regime (region 1) followed by a plastic regime (region 2) where an almost perfect plastic behavior is observed. In region 2, after the nucleation of the first partial dislocation at the critical stress, new dislocation events occurs. The nucleated dislocations shear the cubic NP, exiting from the NP at the opposite surface and leaving behind a stacking fault that completely crosses the NP. Nucleation after nucleation every new stacking fault sums up, changing the bonds locally from a horizontal $L1_0$ to a vertical $L1_0$ as sketched in Figure 5.12. This transition continues until about $\varepsilon = 0.25$, where the structure becomes defect-free, crystalline, and fully shifted in the vertical $L1_0$ structure displaying another elastic stage with different properties (beginning of region 3). After forming the vertical $L1_0$ structure, compressing it in the x or y direction could potentially revert it back to the starting configuration.

Figure 5.13 displays the initial and final structures, both defect-free, illustrating the reversible nature of this process. Similar results are observed also for truncated cubes and truncated octahedrons.

This surprisingly plastic behavior, similarly observed in the literature [125], is promising: with an applied cycling loading the system can go back and forth from two different ordered structures, exhibiting different elastic properties. However, This finding has to be analyzed in details: an examination of the system's stacking fault energy, would facilitate a more precise interpretation the observed mechanisms.

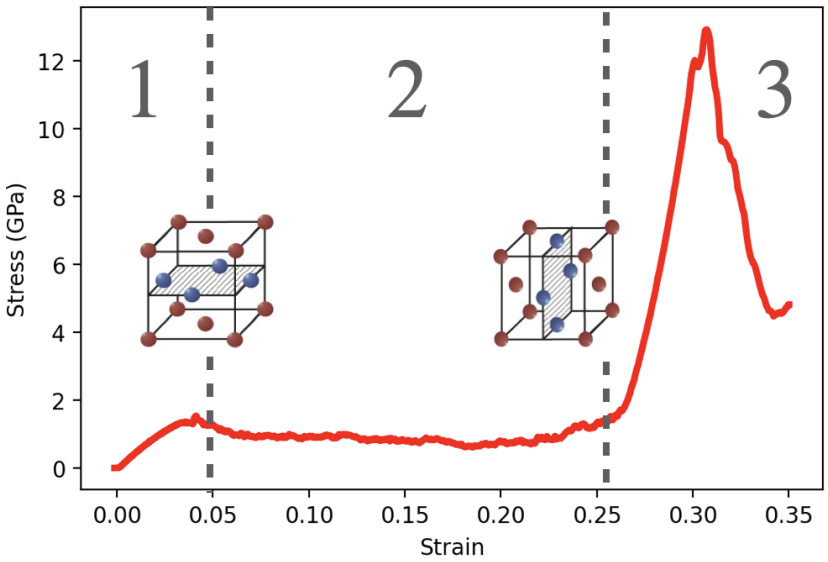

Figure 5.12: 20 nm $L1_0$ indentation stress-strain curve showing initial elastic deformation, followed by plastic deformation with stacking fault pile-up transitioning the structure from horizontal to vertical $L1_0$, and finally complete structure reconstruction leading to a second elastic regime.

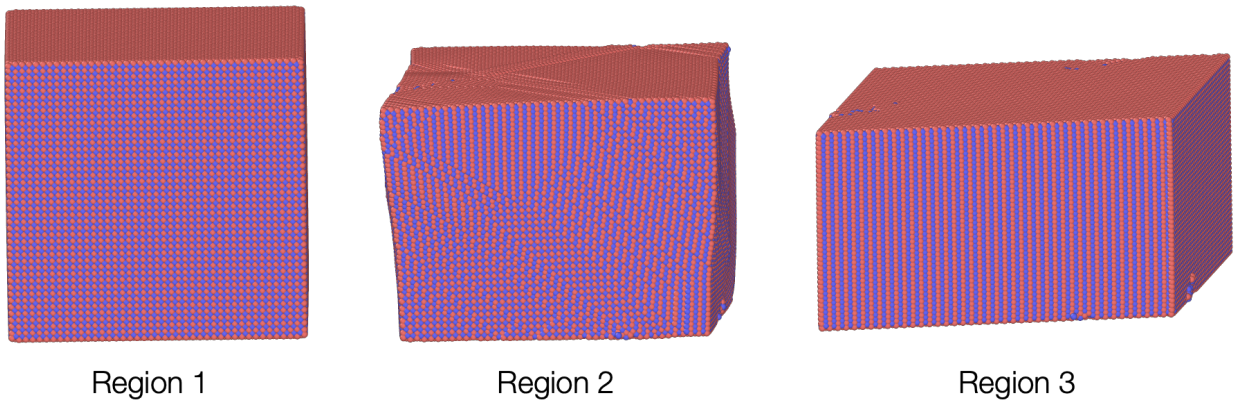

Figure 5.13: Initial, intermediate and final configuration of the cubic $L1_0$ structure analysed. The final structure is perfectly crystalline.

5.3 Conclusion

In this chapter, many key findings regarding the mechanics of nanoalloys are discussed, throughout the different stable phases of the copper-gold system. In disordered structures different elastic behavior can be observed. As the internal stress (residual stress) within nanoparticles increases, their elastic response changes. This change is evident when comparing an A_1 structure to a segregated one. The segregation observed is a way for the material to minimize energy which helps to reduce its internal stress. Moreover the elastic response of the A_1 solid solution is not influenced by local configurations, but it does exhibit elastic softening. Structures with more gold content are softer than pure gold, and those richer in copper are softer than pure copper. In contrast, ordered structures like $L1_0$ and $L1_2$ are stiffer, aligning with bulk properties. This observation are made thanks to the comparison between FE and MD. Following the discussion of Chapter 3 this latter is further validated for alloy systems at the nanoscale

especially for sizes close to 20nm and subject to certain considerations. FE calculations are suitable for disordered structures as long as the internal strain (residual strain) within the nanoparticle is not too high. This requires both similar lattice parameters and good mixing of atoms. If these conditions are not satisfied, the use of Finite Elements might produce divergent results. For ordered structure things works better and good agreement is found for both $L1_0$ and $L1_2$ structures.

Considering the plastic onset, our investigation is a continuation of previous research by *Sharma et al.*, *Bisht et al.*, and *De la Rosa Abad et al.*. Thus, the comparison of A_1 with its segregated counterpart deepens the understanding of nucleation in solid solutions. The plastic softening observed in many A_1 systems can be attributed to two main factors. First, different local configurations can lead to instabilities in USFE, causing earlier nucleation to occur. The second one is the elastic softening, resulting from either the material's natural softening or from residual stresses due to lattice mismatches. This last factor confirms even more the hypothesis exposed in Chapter 4 with nucleation depending mainly on the elastic field. For the $L1_2$ structure, strengthening effect is observed, but it is missing in the $L1_0$ structure. The reasons of both effect are still unknown and represents a possible evolution of this work, that together with a full investigation of SFE and USFE can confirms also the switch mechanism observed in the plastic regime of $L1_0$ structure.

Improving absorption properties of nanoparticles through plastic deformation

6

Catalysis is an indispensable process for contemporary society, used in countless industrial applications, from environmental protection through pollutant degradation to the synthesis of pharmaceuticals. At the core of these catalytic processes, nanoparticles play a fundamental role due to their unique and tunable properties. These properties can be engineered in various ways, one of which is through the deliberate application of strain. This manipulation can, in turn, influence their catalytic efficiency [65, 126].

There exists a well-known relationship between the absorption properties and structural characteristics of a material, as extensively demonstrated by Nørskov and colleagues [61]. A key revelation from their work is the discovery of a correlation between local electronic properties and the absorption of the studied structure. This finding has been exploited to manipulate nanoparticle-catalysed reactions. In this context, our analysis introduces the study of mechanically deformed nanoparticles, inspecting the impact of both elastic deformation and the subsequent plastic regime on local electronic and surface absorption properties.

This chapter starts with the implementation of a tight-binding code to calculate local electronic properties in nanostructures. The development process of the tool, its validation, and its application to our case study, i.e. hydrogen adsorption on platinum nanoparticles, are discussed. Indeed, among the transition elements studied so far, namely Au, Cu and Pt, the latter is the most interesting from a catalytic point of view. In particular, numerous studies in the literature have focused on the use of Pt nanoparticles for the development of hydrogen-based applications[127]. By combining tight-binding analysis based on Nørskov model and DFT calculations, we focus the following study on hydrogen absorption at the surface of Pt nanoparticle under deformation. Of course, the conclusions drawn could easily be generalized to other adsorbed molecules (such as absorption of CO or $\frac{1}{2}O_2$) or other types of catalyst.

6.1 Implementation of the Tight-Binding formalism

In this section, an overview of the main steps needed to implement the code used for the local density of states calculations (equation 1.19) is presented. The starting point of our work is a pre-existing code, developed by Dr Sylvan Latil (CEA Saclay), capable of computing local DOS on single-orbital systems and implemented in Fortran following

the tight-binding formalism described in Section 2.5. After building the Hamiltonian, the recursion method is used to tridiagonalize the matrix and the Green function method to calculate the local DOS. The required inputs including hopping integrals, on-site energies, lattice parameters, and so forth.

We expand the pre-existing code to facilitate multi-orbital studies, as only s orbitals are considered, and therefore not adequate for the study of transition metals. As usual, hopping integrals are geometrically constructed using the Slater-Koster (SK) method [70, 71]. Consequently, we have at our disposal a complete set of basis integrating the s, p and d orbitals. Moreover, hopping integrals are until now fixed in the code and do not explicitly take into account distance dependencies. To overcome these two limitations in our code, the value of the hopping integral is now exponentially modulated with the distance, denoted by $V_{\text{hop}} = V_{\text{sk}} \cdot e^{-q\cdot(r/r_0-1)}$, where r_0 is the lattice parameter, V_{sk} is the SK output with hopping parameters extracted from [72], and q is a fitted value based on DFT results. This spatial dependency is crucial when examining strained materials, ensuring that strained structures provide different results compared to non-strained structures.

For a proper study of local electronic properties of nanoparticles, the determination of the Fermi level (E_f) is fundamental. This is obtained by imposing a certain number of electrons per atom (for platinum, we consider $[Xe]4f^{14}5d^96s^1$, accounting only for the spd electrons of the last shell, thus considering 10 electrons) and identifying the energy at which this condition is met. It is then important to integrate over the DOS:

$$\int_{-\infty}^{E_f} \text{DOS}(E), dE = 10 \tag{6.1}$$

This method works perfectly in bulk materials, but challenges arise when dealing with surfaces, as in the case of nanoparticles. For this reason, it is required to perform self-consistent calculations, a necessary choice to acquire an accurate Fermi level [128]. The Fermi level is defined by the total density of states (DOS). Nevertheless,

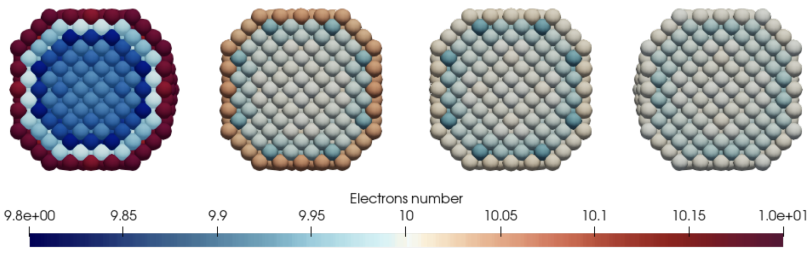

Figure 6.1: Evolution of the electrons numbers during the self-consistent loop in case of a Pt nanoparticle.

local charging effects can occur due to the non-conservation of the total electron number. These effects manifest after imposing a global

$V_{dd\sigma}$	$V_{dd\pi}$	$V_{dd\delta}$	$V_{pd\sigma}$	$V_{pd\pi}$	
−0.9328	0.4800	−0.0800	−1.1651	0.3328	
$V_{ss\sigma}$	$V_{sp\sigma}$	$V_{pp\sigma}$	$V_{pp\pi}$	$V_{sd\sigma}$	
−1.0660	1.5227	2.5410	−0.3354	−0.8431	
ϵ_s	ϵ_p	ϵ_d	q_σ	q_π	q_δ
10.5293	20.2021	6.1859	4.3660	5.5890	6.2247

Table 6.1: Hopping integrals extracted from [72]. Exponential parameters q_σ, q_π, q_δ are calculated from DFT calculation with in cooperation with Dr Cyrille Bareteau (CEA Saclay), the spatial dependence for the s and p orbitals is set to 1.

Fermi level on the local density of states. In nanoparticles, where the majority of atoms are in the core, enforcing the bulk Fermi level on the surfaces, edges, and corner atoms leads to local and artificial charging. To reduce these local charging effects, we implement a self-consistent loop. During this process, the on-site energy of each atom (represented by the diagonal components of the Hamiltonian) is adjusted until charge conservation is achieved, thereby ensuring the correct number of electrons per atom. By iteratively updating these on-site energies, the self-consistent loop enables a more accurate calculation of the Fermi level and eliminates the local charging effects (results are considered converged when the relative error is less than $\epsilon_r < 8 \cdot 10^{-4}$). A detailed illustration is presented in Figure 6.1, where from left to right, we can observe the evolution of the electron numbers per atom from a charged system to a neutral system, over four iteration loops.

We ultimately implemented the code in Python, with all functions written in Fortran, striking a balance between computing time and a user-friendly interface for effective data post-processing. Furthermore, the code is fully parallelized to allow the study of large systems, which would otherwise be impossible. Everything is validated through the study of well-known cases such as graphene or bulk platinum.

6.1.1 Validation of the tight-binding model

As previously mentioned, we perform different tests on various examples. Of course, a crucial step is the fitting of the tight-binding parameters to reproduce the electronic properties of platinum as accurately as possible. To carry out this work, we collaborated with Dr Cyrille Bareteau (CEA Saclay). The final parameters are presented in the table 6.1. A demonstration is provided in Figure 6.2a, where we present a comparison between the total density of states obtained from the Density Functional Theory and our tight-binding calculations for a FCC bulk platinum.

It is interesting to see that the tight-binding DOS adeptly replicates the key characteristics of the DFT one.

Additionally, Figure 6.2a provides insight into the primary contributions from different orbitals. The s orbitals, for example, show a wide

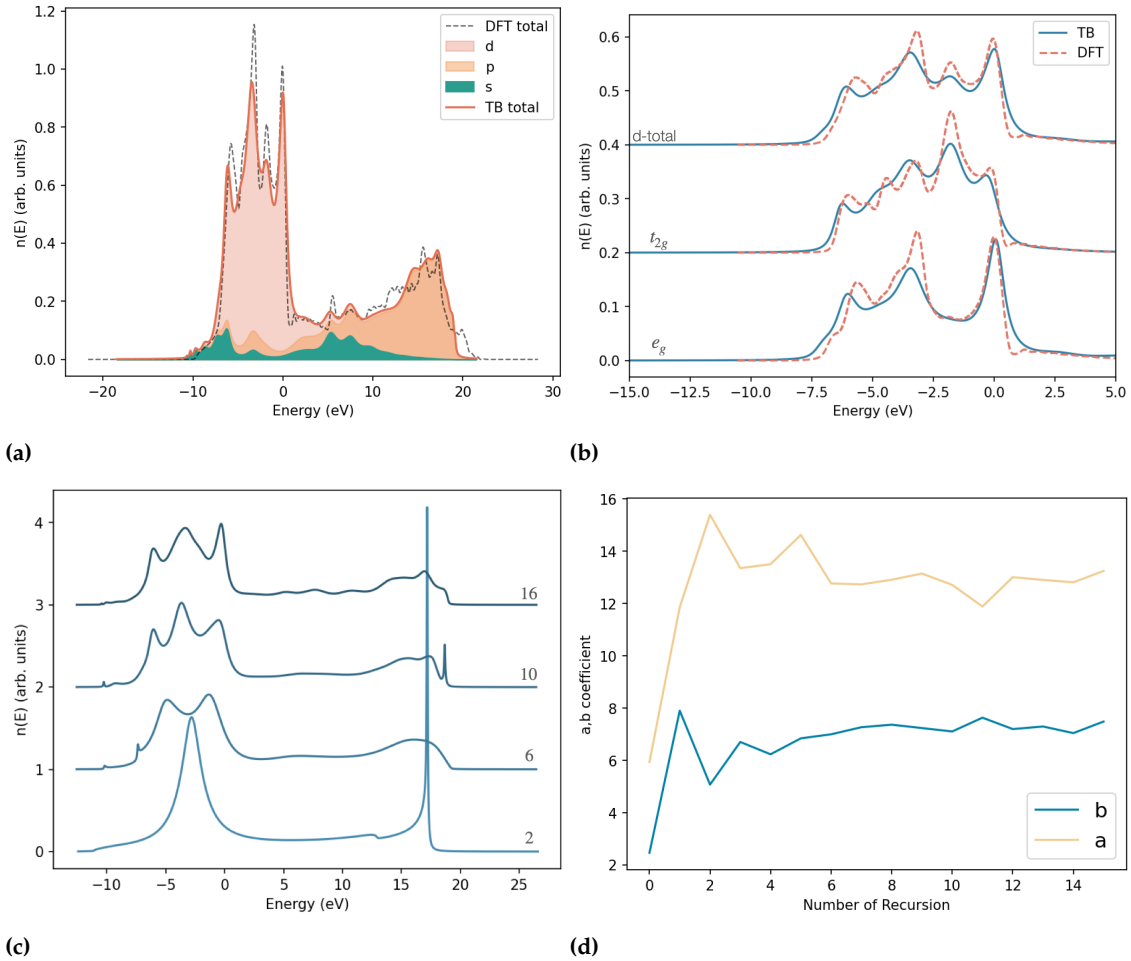

Figure 6.2: Total DOS obtained from tight-binding and DFT calculations for a bulk FCC Pt. Figure (a) The different spd contributions. Figure (b) t_{2g} and e_g families. In all cases, the Fermi level is set to zero. Figure (c): Evolution of the tight-binding total DOS together with the number of coefficient of the continued fraction (a and b) computed. Figure (d): Evolution of the coefficients a, b.

energy distribution, reflecting their delocalized nature and substantial overlap integral. Similarly, p orbitals, while mirroring this behavior, occur at slightly elevated energies. Conversely, the d-band shows a marked different behavior. The energy levels are highly localized, which is consistent with the specific properties of d-orbitals, often being less delocalized and having a more significant role in determining chemical properties. Furthermore, we note the Fermi level aligns with the rightmost peak, this is the reason behind the good behaviour in catalysis of platinum [73]. Shifting our focus to Figure 6.2b, we present a comparison of the methodologies on two different sets of orbitals within the d-band since in the case of a cubic symmetry system, a judicious choice of axes can be used to classify the d levels into two groups: e_g ($\frac{x^2-y^2}{2}$, $\frac{3z^2-r^2}{2\sqrt{3}}$) and t_{2g} (xy, yz, zx). Once again, we find a very good agreement between the two methods. Consequently, our tight-binding parameters are perfectly adapted to deal with Pt systems and this is especially true when looking at the d-band in terms of mean (μ_1) and variance (μ_2) even if all the peaks are not

perfectly reproduced.

Using this set of parameters, we present some calculated densities of states for the FCC structure, enabling us to judge the accuracy of the model. The series of recursion coefficients (a, b) associated with the calculation of the density of states is shown in Figure 6.2d. This series converges fairly rapidly with the number of levels of the continued fraction. In many cases, therefore, it is possible to consider only the first levels of the continued fraction to study the energetic properties of transition metals. Figure 6.2c shows how the density of states varies with the number of coefficients calculated exactly. It can be seen that the main details appear rapidly with the number of coefficients (here 16). To assess the robustness of our parameterization

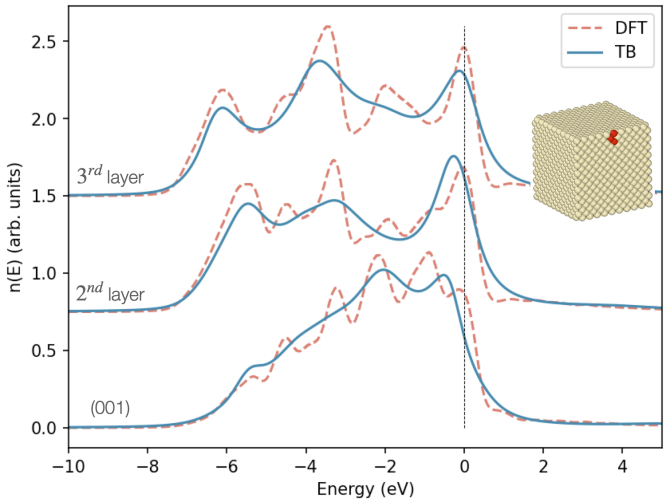

Figure 6.3: Transition of d-*ldos* from the (001) surface to the bulk, in three different layers. Comparison between tight-binding and DFT results.

and the effectiveness of our self-consistency loop in ensuring charge neutrality, we calculate the d-*ldos* of a Pt (001) surface. The results presented in Figure 6.3 show again a good agreement for all three layers (surface, sub-surface and sub-sub-surface). The same behavior is obtained for the (111) surface and is not presented here. This analysis of Pt surfaces confirms that our TB tool is perfectly suited to the case of Pt nanoparticles with (001) and (111) facets.

6.1.2 Electronic properties of pristine Pt nanoparticles

The study can now move on the study of an unstrained, defect-free nanoparticle. These investigations, which provide insights into perfect conditions, are very important to understand the following sections. For practical reasons, such as keeping the computation time for DFT calculations reasonable, the analysis are performed on a small-sized truncated octahedron made of 405 platinum atoms. Figure 6.9 presents the local density of states of specific sites present at the surface from DFT and tight-binding calculations. Here again, the main characteristics are perfectly reproduced, whether for vertices,

edges, or atoms on (001) and (111) facets. At first sight, the width of the d is well related to the coordination number (Z_i) of each site i according to the following sequence: $Z_i^{vertice} < Z_i^{edge} < Z_i^{(001)} < Z_i^{(111)}$. As discussed in Chapter 1.4, first and second moments (μ_1 and μ_2) of

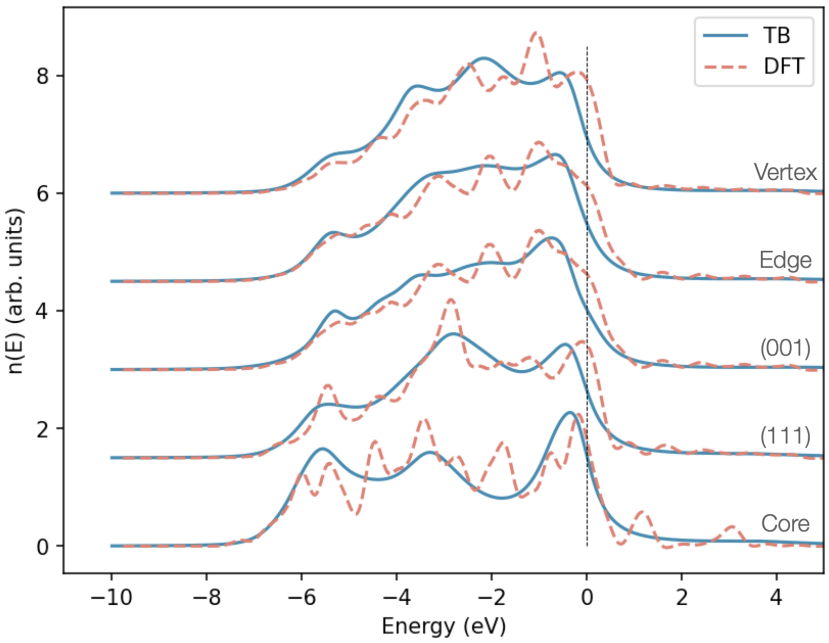

Figure 6.4: The local density of states is investigated at four distinct sites within a nanoparticle: the corner, the (001) facet, the (111) facet, and the core atom. Results were obtained using two different methods: Density Functional Theory and Tight-Binding. These studies were done on a nanoparticle containing 405 atoms, characterized by a truncated octahedral shape. The Fermi level is set to zero.

ldos are relevant quantities for identifying the catalytic properties of nano-objects. As a result, from the local density of states presented in Figure 6.4, we determine these quantities from both DFT and tight-binding calculations (equation 1.20). Results for the first moment

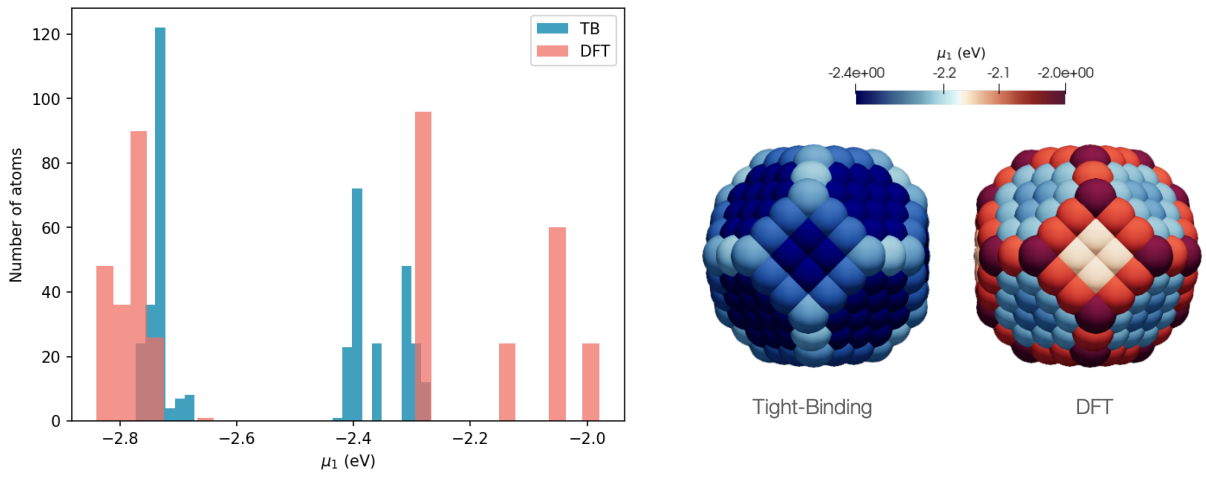

(a) **(b)**

Figure 6.5: Analysis of the first moment distribution for a Pt nanoparticle containing 405 atoms. Results were obtained using tight-binding and DFT calculations.

are presented in Figure 6.5a in a histogram form where different populations of atoms can be identified. As expected, the values of μ_1 change according to the coordination number of each atom. Regarding

tight-binding calculations, μ_1 lie between −2.8 and −2.6 eV for the bulk atoms which have 12 neighbors. The second population corresponds to the surface atoms which first moment values are above −2.4 eV. Then, edges and vertices are observed with lower coordination. This distribution is more clearly visible in the Figure 6.5b where a direct insight of the local μ_1 assignment on the surface of the nanoparticle is presented. In case of DFT results, a noticeable shift in the μ_1 values is revealed compared to those obtained from tight-binding calculations. Furthermore, the main populations are also present but the different families are not as well identified (see Figures 6.5a and b).

Our findings significantly improve when examining the second moment, parameter related to the *ldos* width. In Figure 6.6a, we observe

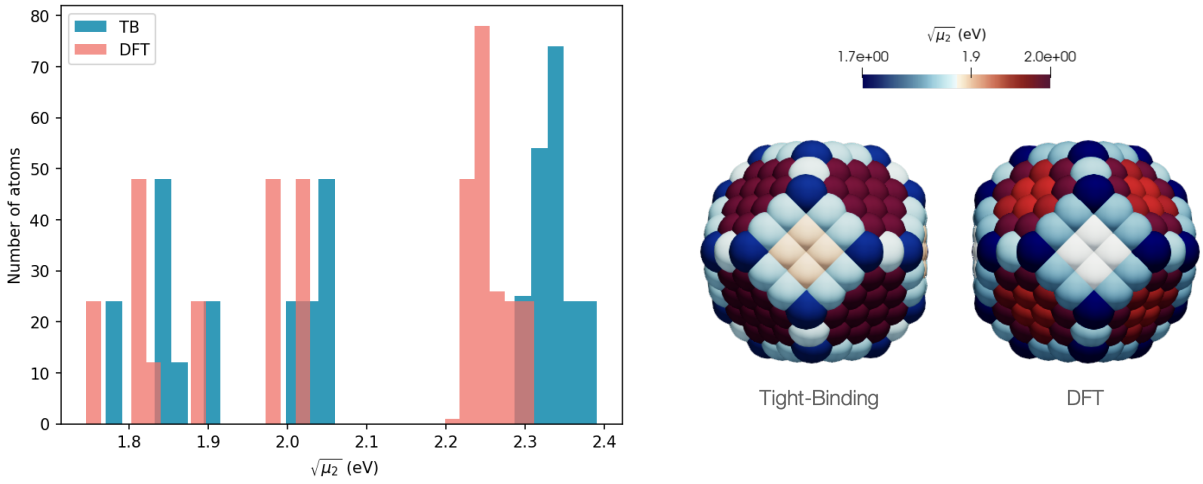

(a) **(b)**

Figure 6.6: Analysis of the second moment distribution for a Pt nanoparticle containing 405 atoms. Results were obtained using tight-binding and DFT calculations.

a stronger resemblance between the calculated histograms obtained by both methods compared to the μ_1 distribution. Indeed, except a minor rigid shift, tight-binding and DFT results align almost perfectly allowing a more precise reproduction of the various atom families and their dependence on the coordination number. Bulk atoms with higher coordination have $\sqrt{\mu_2}$ values between 2.2 and 2.4 eV while atoms with lower coordination have lower $\sqrt{\mu_2}$ values (around 1.7 to 2.1 eV). As a result, both methods successfully capture the expected decrease in the bandwidth as we reduce the coordination number (see Figure 6.6b). The ultimate aim of our work is to study the local electronic properties of nano-objects, with a particular emphasis on absorption properties. As discussed in the first chapter, these properties are directly linked to the first moments of the site. However, the limited precision of the tight-binding method in describing the first moment poses a challenge. First and second moments are linearly related, with the relationship expressed as $\mu_1 \propto \sqrt{\mu_2}$ [129], in Figure 6.7 this is verified for all the *ldos* DFT computed on the 405 atoms

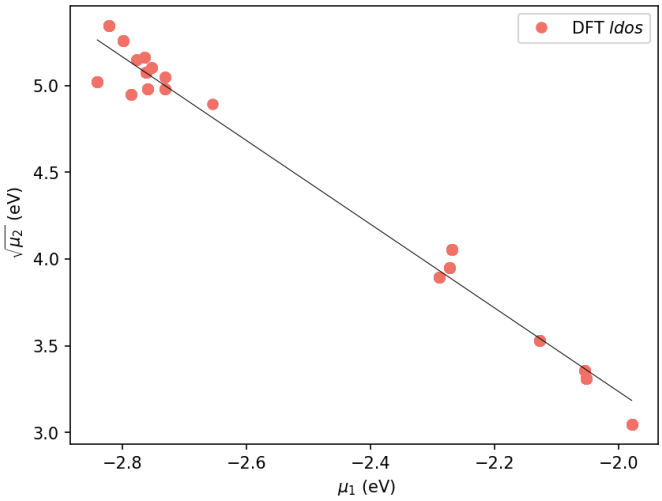

Figure 6.7: Linearity between μ_1 and $\sqrt{\mu_2}$, for our *ldos* calculation of nanoparticle in Step 1.

nanoparticle system. Given the promising results in describing the second moment using the TB method and its linear relationship with the first moment, we have decided to proceed by focusing our study on μ_2 in the context of nanoparticles subjected to both elastic and plastic deformation. This approach, we believe, will enable us to better understand and quantify the impact of structural deformations on the electronic and absorption properties.

6.2 Elastic deformation and first plastic event

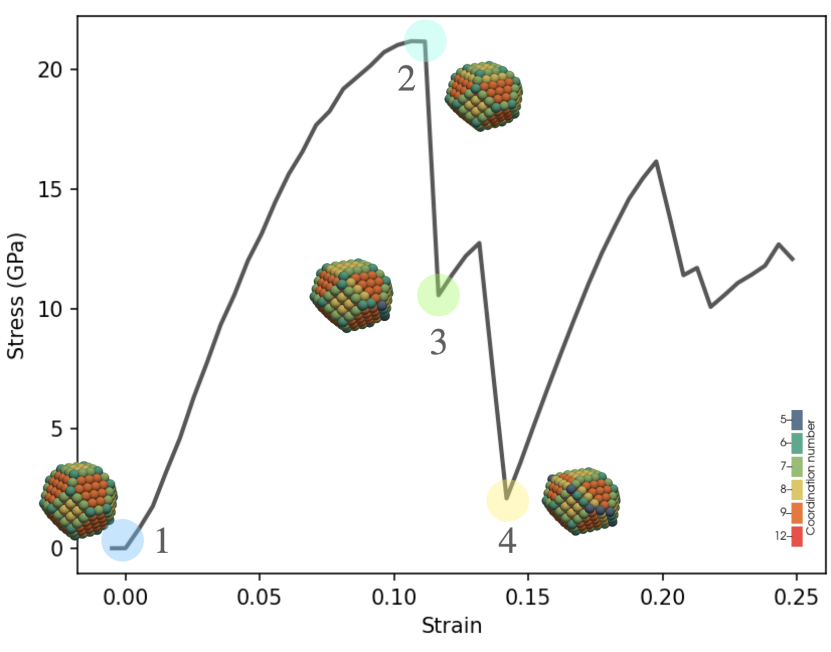

Figure 6.8: Stress ans strain curve obtained with MD calculations for a truncated octahedral Pt nanoparticle containing 405 atoms. The curve is annotated with the various steps at which electronic properties are analyzed. The colors represent the coordination of each atom.

We now focus on the impact of mechanical deformations on the electronic properties of nanoparticles and the link with their catalytic reactivities. Figure 6.8 presents a standard stress and strain curve

obtained through the indentation of a truncated octahedron platinum nanoparticle containing 405 atoms. The methodology is detailed in Section 2.3. While the nanoparticle in its initial configuration (step 1) has already been analyzed within the prior Section, we now investigate the consequences of elastic deformation (step 2) and plastic deformations, by introducing one or two stacking defects (steps 3 and 4), on the electronic properties.

6.2.1 Elastically deformed nanoparticle

Let first consider the effect of elastic deformation on the electronic properties of a Pt nanoparticle. For this purpose, we consider an elastically strained nanoparticle just before the first nucleation occurs. This corresponds to step 2 in Figure 6.8 for a highly strained ($\varepsilon \sim 0.1$) nanoparticle and leading to a high amount of stress (around 20 GPa).

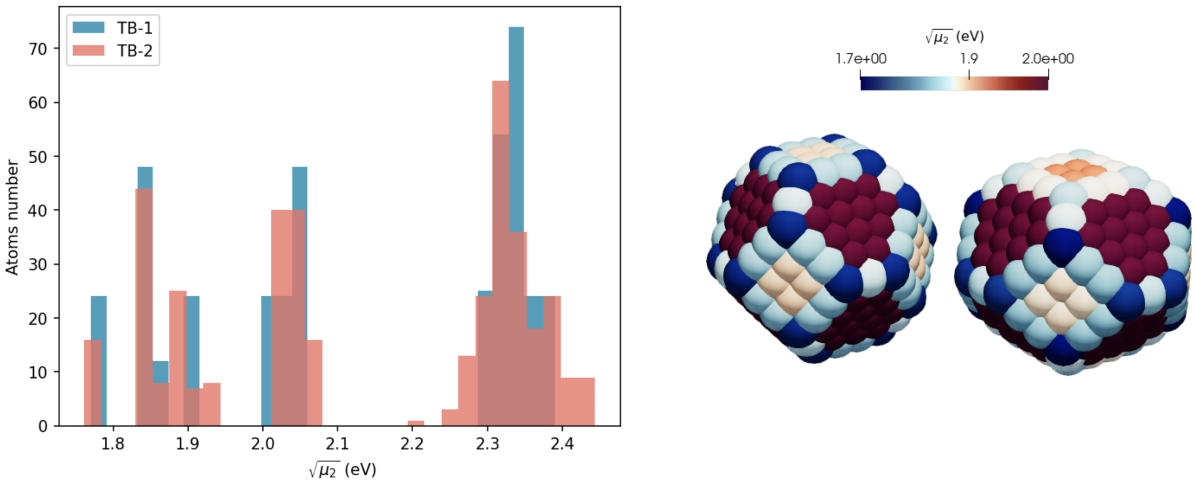

(a) **(b)**

Figure 6.9: Effect of strain on the electronic properties of a Pt 405 nanoparticle by comparing before (step 1) and after (step 2) elastic deformation. Tight-binding analysis of the local μ_2 distribution (a) in a histogram form and (b) on surface sites of the nanoparticle.

Figure 6.9a shows the local distribution of the second moment for each atom in a histogram form before (in blue) and after the elastic deformation (in red). As previously discussed, different populations can be identified, i.e. bulk atoms and surface sites such as vertices, edges and atoms on (111) and (001) facets. For the core atoms, the stress spreads the local μ_2 distribution but does not change the average value. The effect of stress is mostly noticeable at the top surface, where the indenter load is applied. Indeed, we see a small shift (less than 0.01 eV) of the local μ_2 distribution to both left and right. To go beyond, the surface site analysis in 6.9b provides a direct insight into the distribution at the surface of the nanoparticle and confirms the presence of different populations. Under uniaxial stress, atoms present

in the middle of the facet are compressed because they cannot relaxed leading to a right shift in the histogram distribution. In contrast, the atoms on the sides (such as edges or vertices) can relax, reducing the average stress on each atom. Such mechanism induces the leftward μ_2 shift as seen in the histogram analysis. However, it is important to note that these changes in electronic properties are very small even for large elastic deformations.

To conclude, our study based on tight-binding calculations clearly shows that electronic properties are little altered during elastic uniaxial deformation. It is worth pointing out that such elastic stresses can exist as soon as nanoparticles are inserted into matrices, as is often the case for practical needs. This strongly suggests that the various applications envisaged for the use of Pt nanoparticles will not be affected by elastic deformation such as catalytic reactions.

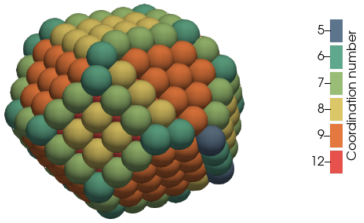

Figure 6.10: Change in coordination number for the nanoparticle in Step 3.

6.2.2 PLASTICALLY DEFORMED NANOPARTICLE

In this section, the impact of plastic deformation on local electronic properties is analyzed. More precisely, the case presented here corresponds to step 3 in Figure 6.8 where the nanoparticle reaches the plastic regime just after the critical stress. As seen in Chapter 4, this transition from elastic to plastic behaviour is due to the dislocation nucleation at the top corner which moves on its slip plane until it gets out, leaving a trace behind. As seen in Figure 6.10, such phenomenon lead to a surface step all around the nanoparticle with the presence of a stacking fault inside. The emergence of the surface step allows the creation of new different sites with specific electronic properties since there is a significant change in terms of coordination.

Once the stacking fault is created, the nanoparticle is relaxed within MD calculations to remove the effect of the indenter, allowing to simulate a more realistic nanoparticle.

Figure 6.11a depicts the local distribution of the second moment for the surface's atoms ($\sqrt{\mu_2} < 2.2$) in a histogram form of the initial nanoparticle (step 1) and after the first plastic event (step3). As we can observe, electronic properties of surface sites are clearly altered. Interestingly, our analysis shows the presence of sites whose coordinates largely change during plastic deformation with very low values of $\sqrt{\mu_2}$ around 1.7 eV. Besides, the surface site analysis in Figure 6.11b clearly reveals the atoms affected. Indeed, the presence of a surface step around a stacking fault results in the formation of surface atoms whose coordination is considerably reduced, narrowing their bandwidth.

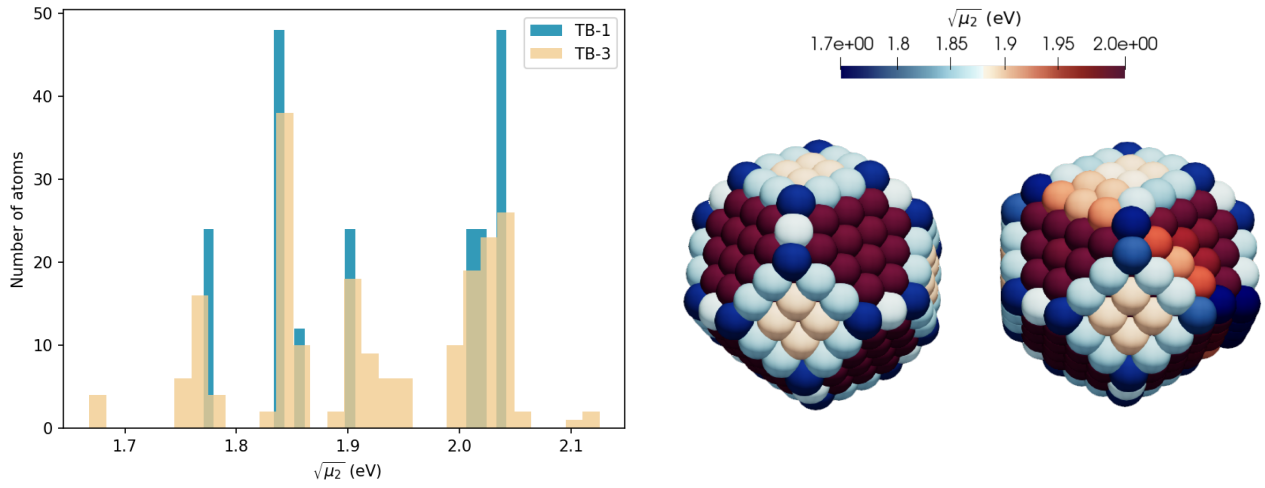

(a) **(b)**

Figure 6.11: Effect of strain on the electronic properties of a Pt 405 nanoparticle by comparing before (step 1) and after (step 3) plastic deformation. Tight-binding analysis of the local μ_2 distribution. Figure (a): in a histogram form with a zoom on the surface sites. Figure: (b) on surface sites of the nanoparticle.

Consequently, our tight-binding analysis highlighted the fact that electronic properties are strongly modified in the plastic regime. Although the characteristic peaked distribution that gives nanoparticles their unique selectivity attributes is lost with the plastic transition, this change is significant and could potentially enhance the absorption properties of a nanoparticle, making it beneficial for catalytic reactions. To assess this assumption, we chose to couple our tight-binding model to DFT calculations of hydrogen adsorption on plastically deformed nanoparticle.

6.2.3 ADSORPTION OF H ON A PLATINUM NANOPARTICLE FROM DFT CALCULATIONS

It is useful to see whether the conclusions drawn from the tight-binding model are correct for the plastically deformed nanoparticle corresponding to step 3. For this purpose, analysis of the local surface μ_2 distribution from DFT calculations are presented in Figure 6.12 for the Pt nanoparticle under analysis. Through this comparison, it seems that DFT calculations are in good agreement with our tight-binding model where a minor shift between the two distribution in the histograms is observed. More interestingly, sub-coordinated sites giving rise to a reduction of μ_2 are also present in case of DFT calculations. To go beyond, we perform DFT calculations of H absorption on a Pt nanoparticle with or without plastic deformation and on specific sites identified thanks to our tight-binding analysis. In this context, the quantity of interest is the absorption energy, E_{abs},

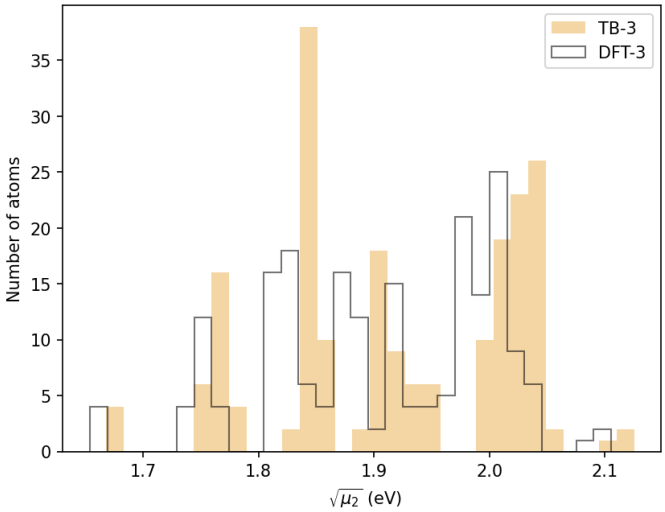

Figure 6.12: Comparison of $\sqrt{\mu_2}$ computed with two different methods, DFT and TB for the surface sites. Step 3 nanoparticle.

defined as follows:

$$E_{abs} = E_{NP+H} - E_{NP} - \frac{1}{2}E_{H_2} \tag{6.2}$$

with E_{NP+H} the total energy including the Pt nanoparticle and the absorbed hydrogen, E_{NP} the total energy of the isolated Pt nanoparticle, and E_{H_2} the total energy of a H_2 molecule. In all cases, two types of calculation are carried out, i.e. to investigate the H absorption on a static Pt nanoparticle whose structure is directly derived from MD simulations as well as Pt nanoparticles relaxed from DFT calculations. Note that DFT calculations are performed with the help of Dr. Hakim Amara (LEM/ONERA-CNRS), using the Quantum Espresso code [130, 131]. To highlight the possible effect of plastic deformation on

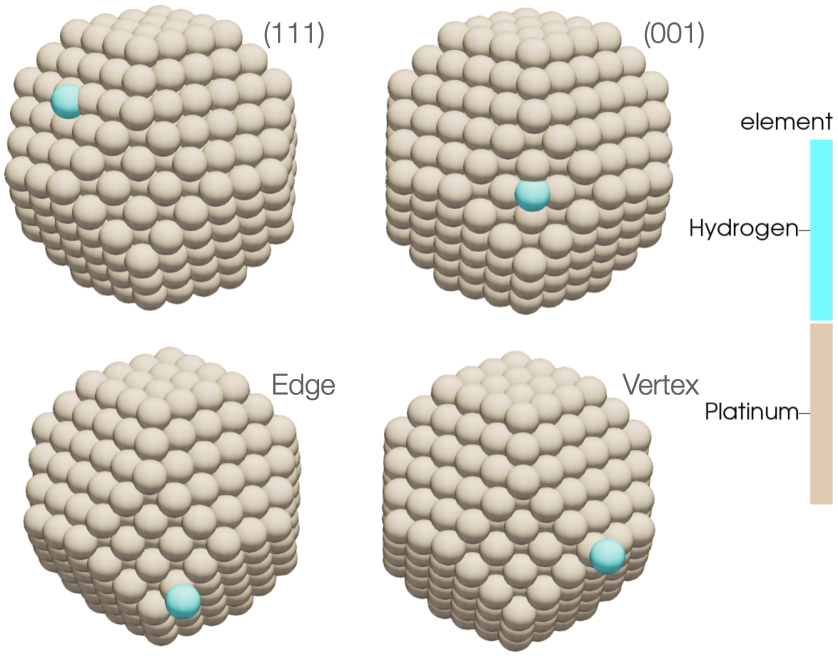

Figure 6.13: Final configuration in the chemisorption energy calculation, in four different sites of interest: (111), (001), Edges, and vertex. Hydrogen on the surface of 405 atoms nanoparticle.

the H absorption properties, the initial nanoparticle must naturally be considered as a reference. In this case, we study the interaction of H with specific surface sites namely vertices, edges, (001) and (111) facets. Results are presented in Table 6.2. According to our calcula-

	μ_2	$E_{abs,relax}$	$E_{abs,static}$
(111)	2.04	-0.414	-0.348
(001)	1.90	-0.253	-0.144
Edges	1.84	-0.517	-0.519
Vertex	1.77	-0.438	-0.516

Table 6.2: DFT absorption energy calculation, with and without atomic relaxation, together with the second moment.

tions, it seems that sub-coordinated atoms favor the adsorption of H. This is particularly true in case of static calculations where the following hierarchy is observed : $E_{abs}^{(001)} < E_{abs}^{(111)} < E_{abs}^{(vertex)} \simeq E_{abs}^{(edge)}$. At this point, we can precise that the final configurations obtained after relaxation of the H atom do not correspond specifically to interaction with a single surface site of the Pt nanoparticle, but several, as can be seen in the Figure 6.13.

When moving to the plastically deformed Pt nanoparticle, atoms that exhibit a significant reduction in μ_2 are selected for absorption calculation. Specifically, we focus on three atoms on the (111) surface that (see Figure 6.14), after the introduction of a stacking fault, transition to being part of a step. In Table 6.3, we highlight the impact of plasticity on the absorption energy. Whatever the type of calculations, these different sites give rise to absorption energies of around -0.5 eV which are very close to the preferential sites obtained for the initial nanoparticle. In other words, the plastic transition transforms (111) to edge like sites, that are highly favorable to the adsorption of H.

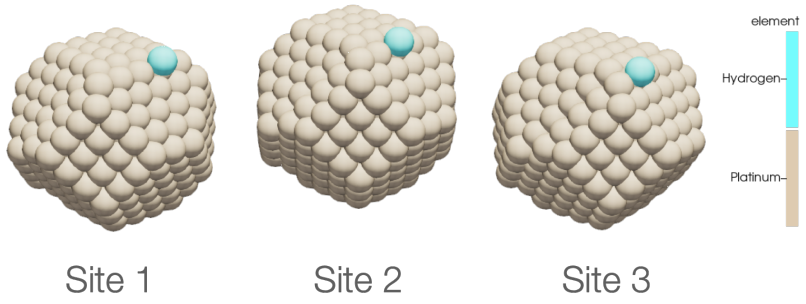

Figure 6.14: Three different final configuration for absorption , where hydrogen bonds with the plastified nanoparticle.

	μ_2	$E_{abs,relax}$	$E_{abs,static}$
Site 1	1.92	-0.512	-0.514
Site 2	1.93	-0.528	-0.527
Site 3	1.93	-0.519	-0.514

Table 6.3: DFT absorption energy calculation, with and without atomic relaxation, together with the second moment.

6.3 IMPROVING ABSORPTION PROPERTIES

6.3.1 INFLUENCE OF PLASTIC EVENTS

Thanks to the insights of the previous sections, we decided to investigate what happens when a Pt nanoparticle undergoes further plastic deformation, depicted as step 4 in Figure 6.8. During this deformation, a second partial dislocation is nucleated, together with the creation of a second stacking fault. Notably, a new step appears around the nanoparticle. This step affects atom coordination, introducing the possibility of new sites that might be intriguing for absorption. The

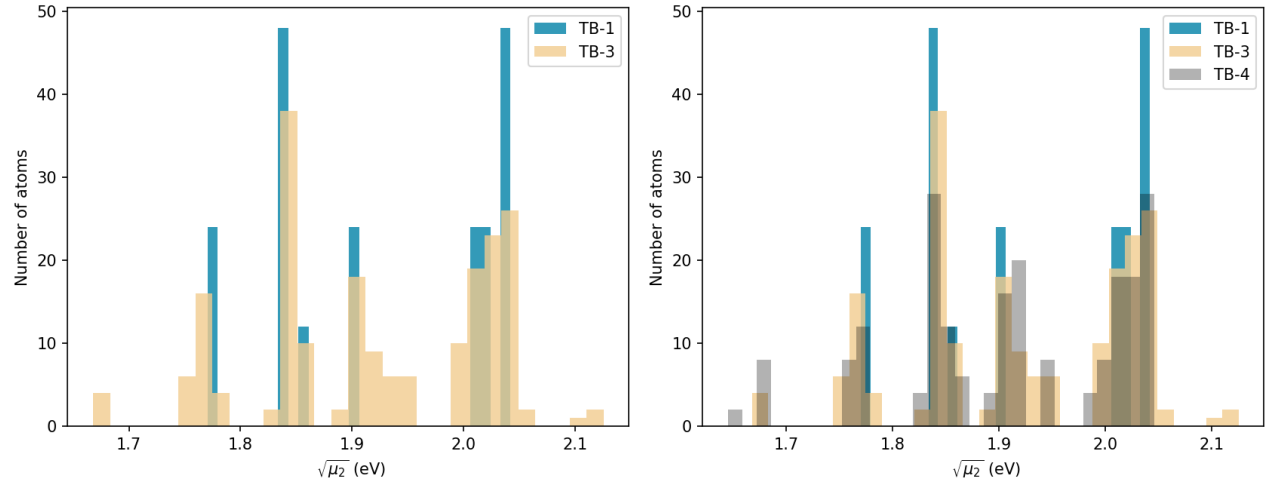

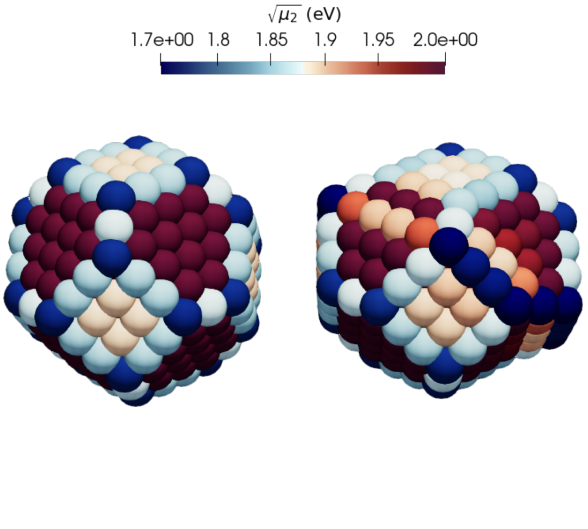

Figure 6.15: Stacking fault's effect on the second moment - results computed with the Tight-Binding method. Figure (a): energy distribution of the initial configuration (labelled 1) and after the first dislocation nucleation (labelled 3). Figure (b): energy distribution of the initial configuration (labelled 1) after the second dislocation nucleation (labelled 4), all energy distribution are focused on surface sites. Figure (c): atomic distribution.

outcomes of this analysis are displayed in Figure 6.15. Panel (a) show the earlier study (step 3), where only the first stacking fault is present.

Moving on to panel (b), we see the nanoparticle after the introduction of the second stacking fault. In this case, there is a rise in the number of new sites with low energy (below 1.8 eV), around the double compared to step 3. Panel (c) specifically illustrates that these low-energy sites are located on the newly formed surface step. In essence, while nanoparticles that have undergone plastic deformation or contain stacking faults may lose some of their inherent energy selectivity, they compensate by offering numerous new low-energy sites. These sites could potentially enhance the absorption properties of the nanoparticle.

6.3.2 Larger nanoparticles

The tight-binding analysis offers advantages over DFT, particularly when examining larger systems. While DFT is typically limited to hundreds of atoms, tight-binding can handle thousands. This capacity allows us to shift from the theoretical model of 405 atoms to more substantial systems that mirror experimental conditions more closely. We expanded our study to include two additional nanoparticles and compared the results at step 3, marking the first plastic event. These new nanoparticles possess truncated octahedral shapes and consist of 1139 and 5341 atoms, corresponding to diameter around 2.5 and 5.6nm, respectively. Figure 6.16 depicts the stress and strain curves for all three particles. Notably, due to their distinct shapes (at this size it is difficult to fix the shape, the shape strongly depends on the number of atoms), the medium-sized nanoparticle exhibits slightly different elastic behavior, but we can still see that bigger is the nanoparticle and lower is the critical stress. A notable change as nanoparticle size

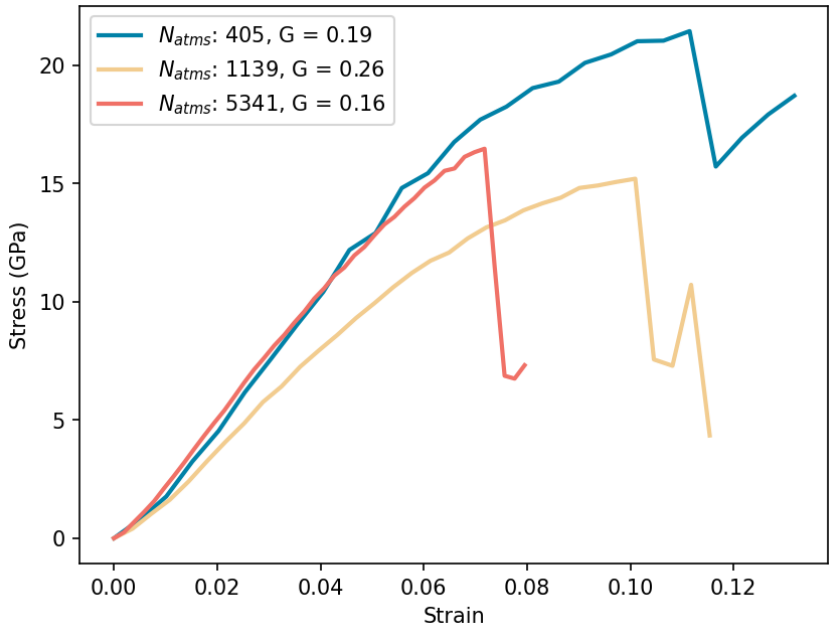

Figure 6.16: True stress and strain curve obtained with MD and with the methodology explained in Chapter 2 for Platinum. Three different sizes and slightly different shapes.

increases is the decrease in the surface-to-volume ratio. Consequently, a larger portion of atoms resides in the core. In terms of percentage, there are fewer atoms at the vertices and edges, with an increase in the (001) and (111) facets. Mechanically speaking, size introduces another variation. With plastic deformation, larger systems exhibit, more almost simultaneous nucleation events. This results in a more significant number of surface steps forming on the nanoparticle's surface, and it can be observed in Figure 6.17, where multiple sites change coordination at step 3. In Figure 6.18, several key aspects are

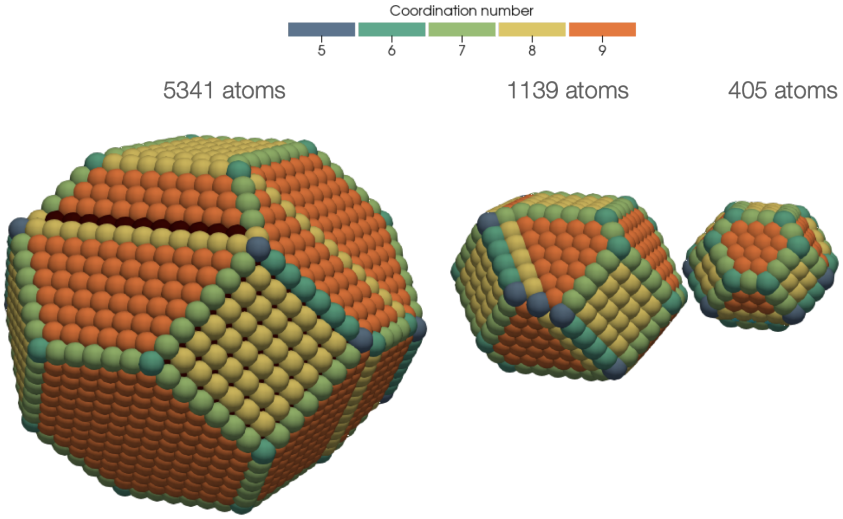

Figure 6.17: Effect of first plastic transition on the coordination number for the three platinum nanoparticles under analysis, with: 5341, 1139, and 405 atoms.

highlighted. Here, we compare the second moment calculated via tight-binding formalism for both step 3 and step 1. Panel (a) features the previous 405-atom study. Panels (b) and (c) present the results for the 1139 and 5341-atom systems, respectively. One immediate observation from the undeformed nanoparticles is the shift in energy distribution. Smaller nanoparticles have a higher percentage of sites on corners and edges. As the system size increases, there is a notable rise in sites at high μ_2, those on the (001) and (111) surfaces.

Looking at the deformed nanoparticle, in big systems, many sites with low $\sqrt{\mu_2}$ values appear during plastic deformation, in number and not in percentage. This is due to the lower surface to volume ratio. As seen in Figure 6.18, zooming in on the histograms show low-energy sites (again below 1.8 eV) whose number increases with particle size. Interestingly, a closer examination of the larger 1139 and 5341 systems, show that these low energy sites appear to emerge from the bulk, contrary to smaller system where they where simply converted from other surface sites. Our study confirms that nanoparticles close in size to those studied experimentally and under plastic deformation are also likely to enhance their surface reactivity. More specifically, we show that nanoparticle size can influence not only the number but also the nature of surface sites reactive to a gaseous environment. In practice, an experimental sample is made up of an assembly of nanoparticles with dispersed diameters. Thus, absorption properties

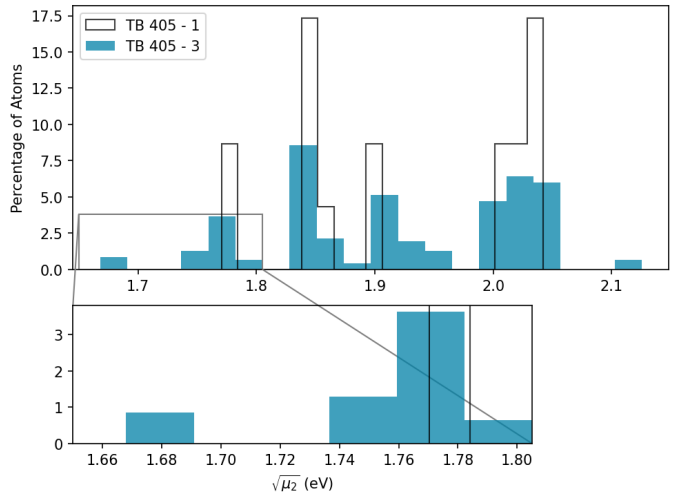

(a)

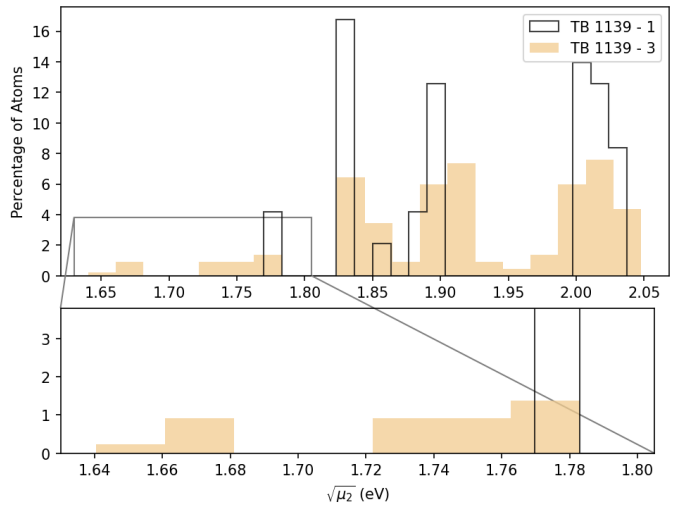

(b)

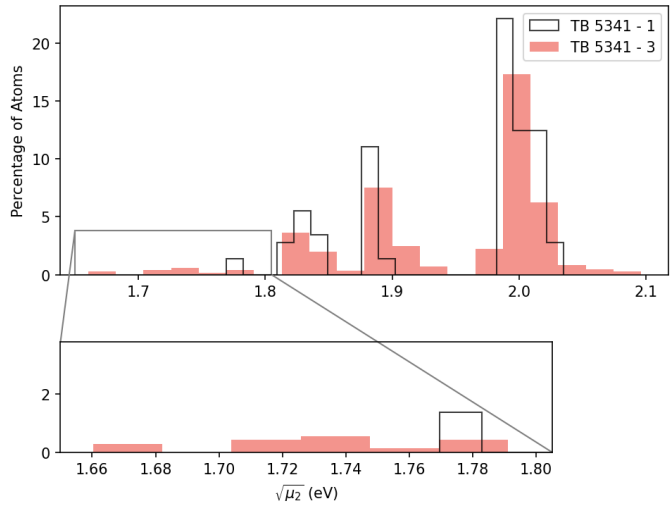

(c)

Figure 6.18: Second moment distribution computed with the tight-binding calculations. Platinum nanoparticles with three different sizes before (labelled 1) and after the first plastic event (labelled 3): 405 (Figure (a)), 1139 (Figure (b)), and 5431 (Figure (c)). A zoom is proposed for the low energy sites.

of the different NPs can be controlled by the charge imposed, since the latter differs according to size, enabling novel engineering of the catalytic properties of NPs.

6.4 Conclusion

In concluding this chapter, it is important to highlight that we develop a tight-binding code (s, p and d orbitals) specifically designed to analyze *ldos* including self-consistent loop to ensure charge neutrality in non-homogeneous systems. This tool has been optimized for parallel computation of large systems (several thousand atoms) such as pristine particles or deformed (elastically and plastically).

After validating the code using DFT calculations, we gained a deeper understanding of how external loads affect the surface reactivity properties of Pt nanoparticle containing 405 atoms. This has been done by performing a fine μ_2 analysis of the *ldos* as the Nørskov model. Our research reveals that applying a uniaxial force (elastic load) to nanoparticles induces no significant changes in their *ldos*, even under significant strains (around 10%). In contrast, when the nanoparticles experience permanent change (plastic deformation), the alterations are far more pronounced. This leads to the emergence of new low-coordinated sites on the surface (i.e., surface steps). While this phenomenon reduces selectivity by creating fewer sites at the same energy, it introduces new energy sites (low μ_2), potentially enhancing the nanoparticle's overall absorption properties. These findings, based on the TB formalism, align with the results from DFT hydrogen absorption calculations on a small platinum system (consisting of 405 atoms).

Thanks to this validation, we extend our tight-binding analysis to a plastically deformed NP. The absorption is intensified as multiple surface steps are created, further amplifying the reactivity process. Lastly, when considering larger systems, that mimic experimental particles, the surface-to-volume ratio decreases, and the percentage of low-coordinated sites (like edges and vertices) drops. However, the total number of available sites increase: for larger NP, in the plastic regime, more dislocation nucleation events occurs at the same time at lower stresses.

Conclusion and perspective 7

7.1 Conclusion

This study revolves around the analysis of how three fundamental factors, namely size, shape and composition, influence mechanical behaviour of nanoparticles, analyzing their elastic and the plastic response, as well as local electronic properties, with a particular focus on absorption reactivity. In the modelling work presented in this manuscript, the subjects are metallic nanoparticles, in the range of about 5-20 nm, of gold, platinum, copper, and the particular case copper-gold alloy. Different modelling techniques have been developed, used or validated to describe multi-scale and multi-physics mechanism, i.e. MD simulations based on SMA-type inter-atomic potentials, finite element calculations, tight-binding Hamiltonian using Green function formalism as well as DFT calculations.

Based on atomistic and continuous calculations, we determined that for transition metal nanoparticles, under external loading, with a diameter larger than 5 nm, there is no size effect on the effective elastic response. Instead, the shape of the particle is fundamental, highly controlling the elastic response. By using a shape descriptor, G, which turns out to evaluate the homogeneity of the stress distribution in nanoparticles, we are now able to predict the effective elastic response of a nanoparticle in a given direction. These results are demonstrated for NPs with FCC structures under an applied load on both surfaces, (001) and (111).

The distribution of the stress field in a NP also dictates the plastic onset, affecting the critical (yield) stress measure. Our findings clearly show that the onset of plasticity depends on NP size and shape. An universal size and shape effect (independent on the material) of the critical stress has been highlighted, expanding results from literature on the Wulff nanoparticles to a broader range of FCC structures, including cubes, truncated-cubes and all truncated octahedrons. A core insight from our research is that the more heterogeneous the elastic field, the stronger the size effect becomes. By examining the von Mises stress and the resolved shear stress, particularly around the corners of compressed nanoparticles where nucleation typically occurs, we noticed that nucleation starts when a local stress condition is reached. Essentially, irrespective of their shapes, these nanoparticles began the nucleation process once a specific internal stress level is achieved within them.

The methodology developed and insights got for pure NPs has been applied to study nano-alloys, focusing on the elastic and plastic responses of ordered and disordered structures in the copper-gold system. In solid solution A_1, our calculations reveals that the elastic response does not depend on local configuration, but an elastic softening is detected with respect to the bulk counterpart. Gold-rich structures are softer than pure gold, while copper-rich are softer compared to pure copper. In the copper-gold system, we also look at segregated nanoparticles. Their reduced residual stress leads to less elastic softening than in the A_1 structure, aligning with bulk elastic response. On the other side, ordered structures, such as $L1_0$ and $L1_2$, are stiffer, consistent with expected bulk properties. In the plastic regime, by comparing A_1 with its segregated version, we deepen our understanding of dislocation nucleation in alloys. In A_1 configurations, plastic softening is observed. This phenomenon is due to two main factors. First, various local arrangements can lead to different stress distributions at the NP corners: nucleation becomes a statistical event influenced by local clustering. Secondly, strength softening is associated with elastic softening, which, implicitly, determines critical stress vaules. Again for the $L1_2$ structure, the well known strengthening effect is recovered, but it is absent in $L1_0$, and the reasons are still under investigation.

Concerning the modelling techniques, thanks to the comparison between FE and atomistic simulations, we can state that FE is effective for nanoscale applications. FE provides accurate results for structures down to 5 nm. However, there can be discrepancies at large strains for metals like platinum, copper, and gold. By extending this analysis to alloys, various mixing patterns were examined using both MD ans FE. Ordered structures, including $L1_0$ and both copper-rich and gold-rich $L1_2$, displayed a close match with FE, having errors less than 5%. Conversely, in the disordered A_1 structure, lattice mismatches introduce internal stresses. This can change the nanoparticle's elastic response, leading to variations between FE and atomistic models. This discrepancy was evident when compared to segregated structures that have minimized internal stress. These structures, indeed, showed a perfect match with FE.

Deformed nanoparticles are exploited to study changes in their electronic properties. For this purpose, a costume tool is developed based on the tight-binding formalism to compute the effects of both elastic and plastic deformation on the electronic properties of indented Pt NPs. Our results emphasize that, unlike elastic deformation, plastic deformation introduces new, low coordinated surface sites that can enhance NP surface reactivity. The enhanced surface reactivity of these new sites is confirmed by DFT calculations examining Hydrogen absorption on plastically deformed Pt NPs.

7.2 Perspective

This study has solved many questions, which were unanswered until now, but from the moment our method of analysis was put in place, many more questions become apparent. Here the main ideas are presented in order of subject.

For the structural modeling method, additional development might account for size effects in the elastic response. This could involve introducing different local elastic constants (for alloy systems) or adding surface strain to address surface contraction. The framework presented in Chapter 3 can be improved by better mimicking real nanoparticles. Edge smoothing and imperfection in the shape, such as roughness, can be introduced. This can induce changes in the shape parameter G, on the stress distribution and consequently on the physics of dislocation nucleation. Concerning the shape and size effect of the critical stress a forthcoming publication will provide further insights, offering detailed explanation of our results, through a simplified 2D study.

In the study of alloys, ordered structures represents another significant research area. The $L1_2$ structure shows strengthening at the plastic onset and a hardening process in the plastic regime, not yet analyzed. This needs to be better understood, backed by a comprehensive study of the stacking fault energy, which is more complex than observed in Appendix 8.6 for solid solutions. The same is true for the $L1_0$ structure and the switching mechanism reported in the final section of Chapter 5. It remains to be seen if the same process can be reproduced with other structures or elements, and check if this mechanism can be captured from an experimental point of view.

In the electronic domain, after an initial refinement of the Nørskov model, the studies might shift to alloy systems under deformation, as for core-shell, janus or ordered and disordered structures.

Finally, from bimetallic systems, the focus may shift to High Entropy Alloys, a growing field of research. The study could initially center on ternary systems, possibly expanding to systems with 4 or 5 elements, such as CoNiPt, CoNiPtCu, CoNiPtAu, and CoNiPtAuCu. An ongoing ANR project targets this area, aiming to enhance both theoretical and experimental understanding of their mechanical properties. Exploring partial segregation and different effects of residual stress could offer more insight into nucleation events and potentially reveal new tunable properties, possibly softer plastic behavior, enhanced ductility, and the prevention of strain burst phenomena. From a modelling point of view, this can be done by developing new potentials in the atomistic domain, or by adapting new strategies in the finite elements framework, such as the definition of local elastic constants or the addition of local strain simulating that induced by lattice mismatch.

Bibliography

[1] McNamara, Karrina and Tofail, Syed AM, 'Nanoparticles in biomedical applications', *Advances in Physics: X* 2.1 (2017), pp. 54–88. cited on pages 1, 12

[2] Ndolomingo, Matumuene Joe, Bingwa, Ndzondelelo, and Meijboom, Reinout, 'Review of supported metal nanoparticles: synthesis methodologies, advantages and application as catalysts', *Journal of Materials Science* 55.15 (2020), pp. 6195–6241. cited on pages 1, 12

[3] Thanh, Nguyen TK and Green, Luke AW, 'Functionalisation of nanoparticles for biomedical applications', *Nano today* 5.3 (2010), pp. 213–230. cited on page 1

[4] Guo, Dan, Xie, Guoxin, and Luo, Jianbin, 'Mechanical properties of nanoparticles: basics and applications', 47.1 (Jan. 8, 2014), p. 013001. cited on pages 1, 12

[5] Phillips, Rob, *Crystals, defects and microstructures: modeling across scales*. Cambridge University Press, 2001. cited on pages 2, 5, 34

[6] Kittel, Charles, 'Introduction to solid state physics Eighth edition' (2021). cited on pages 2, 4, 8, 46, 78, 81

[7] Ashcroft, Neil W and Mermin, N David, *Solid state physics*. Cengage Learning, 2022. cited on pages 2, 5

[8] Boresi, Arthur P and Schmidt, Richard J, *Advanced mechanics of materials*. John Wiley & Sons, 2002. cited on page 5

[9] Hull, Derek and Bacon, David J, *Introduction to dislocations*. Elsevier, 2011, vol. 37. cited on pages 8, 10, 11, 14, 133

[10] Son, Seoung-Bum et al., 'Relationship between microstructure homogeneity and bonding stability of ultrafine gold wire', *Gold Bulletin* 44 (2011), pp. 231–237. cited on page 8

[11] Youssef, Khaled M et al., 'Ultrahigh strength and high ductility of bulk nanocrystalline copper', *Applied Physics Letters* 87.9 (2005). cited on page 8

[12] Zhao, Yonghao et al., 'High tensile ductility and strength in bulk nanostructured nickel', *Advanced Materials* 20.16 (2008), pp. 3028–3033. cited on page 8

[13] Martin Fleck, *Burgers Vector and dislocations (screw and edge type)*, 2020.
URL: https://en.wikipedia.org/wiki/Dislocation cited on page 9

[14] Askeland, Donald R et al., 'The science and engineering of materials' (2003). cited on page 9

cited on page 12 [15] Tang, Youhong et al., 'Interlaminar fracture toughness and CAI strength of fibre-reinforced composites with nanoparticles – A review', *Composites Science and Technology* 86 (Sept. 2013), pp. 26–37.

cited on page 12 [16] Domun, N. et al., 'Improving the fracture toughness and the strength of epoxy using nanomaterials – a review of the current status', *Nanoscale* 7.23 (2015), pp. 10294–10329.

cited on page 12 [17] Loh, Owen Y. and Espinosa, Horacio D., 'Nanoelectromechanical contact switches', *Nature Nanotechnology* 7.5 (May 2012), pp. 283–295.

cited on page 12 [18] Rapoport, L. et al., 'Hollow nanoparticles of WS2 as potential solid-state lubricants', *Nature* 387.6635 (June 1997), pp. 791–793.

cited on pages 12, 13 [19] Uchic, Michael D. et al., 'Sample Dimensions Influence Strength and Crystal Plasticity', *Science* 305.5686 (Aug. 13, 2004), pp. 986–989.

cited on pages 12, 61 [20] Uchic, Michael D, Shade, Paul A, and Dimiduk, Dennis M, 'Plasticity of micrometer-scale single crystals in compression', *Annual Review of Materials Research* 39 (2009), pp. 361–386.

cited on page 13 [21] Greer, Julia R, Oliver, Warren C, and Nix, William D, 'Size dependence of mechanical properties of gold at the micron scale in the absence of strain gradients', *Acta Materialia* 53.6 (2005), pp. 1821–1830.

cited on pages 13, 19, 33, 49 [22] Roy, S. et al., 'A multiscale study of the size-effect in nanoindentation of Au nanoparticles', *Computational Materials Science* 162 (May 2019), pp. 47–59.

cited on pages 13, 32 [23] Amodeo, Jonathan and Pizzagalli, Laurent, 'Modeling the mechanical properties of nanoparticles: a review', *Comptes Rendus. Physique* 22 (S3 May 21, 2021), pp. 1–32.

cited on pages 14, 66 [24] Li, Ju, 'The Mechanics and Physics of Defect Nucleation', *MRS BULLETIN* 32 (2007).

cited on pages 14, 66 [25] Zhu, Ting et al., 'Temperature and Strain-Rate Dependence of Surface Dislocation Nucleation', *Physical Review Letters* 100.2 (Jan. 15, 2008), p. 025502.

cited on page 14 [26] Cottrell, A He, 'Theory of dislocations', *Progress in Metal Physics* 4 (1953), pp. 205–264.

cited on pages 14, 15, 19, 32, 33, 49, 70 [27] Mordehai, Dan et al., 'Size effect in compression of single-crystal gold microparticles', *Acta Materialia* 59.13 (Aug. 2011), pp. 5202–5215.

cited on page 14 [28] Bogy, David B, 'Two edge-bonded elastic wedges of different materials and wedge angles under surface tractions' (1971).

cited on page 15 [29] Zhang, Zhen, Yoon, Juil, and Suo, Zhigang, 'Method to analyze dislocation injection from sharp features in strained silicon structures', *Applied physics letters* 89.26 (2006), p. 261912.

[30] Paggi, Marco and Carpinteri, Alberto, 'On the stress singularities at multimaterial interfaces and related analogies with fluid dynamics and diffusion', *Applied Mechanics Reviews* 61.2 (2008), p. 020801. cited on page 15

[31] Bian, Jian-Jun and Wang, Gang-Feng, 'Atomistic deformation mechanisms in copper nanoparticles', *Journal of Computational and Theoretical Nanoscience* 10.9 (2013), pp. 2299–2303. cited on page 15

[32] Sharma, A et al., 'Nickel nanoparticles set a new record of strength', *Nature communications* 9.1 (2018), p. 4102. cited on pages 15, 32

[33] Zimmerman, J. et al., 'Size and shape effects on the strength of platinum nanoparticles', *Journal of Materials Science* 56.32 (Nov. 2021), pp. 18300–18312. cited on pages 15, 18, 27–29, 59

[34] Feruz, Yosi and Mordehai, Dan, 'Towards a universal size-dependent strength of face-centered cubic nanoparticles', *Acta Materialia* 103 (Jan. 2016), pp. 433–441. cited on pages 15, 17, 50, 59, 63, 69

[35] Kositski, Roman et al., 'Cross-split of dislocations: an athermal and rapid plasticity mechanism', *Scientific Reports* 6.1 (2016), pp. 1–8. cited on page 16

[36] Sharma, A et al., 'Giant shape-and size-dependent compressive strength of molybdenum nano-and microparticles', *Acta Materialia* 198 (2020), pp. 72–84. cited on pages 16, 18, 19

[37] Gerberich, WW et al., 'Superhard silicon nanospheres', *Journal of the Mechanics and Physics of Solids* 51.6 (2003), pp. 979–992. cited on page 16

[38] Wagner, Andrew J. et al., 'Mechanisms of plasticity in near-theoretical strength sub-100 nm Si nanocubes', *Acta Materialia* 100 (Nov. 2015), pp. 256–265. cited on pages 16, 17, 27

[39] Kilymis, D. et al., 'Uniaxial compression of silicon nanoparticles: An atomistic study on the shape and size effects', *Acta Materialia* 158 (Oct. 2018), pp. 155–166. cited on pages 16–18, 33, 46, 50, 59

[40] Issa, I. et al., 'In situ investigation of MgO nanocube deformation at room temperature', *Acta Materialia* 86 (Mar. 2015), pp. 295–304. cited on page 16

[41] Sarobol, Pylin et al., 'Room temperature deformation mechanisms of alumina particles observed from in situ micro-compression and atomistic simulations', *Journal of Thermal Spray Technology* 25 (2016), pp. 82–93. cited on page 16

[42] Ferrando, Riccardo, Jellinek, Julius, and Johnston, Roy L., 'Nanoalloys: From Theory to Applications of Alloy Clusters and Nanoparticles', *Chemical Reviews* 108.3 (Mar. 1, 2008), pp. 845–910. cited on pages 16, 17, 80

[43] Bisht, Anuj et al., 'The impact of alloying on defect-free nanoparticles exhibiting softer but tougher behavior', *Nature Communications* 12.1 (Dec. 2021), p. 2515. cited on pages 16, 17, 75, 79, 87, 88

cited on page 16 [44] Chen, Jianxin, Li, Pengtao, and Lin, E Emily, 'A molecular dynamics study on the mechanical properties of Fe–Ni alloy nanowires and their temperature dependence', *RSC Advances* 10.66 (2020), pp. 40084–40091.

cited on pages 16, 75 [45] Rosa Abad, Juan A. de la et al., 'On the mechanical response in nanoalloys: the case of NiCo', *Faraday Discussions* (2022), 10.1039.D2FD00111J.

cited on pages 16, 75, 88, 89 [46] Sharma, Amit et al., 'Solid-solution and precipitation softening effects in defect-free faceted Nickel-Iron nanoparticles', *Acta Materialia* (Nov. 2022), p. 118527.

cited on page 17 [47] Kilymis, D., Gérard, C., and Pizzagalli, L., 'Ductile deformation of core-shell Si-SiC nanoparticles controlled by shell thickness', *Acta Materialia* 164 (Feb. 2019), pp. 560–567.

cited on page 17 [48] Yeh, J-W et al., 'Nanostructured high-entropy alloys with multiple principal elements: novel alloy design concepts and outcomes', *Advanced engineering materials* 6.5 (2004), pp. 299–303.

cited on page 17 [49] Cantor, Brain et al., 'Microstructural development in equiatomic multicomponent alloys', *Materials Science and Engineering: A* 375 (2004), pp. 213–218.

cited on page 17 [50] George, Easo P., Raabe, Dierk, and Ritchie, Robert O., 'High-entropy alloys', 4.8 (June 18, 2019), pp. 515–534.

cited on page 17 [51] Yan, Jingyuan et al., 'Anomalous size effect on yield strength enabled by compositional heterogeneity in high-entropy alloy nanoparticles', *Nature Communications* 13.1 (Dec. 2022), p. 2789.

cited on page 18 [52] Cao, Ajing and Ma, E., 'Sample shape and temperature strongly influence the yield strength of metallic nanopillars', *Acta Materialia* 56.17 (Oct. 2008), pp. 4816–4828.

cited on pages 18, 32, 50 [53] Amodeo, Jonathan and Lizoul, Khalid, 'Mechanical properties and dislocation nucleation in nanocrystals with blunt edges', *Materials & Design* 135 (Dec. 2017), pp. 223–231.

cited on pages 19, 52 [54] Armstrong, Patrick and Peukert, Wolfgang, 'Size effects in the elastic deformation behavior of metallic nanoparticles', *Journal of Nanoparticle Research* 14.12 (Dec. 2012), p. 1288.

cited on page 19 [55] Ramos, Manuel et al., 'Hardness and Elastic Modulus on Six-Fold Symmetry Gold Nanoparticles', *Materials* 6.1 (Jan. 14, 2013), pp. 198–205.

cited on page 19 [56] Hazarika, A. et al., 'STM verification of the reduction of the Young's modulus of CdS nanoparticles at smaller sizes', *Surface Science* 630 (Dec. 2014), pp. 89–95.

cited on pages 19, 45 [57] Yang, L et al., 'An analytical description for the elastic compression of metallic polyhedral nanoparticles', *AIP Advances* 6.8 (2016), p. 085113.

[58] Gatti, R et al., 'Modeling the plastic relaxation onset in realistic SiGe islands on Si (001)', *Physical Review B* 78.18 (2008), p. 184104. cited on page 19

[59] Skibitzki, Oliver et al., 'Reduction of threading dislocation density beyond the saturation limit by optimized reverse grading', *Physical Review Materials* 4.10 (2020), p. 103403. cited on page 19

[60] Persichetti, L et al., 'Formation of extended thermal etch pits on annealed Ge wafers', *Applied Surface Science* 462 (2018), pp. 86–94. cited on page 19

[61] Moseley, Philip and Curtin, WA, 'Computational design of strain in core–shell nanoparticles for optimizing catalytic activity', *Nano letters* 15.6 (2015), pp. 4089–4095. cited on pages 19, 20, 23, 24, 45, 84, 93

[62] Vogelsang, Thi and Hofmann, KR, 'Electron mobilities and high-field drift velocities in strained silicon on silicon-germanium substrates', *IEEE Transactions on Electron Devices* 39.11 (1992), pp. 2641–2642. cited on page 20

[63] Bedell, SW, Khakifirooz, A, and Sadana, DK, 'Strain scaling for CMOS', *Mrs Bulletin* 39.2 (2014), pp. 131–137. cited on page 20

[64] Stephens, Ifan Erfyl Lester, Rossmeisl, Jan, and Chorkendorff, Ib, 'Toward sustainable fuel cells', *Science* 354.6318 (2016), pp. 1378–1379. cited on page 20

[65] Luo, Mingchuan and Guo, Shaojun, 'Strain-controlled electrocatalysis on multimetallic nanomaterials', *Nature Reviews Materials* 2.11 (2017), pp. 1–13. cited on pages 20, 23, 93

[66] Sneed, Brian T, Young, Allison P, and Tsung, Chia-Kuang, 'Building up strain in colloidal metal nanoparticle catalysts', *Nanoscale* 7.29 (2015), pp. 12248–12265. cited on page 20

[67] Zhang, Zhicheng et al., 'One-pot synthesis of highly anisotropic five-fold-twinned PtCu nanoframes used as a bifunctional electrocatalyst for oxygen reduction and methanol oxidation', *Advanced Materials* 28.39 (2016), pp. 8712–8717. cited on page 20

[68] Wu, Jianbo et al., 'Icosahedral platinum alloy nanocrystals with enhanced electrocatalytic activities', *Journal of the American Chemical Society* 134.29 (2012), pp. 11880–11883. cited on page 20

[69] Chattot, Raphaël et al., 'Beyond strain and ligand effects: microstrain-induced enhancement of the oxygen reduction reaction kinetics on various PtNi/C nanostructures', *Acs Catalysis* 7.1 (2017), pp. 398–408. cited on page 20

[70] Slater, John C and Koster, George F, 'Simplified LCAO method for the periodic potential problem', *Physical review* 94.6 (1954), p. 1498. cited on pages 21, 94

[71] Sutton, Adrian P, *Electronic structure of materials*. Clarendon Press, 1993. cited on pages 21, 22, 35, 94

cited on pages 21, 94, 95 [72] Papaconstantopoulos, Dimitris A et al., *Handbook of the band structure of elemental solids*. Springer, 1986.

cited on pages 22, 23, 96 [73] Hammer, Bjørk and Nørskov, Jens Kehlet, 'Advances in catalysis', vol. 45, Elsevier, 2000, pp. 71–129.

cited on page 22 [74] Mavrikakis, Manos, Hammer, Bjørk, and Nørskov, Jens Kehlet, 'Effect of strain on the reactivity of metal surfaces', *Physical Review Letters* 81.13 (1998), p. 2819.

cited on page 24 [75] Nørskov, Jens Kehlet et al., 'Towards the computational design of solid catalysts', *Nature chemistry* 1.1 (2009), pp. 37–46.

cited on page 24 [76] Jia, Qingying et al., 'Activity descriptor identification for oxygen reduction on platinum-based bimetallic nanoparticles: in situ observation of the linear composition–strain–activity relationship', *ACS nano* 9.1 (2015), pp. 387–400.

cited on page 27 [77] Yu, Q, Legros, Marc, and Minor, AM, 'In situ TEM nanomechanics', *Mrs Bulletin* 40.1 (2015), pp. 62–70.

cited on page 27 [78] Carlton, CE and Ferreira, PJ, 'In situ TEM nanoindentation of nanoparticles', *Micron* 43.11 (2012), pp. 1134–1139.

cited on page 28 [79] Henry, Claude R., 'Morphology of supported nanoparticles', *Progress in Surface Science* 80.3-4 (2005), pp. 92–116.

cited on page 28 [80] Wulff, G., 'Zur Frage der Geschwindigkeit des Wachsthums und der Auflösung der Krystallflächen', *Z. Kristallogr.* 34 (1901), p. 449.

cited on pages 28, 29 [81] Tao, Andrea R, Habas, Susan, and Yang, Peidong, 'Shape control of colloidal metal nanocrystals', *small* 4.3 (2008), pp. 310–325.

cited on page 28 [82] Habibullah, Giyaullah, Viktorova, Jitka, and Ruml, Tomas, 'Current strategies for noble metal nanoparticle synthesis', *Nanoscale Research Letters* 16.1 (2021), pp. 1–12.

cited on page 28 [83] Baletto, F et al., 'Crossover among structural motifs in transition and noble-metal clusters', *The Journal of chemical physics* 116.9 (2002), pp. 3856–3863.

cited on page 29 [84] Larsen, Ask Hjorth et al., 'The atomic simulation environment—a Python library for working with atoms', *Journal of Physics: Condensed Matter* 29.27 (2017), p. 273002.

cited on page 31 [85] Frenkel, Daan and Smit, Berend, *Understanding molecular simulation: from algorithms to applications*. Elsevier, 2001, vol. 1.

cited on page 32 [86] Thompson, A. P. et al., 'LAMMPS - a flexible simulation tool for particle-based materials modeling at the atomic, meso, and continuum scales', *Comp. Phys. Comm.* 271 (2022), p. 108171.

cited on page 33 [87] Zhu, Ting et al., 'Temperature and strain-rate dependence of surface dislocation nucleation', *Physical Review Letters* 100.2 (2008), p. 025502.

[88] Carlsson, A.E., 'Beyond Pair Potentials in Elemental Transition Metals and Semiconductors', *Solid State Physics*, vol. 43, Elsevier, 1990, pp. 1–91. cited on page 34

[89] Ducastelle, F., 'Modules élastiques des métaux de transition', 31.11 (1970), pp. 1055–1062. cited on pages 34, 35

[90] Cyrot-Lackmann, F., 'On the calculation of surface tension in transition metals', 15.3 (July 1969), pp. 535–548. cited on page 34

[91] Stillinger, Frank H. and Weber, Thomas A., 'Computer simulation of local order in condensed phases of silicon', 31.8 (Apr. 15, 1985), pp. 5262–5271. cited on page 34

[92] Rosato, Vittorio, Guillope, M, and Legrand, B, 'Thermodynamical and structural properties of fcc transition metals using a simple tight-binding model', *Philosophical Magazine A* 59.2 (1989), pp. 321–336. cited on page 35

[93] Daw, Murray S. and Baskes, M. I., 'Embedded-atom method: Derivation and application to impurities, surfaces, and other defects in metals', *Physical Review B* 29.12 (June 15, 1984), pp. 6443–6453. cited on page 35

[94] Zienkiewicz, Olek C, Taylor, Robert Leroy, and Zhu, Jian Z, *The finite element method: its basis and fundamentals*. Elsevier, 2005. cited on page 39

[95] Alnaes, M. S. et al., 'The FEniCS Project Version 1.5', *Archive of Numerical Software* 3 (2015). cited on page 39

[96] Geuzaine, Christophe and Remacle, Jean-François, 'Gmsh: A 3-D finite element mesh generator with built-in pre-and post-processing facilities', *International journal for numerical methods in engineering* 79.11 (2009), pp. 1309–1331. cited on page 40

[97] Grosso, Giuseppe and Parravicini, Giuseppe Pastori, *Solid state physics*. Academic press, 2013. cited on pages 42, 43

[98] Chmielewski, Adrian et al., 'Direct measurement of the surface energy of bimetallic nanoparticles: evidence of vegard's rule-like dependence', *Physical Review Letters* 120.2 (2018), p. 025901. cited on pages 46, 77

[99] Mottet, Christine et al., 'Stress effect on segregation and ordering in Pt–Ag nanoalloys', *Journal of Physics: Condensed Matter* 33.15 (2021), p. 154006. cited on page 46

[100] Delfour, L, Creuze, J, and Legrand, B, 'Exotic behavior of the outer shell of bimetallic nanoalloys', *Physical review letters* 103.20 (2009), p. 205701. cited on page 46

[101] Vitos, Levente et al., 'The surface energy of metals', *Surface science* 411.1-2 (1998), pp. 186–202. cited on pages 46, 81

[102] Darling, AS, 'The elastic and plastic properties of the platinum metals', *Platinum Metals Review* 10.1 (1966), pp. 14–19. cited on page 46

cited on page 47 [103] Stukowski, Alexander, 'Visualization and analysis of atomistic simulation data with OVITO–the Open Visualization Tool', *Modelling and simulation in materials science and engineering* 18.1 (2009), p. 015012.

cited on pages 47, 51 [104] Gupta, Raju P, 'Lattice relaxation at a metal surface', *Physical Review B* 23.12 (1981), p. 6265.

cited on page 47 [105] Ahrens, James, Geveci, Berk, and Law, Charles, *Visualization Handbook*, ed. by Hansen, Charles D. and Johnson, Christopher R. Burlington, MA, USA: Elsevier Inc., 2005, chap. ParaView: An End-User Tool for Large Data Visualization, pp. 717–731.

cited on page 51 [106] McDowell, Matthew T, Leach, Austin M, and Gall, Ken, 'On the elastic modulus of metallic nanowires', *Nano letters* 8.11 (2008), pp. 3613–3618.

cited on page 51 [107] Hemmerle, Arnaud, Schröter, M, and Goehring, Lucas, 'A tunable cohesive granular material', *Sci. Rep* 24 (2016), p. 35650.

cited on page 51 [108] Goyal, Monika and Gupta, BRK, 'Study of shape, size and temperature-dependent elastic properties of nanomaterials', *Modern Physics Letters B* 33.26 (2019), p. 1950310.

cited on page 51 [109] Dhulipala, Somayajulu et al., 'Tunable Mechanical Response of Self-Assembled Nanoparticle Superlattices', *Nano Letters* (2023).

cited on page 60 [110] Gerberich, William W et al., 'Reverse plasticity in single crystal silicon nanospheres', *International Journal of Plasticity* 21.12 (2005), pp. 2391–2405.

cited on page 66 [111] Miller, Ronald E and Acharya, Amit, 'A stress-gradient based criterion for dislocation nucleation in crystals', *Journal of the Mechanics and Physics of Solids* 52.7 (2004), pp. 1507–1525.

cited on page 66 [112] Zhu, Ting et al., 'Predictive modeling of nanoindentation-induced homogeneous dislocation nucleation in copper', *Journal of the Mechanics and Physics of Solids* 52.3 (2004), pp. 691–724.

cited on page 66 [113] Liu, Yufu, Van der Giessen, Erik, and Needleman, Alan, 'An analysis of dislocation nucleation near a free surface', *International Journal of Solids and Structures* 44.6 (2007), pp. 1719–1732.

cited on page 66 [114] Miller, Ronald E and Rodney, David, 'On the nonlocal nature of dislocation nucleation during nanoindentation', *Journal of the Mechanics and Physics of Solids* 56.4 (2008), pp. 1203–1223.

cited on page 75 [115] Irani, R.S and Cahn, R.W, 'Order-hardening of CuPt', *Acta Metallurgica* 21.5 (May 1973), pp. 575–584.

cited on page 75 [116] Delannoy, Laurent et al., 'Selective hydrogenation of butadiene over TiO 2 supported copper, gold and gold–copper catalysts prepared by deposition–precipitation', *Physical Chemistry Chemical Physics* 16.48 (2014), pp. 26514–26527.

[117] Liu, Xiaoyan et al., 'Au–Cu alloy nanoparticles supported on silica gel as catalyst for CO oxidation: Effects of Au/Cu ratios', *Catalysis today* 160.1 (2011), pp. 103–108. cited on page 75

[118] Okamoto, H et al., 'The Au- Cu (gold-copper) system', *Journal of Phase Equilibria* 8 (1987), pp. 454–474. cited on page 76

[119] Barrera, GD, De Tendler, RH, and Isoardi, EP, 'Structure and energetics of Cu-Au alloys', *Modelling and Simulation in Materials Science and Engineering* 8.3 (2000), p. 389. cited on page 78

[120] Gola, Adrien and Pastewka, Lars, 'Embedded atom method potential for studying mechanical properties of binary Cu–Au alloys', *Modelling and Simulation in Materials Science and Engineering* 26.5 (2018), p. 055006. cited on pages 78, 132, 133

[121] Simmons, Gene and Wang, Herbert, 'Single crystal elastic constants and calculated aggregate properties: a handbook', *(No Title)* (1971). cited on page 78

[122] Sparnaay, MJ and Thomas, GE, 'Surface segregation in Au0. 1Cu0. 9 crystals', *Surface Science* 135.1-3 (1983), pp. 184–198. cited on page 81

[123] Guisbiers, Grégory et al., 'Gold–copper nano-alloy,"tumbaga", in the era of nano: phase diagram and segregation', *Nano letters* 14.11 (2014), pp. 6718–6726. cited on page 81

[124] Breyton, Grégoire et al., 'Atomic-Scale Surface Segregation in Copper-Gold Nanoparticles', *Physical Review Letters* 130.23 (2023), p. 236201. cited on pages 81, 82

[125] Amodeo, Jonathan, Begau, C, and Bitzek, E, 'Atomistic simulations of compression tests on Ni3Al nanocubes', *Materials Research Letters* 2.3 (2014), pp. 140–145. cited on page 89

[126] Atlan, Clément et al., 'Imaging the strain evolution of a platinum nanoparticle under electrochemical control', *Nature Materials* (2023), pp. 1–8. cited on page 93

[127] Gröger, Oliver, Gasteiger, Hubert A, and Suchsland, Jens-Peter, 'Electromobility: Batteries or fuel cells?', *Journal of The Electrochemical Society* 162.14 (2015), A2605. cited on page 93

[128] Desjonqueres, M-C and Spanjaard, Daniel, *Concepts in Surface Physics: 2eme édition*. Springer Science & Business Media, 1996, vol. 30. cited on page 94

[129] Kitchin, JR et al., 'Modification of the surface electronic and chemical properties of Pt (111) by subsurface 3d transition metals', *The Journal of chemical physics* 120.21 (2004), pp. 10240–10246. cited on page 99

[130] Giannozzi, Paolo et al., 'QUANTUM ESPRESSO: a modular and open-source software project for quantum simulations of materials', *Journal of physics: Condensed matter* 21.39 (2009), p. 395502. cited on page 104

cited on page 104 [131] Giannozzi, Paolo et al., 'Advanced capabilities for materials modelling with Quantum ESPRESSO', *Journal of physics: Condensed matter* 29.46 (2017), p. 465901.

cited on page 129 [132] Zhang, Lin et al., 'Anisotropic elasticity of silicon and its application to the modelling of X-ray optics', *Journal of synchrotron radiation* 21.3 (2014), pp. 507–517.

cited on page 129 [133] Front, Alexis and Mottet, Christine, 'Ordering Frustration in Large-Scale Co–Pt Nanoalloys', *The Journal of Physical Chemistry C* 125.29 (2021), pp. 16358–16365.

Appendix

8 Supplementary material

8.1 Convention

8.1.1 crystallographic convention

In crystallography, specific notations distinguish between vectors, planes, and their families. Here's a brief outline of the convention used in this work.

- $[ijk]$ Represents a direction vector along the lattice parameters i, j and k.
- (ijk) Denotes a plane that is normal (perpendicular) to the vector $[ijk]$.
- $\{ijk\}$ Refers to the set or family of equivalent planes that have the same crystallographic properties as the (ijk) plane.
- $\langle ijk \rangle$ Indicates the set or family of direction vectors equivalent to $[ijk]$ in terms of their crystallographic significance.

8.1.2 Einstein Notation

The Einstein summation notation, is a concise way to represent sums over repeated indices, typically used in tensor operations. This notation is especially valuable when working with multi-dimensional arrays (like tensors) in the context of continuum mechanics and physics.

In Einstein notation, whenever an index is repeated in a term, it implies a summation over that index. For example, considering vectors a_i and b_i, the dot product can be written as:

$$a_i b_i$$

This implicitly means:

$$\sum_{i=1}^{n} a_i b_i$$

where n is the dimension of the vectors.

When working with second order tensors, like the stress σ_{ij} and strain ϵ_{ij} tensors, and a fourth order elastic tensor C_{ijkl}, relationships can be concisely written using Einstein notation.

For instance, the linear relationship between stress and strain can be written in tensor form as:

$$\sigma_{ij} = C_{ijkl}\epsilon_{kl}$$

In the above expression, both k and l are repeated indices, indicating a summation over them. This means that for each pair of i, j, we sum over all combinations of k, l. In a 3D space, this would mean that i, j, k, l each take on values 1, 2, or 3 corresponding to the x, y, and z directions, respectively.

8.2 Elastic properties - Copper and platinum

More results concerning the elastic properties of Copper and Platinum nanoparticles for nano-indentation on (001) facets are presented in the Figure 8.1 and 8.2.

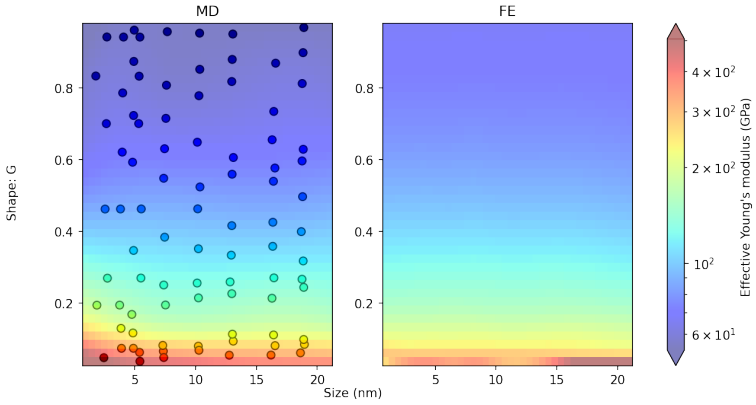

Figure 8.1: Copper, comparison between FE and MD. (001) facet

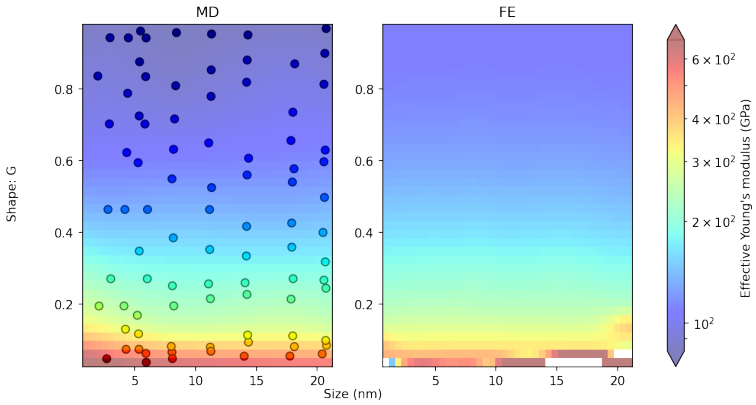

Figure 8.2: Platinum, comparison between FE and MD. (001) facet

8.3 Directional Young's modulus

These equations describe the methodology for computing the compliance matrix (the inverse of the stiffness matrix or the elastic constants) and the direction-dependent Young's modulus in a face-centered cubic (FCC) structure.

The compliance matrix, denoted as S_{hkl}, which is derived from the elastic constant tensor C_{hkl}, provides a measure of how the material

strain responds to stress. In an FCC structure, the elements of the compliance matrix are given by:

$$
\begin{aligned}
s_{11} &= \frac{c_{11} + c_{12}}{(c_{11} - c_{12})(c_{11} + 2c_{12})} \\
s_{12} &= \frac{-c_{12}}{(c_{11} - c_{12})(c_{11} + 2c_{12})} \\
s_{44} &= \frac{1}{c_{44}}
\end{aligned}
$$

The Young's modulus, E, is a measure of the material's stiffness. In an FCC structure, E is direction-dependent (represented by the Miller indices hkl). The inverse of the Young's modulus is given by:

$$
\frac{1}{E_{hkl}} = s_{11} - 2(s_{11} - s_{12} - \frac{1}{2}s_{44})(m^2n^2 + n^2p^2 + p^2m^2) \tag{8.1}
$$

The coefficients m, n, and p represent the direction cosines that define the hkl direction in respect to the Cartesian axes:

$$
\begin{aligned}
m &= \frac{h}{\sqrt{h^2 + k^2 + l^2}} \\
n &= \frac{k}{\sqrt{h^2 + k^2 + l^2}} \\
p &= \frac{l}{\sqrt{h^2 + k^2 + l^2}}
\end{aligned}
$$

These direction cosines normalize the hkl indices, enabling us to examine the material behavior along different crystallographic directions. This framework allows us to compute the direction-dependent Young's modulus, a crucial element for understanding and predicting the mechanical behavior of anisotropic materials like crystalline alloys[132].

8.4 Alloy - CoPt

We make use of the SMA potential developed by *Front et al.*, primarily for structural analysis of the cobalt platinum alloy[133]. We test this potential from a more mechanical point of view, although our analysis is confined to the A_1 structure, which represents a solid solution. Notably, we observe a significant deviation from Vegard's Law in the case of the lattice parameter. In addition, the elastic constant shows an unusual behavior at around an 80% concentration of cobalt. This peculiar behaviour also mirrors in the calculations of Young's

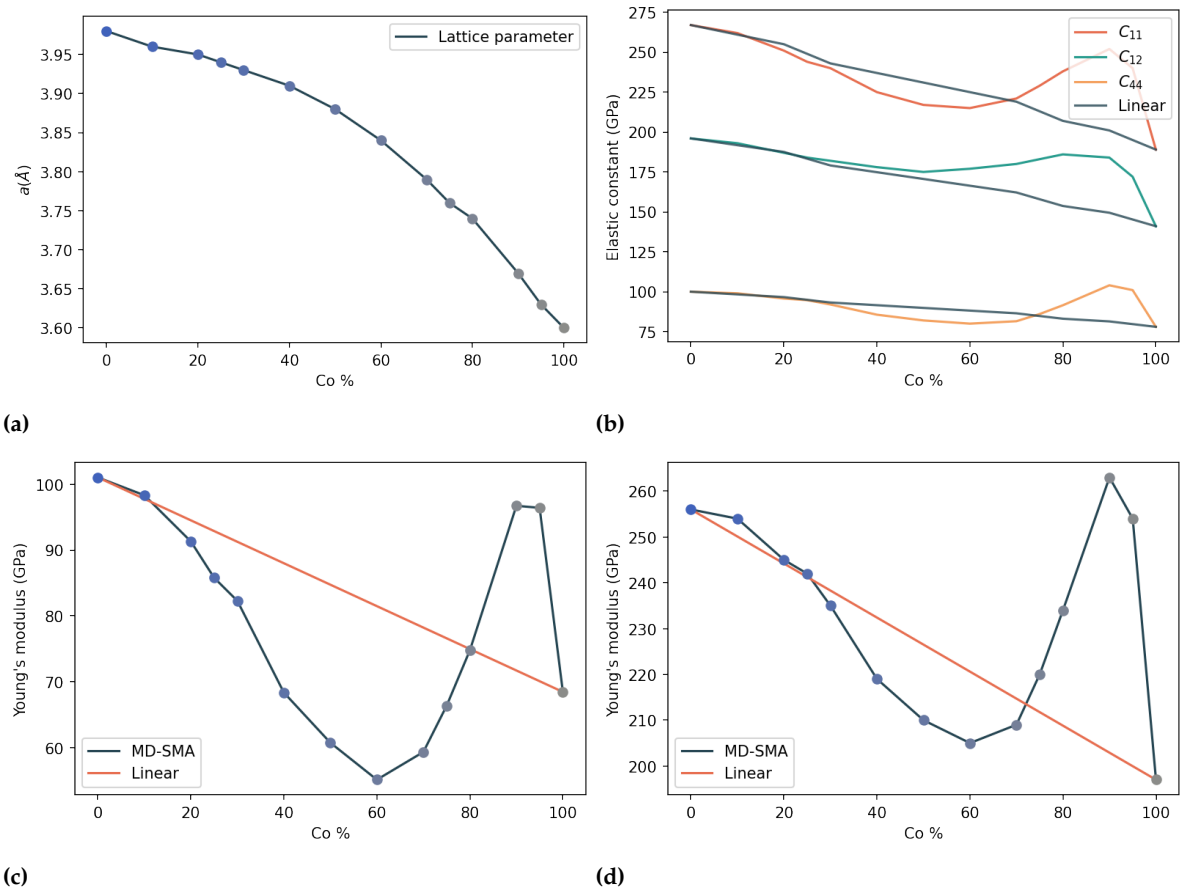

Figure 8.3: Figure (a). Lattice parameter as function of copper density. Figure (b). Elastic constant as function of the cobalt density. Figure (c): Young's modulus as a function of the cobalt density, (001) direction. Figure (d): (111) direction.

modulus, implying an unanticipated change in the material's stiffness at this particular concentration. However, because of these anomalous results, we put the use of this potential on hold for further study and refinement.

8.5 (111) Cu_xAu_{1-x} Elastic and Plastic behaviour

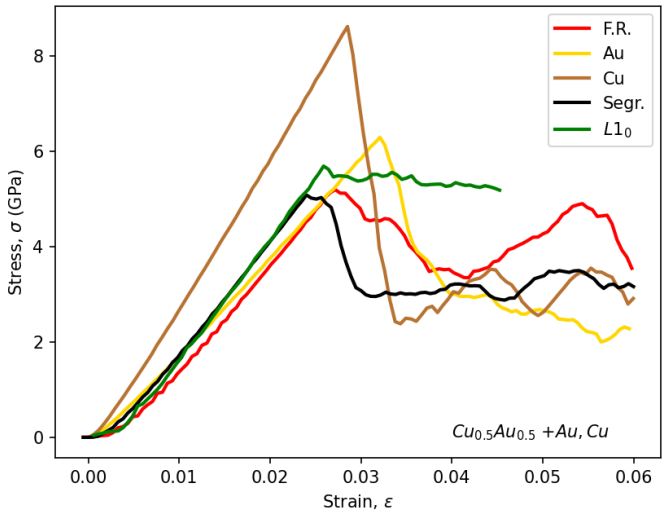

Figure 8.4: Stress and strain curve. CuAu system (111) facet, A_1, segr., $L1_0$ and pure copper and gold.

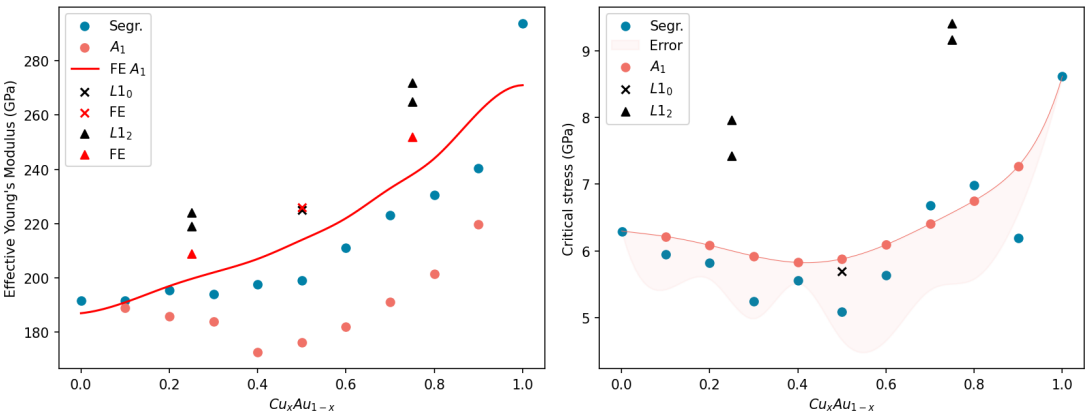

(a) **(b)**

Figure 8.5: Figure (a):(111) Effective Young's modulus at different Cu concentration, with ordered structure: $L1_0$ and $L1_2$, disordered structure: A_1 and the segregated counterpart. A comparison is proposed with two different methods, Finite Element and Molecular Dynamics. Figure (b): Critical stress at different copper concentrations. A_1 and segregated structure for the disordered systems. $L1_2$ and $L1_0$ for the ordered nanoparticles.

Similar observations to Chapter 5 are replicated for the (111) facet. In Figure 8.5, we present the stress-strain curve for the CuAu system, and the extracted elastic properties. The disparity between the two disordered systems is less significant in gold-rich nanoparticles and more pronounced in copper-rich ones. The Finite Element curve accurately aligns with the bulk trend depicted in Figure 5.3b. However, it markedly deviates from the A_1 systems, with discrepancies of the order of 20% and less than 10% in the segregated structure. It is probable that the residual σ_{zz} in the (111) direction system deviates on average more than that in the (001) system.

8.6 STACKING-FAULT ENERGY

For an accurate study of the plastic regime, a detailed examination of the selected inter-atomic potentials is essential. This goes beyond the simple extraction of elastic constants as detailed in Chapter 3, and the size effect analysis of σ_c outlined in Chapter 4. Typically, this includes analysis of both the SFE and the USFE. The SFE indicates a material's tendency to deform through planar slip, in presence of partial dislocations, or deformation twinning. The higher the SFE, the less likely the material is to form stacking faults or twins during deformation. The USFE is the energy barrier to create a stacking fault: if the energy barrier to is low, then the material might deform, creating or extendig a stacking fault, more easily. To compute both quantities MD simulation were performed. We employ the NPT ensemble (to allow relaxation of the simulation box) for a $30 \times 30 \times 30$ atomic layers with periodic boundary conditions in x an y directions, setting the [111] direction parallel to z. After an intial energy minimisation the crystal is then split into two parts (upper and lower with respect z direction) and the top section is shifted in the plane (a typical example is shown in Figure 8.6). This procedure emulates that presented by *Gola et al.*[120].

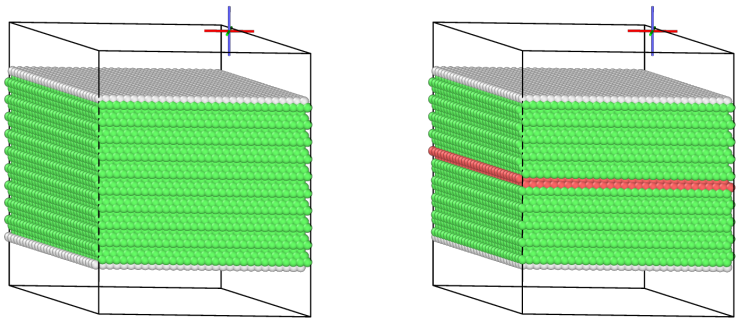

(a) **(b)**

Figure 8.6: Sample created for the SFE calculation. 27000 atoms with boundary conditions in all direction but void is added along z. The [111] is aligned with z to allows the fault to be in the plane $x - y$. Figure (a) pristine sample. Figure (b) sample with stacking fault.

By shifting in the x and y directions, we can determine the stacking fault energy γ_{sh} as:

$$\gamma_{sh} = \frac{E_{sh} - E_p}{A}$$

Here, E_{sh} is the shifted system energy, E_p is the perfect system's energy, and A is the stacking fault area.

Figure 8.7 displays the result for pure gold. The red regions mark high-energy areas where atomic gliding is less probable, while the blue regions denote potential valleys where gliding is more likely, as given by Equation 1.12. This behavior corresponds with movement along the B-C direction as depicted in figure 8.8, where introducing the initial partial dislocation locally turns the crystal to an HCP structure.

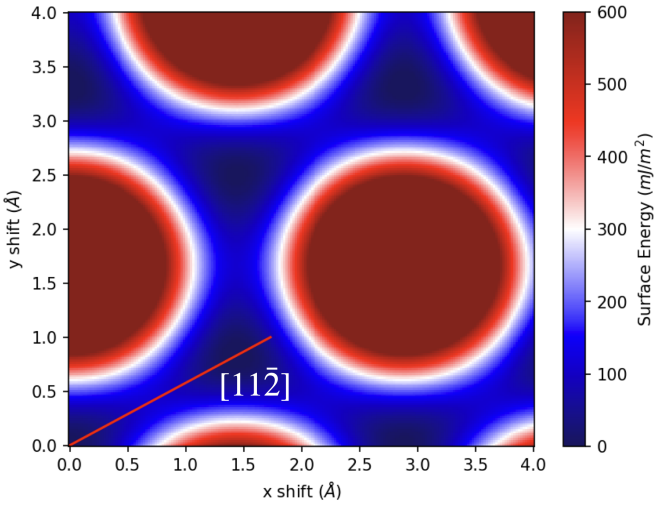

Figure 8.7: The surface energy γ_{sh} computed for at different x and y shifts. In red is unlighted the direction where the second minimum can be found.

In Figure 8.9, the map shown in Figure 8.7 is cut along the indicated direction and the results is shown for three different material: gold, copper and platinum (corresponding to the potential already used in the previous chapters). in this Figure the maximum value represents USFE, i.e. the energy barrier to overcome to create a stacking fault, while the energy value of the three minimum is SFE the energy associated to the creation of the stacking fault itself.

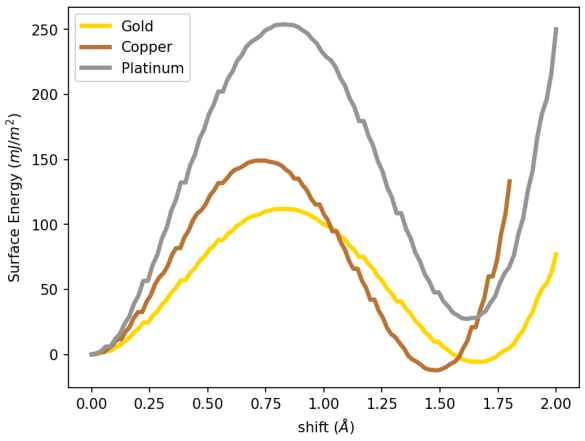

Figure 8.9: Surface energy γ_{sh} along the $[11\bar{2}]$ for three different material, Gold, Copper, and Platinum

Table 8.1 shows that the USFE values are consistent with findings in Chapter 4, displaying a higher value for Pt compared to copper and gold. This pattern mirrors the rigid shift seen in size effects. However, regarding SFE, we observed a discrepancy, for copper and gold, where the faulted structure, an HCP structure, appears more stable contrary to experimental data and other research [120]. Contrary, for platinum, the initial FCC structure is the more stable configuration, aligning well with experimental findings.

We continued to analyze the SFE of the copper-gold alloy, focusing first on the A_1 configuration. The previous procedure is followed, in the NPT minimisation atoms are allowed to relax before the rigid shift, to create the expected residual strain due to lattice mismatch. In this

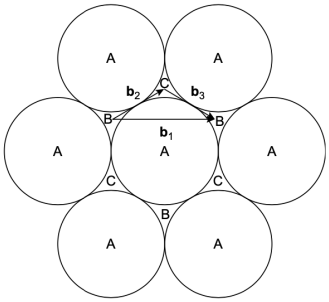

Figure 8.8: Partial dislocation moving atom B in C position, creating a stacking fault. The effect of the second partial dislocation bringing back atom B in a B position. Figures extracted from [9].

-	STE	USTE
Au	-5.61	112
lit.	39	103
Cu	-12.1	149
lit.	51	179
Pt	27.4	254
lit.	-	-

Table 8.1: Computed values of SFE and USFE, units are in mJ/m^2. Literature *lit.* values extracted from [120]

preliminary findings no statistic is made, with one sample for the one concentration. In Figure 8.11a, the extracted slice in the [11$\bar{2}$] direction

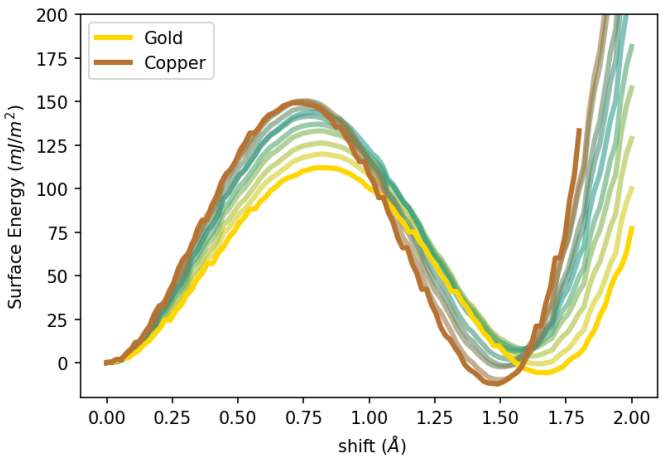

Figure 8.10: A_1 surface energy γ_{sh} along the [11$\bar{2}$] for three different material, Gold, Copper, and the various concentration between them. Figure (b) Extracted SFE. Figure (c) Extracted USFE

is depicted, and Figure 8.11b presents the derived SFE and Figure 8.11c the USFE values. Regarding the USFE, despite some fluctuations due to lack of statistic, a potential barrier transitioning from that of gold to that of copper can be observed. This transition contradicts the previous assumption that USFE is associated with nucleation stress, instead appearing to follow the elastic constant C_{44} more closely. Turning to the SFE, we found it to be consistent with earlier data for pure materials, showing negative values. Notably, at intermediate concentrations, the SFE turns positive, indicating a greater stability in the FCC structure, a positive outcome. An analysis of the stress and strain curves in Figure 5.6 shows no notable tougher behaviour in the A_1 configuration, suggesting that strain bursts are still possible (After the first maximum σ_c, there is no hardening). Impurities only trigger earlier nucleation without much effect on slowing its progression.

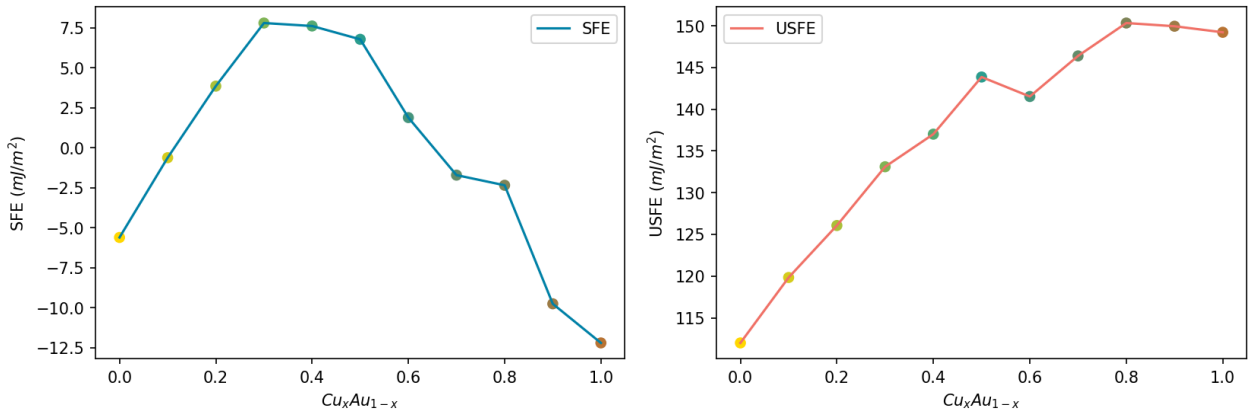

(a) **(b)**

Figure 8.11: Figure (a): A_1 surface energy γ_{sh} along the [11$\bar{2}$] for three different material, Gold, Copper, and the various concentration between them. Figure (b) Extracted SFE. Figure (c) Extracted USFE